LOW-INDEX SURFACES RECONSTRUCTION AND ITS INFLUENCE ON VICINAL SURFACES: THE CASE OF AU(100) AND AU(111).

Thesis submitted for the degree of
"Doctor Philosophiae"

CANDIDATE
Anna Bartolini

SUPERVISORS
Prof. Erio Tosatti
Dr. Furio Ercolessi

November 1988

Contents

Introduction 1

1 A review of the "glue" model **5**
- 1.1 The failure of pair potential 5
- 1.2 The glue Hamiltonian for gold 7
  - 1.2.1 The glue concept 7
  - 1.2.2 Construction of the glue Hamiltonian for gold 9
- 1.3 Other many-body force models 13
- 1.4 Molecular dynamics for the glue model 16

2 Previous applications of the glue model **20**
- 2.1 Bulk and surface properties of gold 20
- 2.2 Au(100) surface reconstruction 22
  - 2.2.1 Experimental studies 22
  - 2.2.2 Au(100) surface reconstruction at T=0 in the glue model 23
- 2.3 Au(110) surface reconstruction at T=0 in the glue model . 30

3 Au(111) surface reconstruction **35**
- 3.1 Review of the experimental facts and the proposed models . 35
  - 3.1.1 Experimental results 35
  - 3.1.2 Models for Au(111) surface reconstruction 38
  - 3.1.3 Models for Au(111) surface reconstruction with solitons 39
- 3.2 Simulation studies of Au(111) surface reconstruction in the glue model 47
  - 3.2.1 Au(111) surface reconstruction at T=0 47

3.2.2 Au(111) surface reconstruction with increasing temperature 53

4 Review of physical properties of vicinal surfaces 62
4.1 Surface crystallography 62
4.2 Experimental observations 63
4.3 Theoretical considerations: the Wulff plot and the faceting of a vicinal surface 66
4.4 The interaction among steps on a stepped surface 74
4.5 Experimental observation on interplay between steps and reconstruction 75
4.5.1 Experimental studies of (K,1,1) Au(100)-vicinals . . 76
4.5.2 Experimental studies of (M+1,M−1,M) Au(111)-vicinals 78

5 Simulation of Au(100)-vicinals 81
5.1 General description of (K,1,1) Au(100)-vicinals 81
5.2 Structure and energetics of quenched and annealed samples 86
5.2.1 The (3,1,1), (5,1,1) and (7,1,1) vicinals 87
5.2.2 Sharp and smooth steps 94
5.2.3 A model for surface energies of quenched samples . . 100
5.3 "Stabilized" (K,1,1) Au(100)-vicinals 108
5.3.1 The "tilting" pressure. 108
5.3.2 The Wulff plot 109
5.3.3 The faceting of (K,1,1) Au(100)-vicinals 109

6 Simulation of Au(111)-vicinals 120
6.1 General description of (M+1, M−1, M) Au(111)-vicinals . . 120
6.2 Structure and energetics of (M+1,M−1,M) Au(111)-vicinals 123
6.3 A model for the surface energies of quenched samples 128
6.4 "Stabilized" (M+1, M−1, M) Au(111)-vicinals 131
6.4.1 The "tilting pressure" 131
6.4.2 The faceting of (M+1,M−1,M) Au(111) vicinals . . 134

7 Conclusions and possible outlooks 138

Bibliography 142

Acknowledgements 150

Introduction

Any fundamental understanding of the microscopic properties of a solid surface requires a reasonably detailed model of the atomic geometry. It is well known that for many metals and semiconductor surfaces the two dimensional periodicity of the outermost layer is not identical to that of an equivalent parallel layer in the bulk (*"reconstruction"*) and that the spacing between adjacent layers in the surface zone is not the same as in the interior of the crystal (*"relaxation"*).

Surface reconstruction was first observed about 30 years ago by LEED (Low-Energy-Electron-Diffraction) on studies of clean Si and Ge crystals, and it is now recognized as a common phenomenon on semiconductors. By contrast, for clean metal surfaces, it was thought that reconstruction was not important since until fairly recently the only known examples were the low index faces (100) and (110) of Ir, Pt and Au. But more recently, surfaces of a number of other metals, including the (100) surface of Mo, W, V, Cr and Al and the (110) one of Al, have been reported to reconstruct spontaneously [1], even if for some of them the reconstruction phenomenon seems to be attributable to the non perfect cleanness of the surface. Also the close-packed Au(111) has been seen to reconstruct. Furthermore it has become evident that in many systems the presence of chemisorbed species can induce a rearrangement of the outermost metal atoms.

Thus the reconstruction phenomenon, is not only of fundamental interest in studying atomic geometry, electronic structure, electronic density of states, electronic work function, surface phonons, surface phase transitions, some phenomena of crystal growth and epitaxy, but may be essential also for the understanding of the nature of the adatom-substrate and adatom-adatom interactions in metals.

The experimental evidence for surface reconstruction has come primarily from investigations by LEED and, more recently, by HEIS or RBS (High Ion Scattering or Rutherford Backscattering), RHEED (Reflection High Energy Electron Diffraction), FIM (Field Ion Microscopy), TEM (Transmission Electron Microscopy), TED (Transmission Electron Diffraction), STM (Scanning Tunneling Microscopy) and by HAD (He-Atom Diffraction). Additional, but less direct information has been obtained by correlation of structural data with measurements concerning the surface electronic structure, that is, photoemission and work function, and with chemisorption studies involving the kinetics of adsorption, diffusion and desorption, and surface phase diagrams.

It seems clear that surface reconstruction is driven by the tendency towards minimum surface free energy. However, an accurate calculation of the free energy from first principles is very difficult and theoretical predictions of the equilibrium geometry of metal surfaces are almost completely lacking. Only some phenomenological approaches have had success, as it will be clear further.

The experimental evidence suggests that reconstructive rearrangements are favoured on fcc metals, whereas displacive rearrangements (i. e. rearrangements in which no interatomic bonds are broken and no new ones are formed) are favoured on bcc metals.

The preferred models for the (fcc) noble metals Ir, Au and Pt surface reconstructions are based on the assumption that the surface atoms tend to form a close-packed [111]-like configuration. The reconstructed surface then has fewer "dangling bonds" per surface atom. Obviously, this cannot be true in general, since no reconstruction is seen on clean Ag and Pd surfaces, for example. The explanation of the displacive rearrangement on clean W(100) and Mo(100) also depends on a detailed understanding of the surface electronic structure.

This thesis focuses on gold, which stands out for its remarkable reconstruction properties. In fact, it is the only metal which exhibits reconstruction on *all* its low-index surfaces, including (111).

Reconstruction, just like many other bulk and surface properties of metals, cannot be described by simple models based on pairwise interactions. On the other hand, first principle methods, fully taking into account the

presence of conduction electrons, require a considerable computational effort to study systems with $N \simeq 100$ atoms, and cannot be used for much larger systems, such as those required to study reconstructions with large unit cells. To fill this gap, several phenomenological many-body scheme, able to mimic the effects of electrons in metals, have appeared in the last few years. One of these schemes, reviewed in detail in Chapter 1, is the so called "glue-model" introduced by Ercolessi, Parrinello and Tosatti. The main idea behind this model consists of introducing an energy dependence of each atom upon its coordination, which in turn is assumed to be a quantity characterizing well the electronic environment around the atom. This mechanism seems to be particularly well suited to model noble metals.

Chapter 2 contains a review of previous applications of the glue model, by Ercolessi et al., to bulk and surface properties of gold. In particular, the behaviour of Au(100) surface reconstruction is characterized by the superstructure (1×5), which takes into account the reconstruction in the fivefold direction and by the (34×5) one, that considers also the possibility of reconstruction in the multifold direction. Also the Au(110) missing-row (1×2) reconstruction is reproduced in the glue scheme.

In Chapter 3 we focus our attention on Au(111) surface not previously studied. First of all the complex experimental and theoretical situation will be reviewed. There have been various attempts to explain its superstructure $(p \times \sqrt{3})$ with $p \simeq 23$. In some of these the epitaxy between the first and the second layer is characterized by an alternance of fcc and hcp domains separated by "soliton" walls. In the second part of this Chapter the glue model, coupled with a standard molecular-dynamics strategy, is used to search the optimal structure of Au(111) surface at $T = 0$. It is found to be reconstructed, in qualitative agreement with known facts. With this simulation, we also investigate the low temperature properties, while high-T phase transitions [2] cannot be pursued due to our small size box and short simulation times.

In view of the satisfactory description which the glue model yields for all low-index surfaces of gold, one is encouraged to try to use the same model to study higher index surfaces. Au(100)- and Au(111)-vicinals appear particularly interesting, due to the possible interplay effects between steps and reconstruction. We have chosen to investigate the $(K, 1, 1)$ family of Au(100)-vicinals (Chapter 5), and the family of Au(111)-vicinals (Chapter 6).

Before treating gold vicinals, we review (Chapter 4) some general physical properties of vicinal surfaces. In particular, we describe the Wulff polar plot of the surface free energy as a function of the orientation of the vicinal and the associated construction of the equilibrium crystal shape. The Herring criterion, for which a vicinal chooses to form a "hill and valley" structure or regular array of steps is also reviewed, together with the behaviour of vicinal surfaces at finite temperature (roughening transition). At the end of the Chapter, what is known experimentally about the two classes examined of gold vicinals is reviewed.

Our main observation, which is further pursued quantitatively in Chapters 5 and 6, is that the presence of reconstruction on the low-index faces must induce an effective locking force between the steps. In particular, steps may rearrange themselves so as to form terraces, whose length is such to accommodate an integer number of reconstruction unit cells. Therefore, certain "magic" vicinal surfaces must be preferred to others, and should ubiquitously appear in the faceting habit of the crystal.

Chapter 5 contains our results for the vicinals of Au(100). The main result is that two magic vicinals are expected, namely (5,1,1) and (11,1,1), in perfect agreement with experiments.

Chapter 6 describes our studies of the Au(111) vicinals, where we do not find similarly sharp magic vicinals, but rather a slight preference for vicinals, where terrace lengths are multiple of the basic (111) reconstruction cell length. This finding may, in fact, explain Kaiser and Jaklevic' s STM data [3], where steps have been observed in perfect registry with the basic reconstruction period.

At the end of the thesis (Chapter 7) further comments on our results are reported, along with some possible outlooks.

Chapter 1

A review of the "glue" model

1.1 The failure of pair potential

It has been known for a long time the theoretical inadequacy of the model, used to describe the cohesion of solids, according to which the metal is composed by single entities (undeformed atoms or molecules) with a pairwise interaction. The main physical feature of a metal is the multitude of conduction electrons that constitutes a sort of quantum mechanical "glue", which in no way can be taken in consideration by a pairwise model.

In spite of the absence of any theoretical foundation, the pairwise model, which arranges a center of force in every lattice position, has been for long time the only way to do many predictions, at least for bulk properties. However it has many shortcomings:

(a) it cannot account simultaneously for the cohesion and the melting behaviour of a metal. In fact with this model the ratio $C = E_c/k_B T_M$, (where E_c is the cohesive energy per atom and T_M is the melting temperature), which is around 30 in metals (and 10 in rare gas solids), turns out to be always nearly 10. This means that a system with the correct cohesion is stiff compared to the real material and melts at a much higher temperature, while a system with a nearly correct T_M has a cohesion too low [4].

(b) By the pairwise model, it results that the vacancy formation energy E_v is nearly equal to the cohesive energy E_c, while in metals E_v/E_c results about 1/3 [5].

(c) It fails in reproducing the behaviour of the elastic constants of metals. In fact it predicts the "Cauchy relation" [6] between two of the three

independent elastic constants in a cubic crystal

$$C_{12} = C_{44} \tag{1.1}$$

while the real C_{44} (one of the shear moduli) is much lower in metals,as also suggested by the high ductility and malleability of these materials.

(d) It fails completely in explaining surface properties, especially surface reconstructions; besides, it leads to an outwards relaxation of the first surface layer, while metals usually show the opposite behaviour.

(e) It predicts an extremely high evaporation rate near the melting temperature, as seen from molecular dynamics simulations [7,8]. This results in a high value for the vapour tension.

Some of these difficulties can be solved by adding a volume dependent term to the total potential energy [9,10]; this correction contains a linear term in the volume

$$V = \frac{1}{2} \sum_{ij,j \neq i} \phi(r_{ij}) + p_o \, \Omega. \tag{1.2}$$

If $p_o = \frac{1}{2}(C_{12} - C_{44})$, ("Cauchy pressure") the correct behaviour of elastic constants can be predicted.

We conclude therefore that, in order to give a realistic description of the strong cohesive character of the metallic bond and of the defects formation, in particular of the observed structure of real metal surfaces, we cannot disregard the presence of the conduction electrons, whose "gluing" role can in no way be simulated by a pairwise interaction.

So, in order to consider the electronic effects, a many-body term must be added to the interatomic two-body potential and this must be density dependent. This fact can be explained intuitively, considering that the common feature of every defect formation process, including surfaces, is a local change of the atomic arrangement in the zone where the defect has been created.

For this reason, when we attempt to model such a situation in noble metals, the key variable to consider is the local atomic coordination, that is the number of neighbours of a given ion. Assuming that the coordination around an ion represents in some way the amount of local electronic density, we can take this coordination as the variable characterizing the environment in which the ion is situated. So we can think that when its coordination

is nearly equal to the bulk coordination, the ion moves in a normal way, interacting with the other ions through an effective two body-potential. However, motions which tend to change the coordination in an appreciable way are greatly discouraged by their high energetic cost. Such a mechanism cannot be modeled by two-body forces because a two-body scheme implies a linear dependence of the energy of an atom upon its coordination. An essential feature of an alternative scheme must be the non-linearity of this dependence.

1.2 The glue Hamiltonian for gold

1.2.1 The glue concept

Many attempts have been done to construct Hamiltonians which include a many-body term. One of such schemes is that developed by Ercolessi, Parrinello and Tosatti (EPT) [11,12,13], where the total potential energy of the system is written as:

$$V = \frac{1}{2} \sum_{ij,j \neq i} \phi(r_{ij}) + \sum_{i} U(n_i). \tag{1.3}$$

A standard two-body part $\phi(r_{ij})$ is still present together with the new many-body term $U(n_i)$, which replaces the volume dependent term in Eq.(1.2); it is a function of the coordination of each atom i and associates an energy value to this coordination, including the previously discussed "gluing effects" of the conduction electrons; for this reason it has been named "the glue".

It is natural to impose $U(0) = 0$. In this way the total energy is referred to that of a system of N atoms at rest, infinitely far each from the other.

The coordination n_i, for each atom i in the system, is constructed as a superposition of contributions coming from the neighbours of atom i

$$n_i = \sum_{j,j \neq i} \rho(r_{ij}), \tag{1.4}$$

where $\rho(r)$ is a short-ranged, monotonically decreasing function of the distance. This equation essentially counts the number of neighbours of atom i. This is done in a continuous way, so that nearby atoms give a contribution

to n_i larger than far atoms. The final result for n_i is a real number that generalizes the usual idea of coordination.

Some points to be underlined are [11,14]:

(a) the units for ρ (and n) are arbitrary; in particular, given $\rho(r)$ and $U(n)$, $\hat{\rho}(r)$=c$\rho(r)$ and $\hat{U}(n) = U(n/c)$ describe the same physics, giving rise to the same forces for an arbitrary value of c. As a consequence, we have the freedom to define a scale for n. We can take, conveniently for a bulk fcc or hcp atom in an undistorted lattice $n_o = 12$. If we think to apply the equation for n_i to such an atom, we can have a normalization condition for $\rho(r)$. In fact, if $\rho(r)$ has a range limited to the first neighbours, we have: $n_o = 12 = 12\rho(d)$ (from (1.4)), where d is the first neighbours distance, from which it derives the normalization condition $\rho(d) = 1$.

(b) There is an important invariance property of the glue Hamiltonian: it gives rise to forces, which remain unchanged when the functions $\phi(r)$, $U(n)$, $\rho(r)$ are replaced by $\hat{\phi}(r)$, $\hat{U}(n)$, $\rho(r)$

$$\hat{\phi}(r) = \phi(r) + 2\lambda\rho(r) \tag{1.5}$$

$$\hat{U}(n) = U(n) - \lambda n \tag{1.6}$$

and λ is an arbitrary real number.

This fact can be seen immediately by substituting such functions in the glue Hamiltonian (1.3). From this invariance, many examples take to the conclusion that it is not possible to attribute a physical meaning to either $U(n)$ or $\phi(r)$, when considered separately, in spite of the apparent well-defined distinction between the two and many-body term. Only invariant quantities can be related to physical properties. Examples of such quantities are $U''(n)$, which is directly connected to many-body effects as shown below, and the "effective potential"

$$\psi(r,n) = \phi(r) + 2U'(n)\rho(r) \tag{1.7}$$

which defines, roughly, an effective pairwise interaction in an environment characterized by an average coordination n. A particularly convenient condition that can be imposed, removing the ambiguity, is

$$U'(n_o) = 0. \tag{1.8}$$

With this condition $U(n)$ has a minimum in correspondence with the bulk coordination n_o.

Very briefly, it can be seen that the glue Hamiltonian removes the Cauchy discrepancy in the elastic constants. In fact the Cauchy pressure results [14]

$$\frac{1}{2}(C_{12} - C_{44}) = \frac{8\sqrt{2}}{d}\rho'(d)^2 U''(12). \tag{1.9}$$

Among the others, the glue Hamiltonian solves also the problem of the low vacancy formation energy compared to the cohesive energy; in fact the former, neglecting relaxations, is the energy associated with the breaking of 12 bonds, and the change of the coordination of the 12 neighbour atoms from 12 to 11, and it can be expressed as

$$E_v = -6\phi(d) + 12(U(11) - U(12)) \tag{1.10}$$

while the latter is

$$E_c = -[6\phi(d) + U(12)] \tag{1.11}$$

giving rise to $(E_v/E_c) < 1$, as a consequence of the non-linearity of $U(n)$.

As it will be shown, the glue Hamiltonian also explains the presence of surface reconstruction on noble metal surfaces.

On the other hand, as seen by calculating the dynamical matrix for the glue Hamiltonian, the glue term does not have any effect on the transverse phonon frequencies, which are completely determined by the two-body potential [15]. This can be understood intuitively by noting that the coordination remains roughly constant in a transverse mode, while it changes in a longitudinal mode.

From this fact it derives that the elastic constants associated to the transverse modes (i. e. the shear moduli) are also determined only by the two-body part.

1.2.2 Construction of the glue Hamiltonian for gold

The three functions $\phi(r)$, $\rho(r)$, $U(n)$, appearing in the "glue" Hamiltonian, have been constructed by fitting a certain number of physical quantities (expressed by the three functions now nominated of the glue Hamiltonian) to the experimental values for a given material (in our case gold).

For the gold fit, a fcc crystal structure, a first neighbours range for $\phi(r)$ and $\rho(r)$, the normalizations for n and ρ ($n_o = 12$, $\rho(d) = 1$) and the condition $U'(n_o) = 0$ have been assumed.

The two most important expressions, that can be found from the glue Hamiltonian and can be used in the fit, are those for the cohesive energy (1.11) and for the bulk modulus of the system

$$B = \left(\frac{2\sqrt{2}}{3d}\right)\phi''(d) + \left(\frac{16\sqrt{2}}{d}\right)\rho'(d)^2 U''(12). \qquad (1.12)$$

In the fitting procedure, the following experimental data have been fitted exactly [11,14]:

(1) $T = 0$ lattice parameter $a_o = 4.0704$ Å.

(2) Cohesive energy $E_c = 3.78$ eV/atom.

(3) Surface energy $\sigma = 96.8$ meV/Å^2. This value has been fitted on a not reconstructed, but relaxed (111) face.

(4) Bulk modulus B = $1.803\ 10^{12}$ dyne/cm^2.

(5) Frequency of the transverse phonons at point X of the Brillouin zone, $\nu_T(X) = 2.75$ THz.

Moreover the following quantities have been reasonably reproduced:

(6) Vacancy formation energy $E_v = 0.95$ eV.

(7) Thermal expansion coefficient $\alpha = 15.8\ 10^{-6}$ K^{-1}.

(8) Melting temperature, $T_M = 1336$ K.

(9) Instability of the ideal surface structures.

(10) Phonon dispersion relations, even if they can be fitted only in an approximate way, as it is well explained in [14].

The analytic forms used for the three functions of the glue Hamiltonians and the details of the fit are discussed elsewhere [14]. What we want to remark is that these details are generally dependent on the material which is to be reproduced, so that different materials may require different procedures and different analytic forms.

Most of the quantities listed above allow a determination of the functions or of their derivatives only at some particular values of the arguments. For instance, Eq. (1.11) connects the cohesive energy with $\phi(r)$ at $r = d$ and $U(n)$ at $n = 12$.

In constructing the three functions $\phi(r)$, $\rho(r)$, $U(n)$ there remains a large freedom in the shape of these functions far from these fitting points. Therefore it is possible to construct many different triplets of functions, all

of which fit the same quantities listed above, but describe different physical systems. Anyhow one can confidently hope to find (by some powerful selective tests) in the large space of all the possible choices, a realization with overall properties similar to those of the real material.

Thermal properties constitute the most useful test. In fact, when the atoms vibrate, they sample wide regions of the three functions, so that the behaviour of the system depends on their whole shape, ever relatively far from the fit points. The thermal test is particularly severe at high temperatures, where anharmonic effects play an important role. In fact properties like the thermal expansion coefficient or the melting temperature are very sensitive to tiny details in the shape of ϕ, ρ, U. For instance, the slope of the core-core region in the 2-body potential turns out to be crucial in determining the melting temperature.

Besides the thermal properties, other stringent tests for the glue Hamiltonian are linked to the description of defects and in particular of surface properties.

To resume, thermal and surface properties depend on the detail of the glue Hamiltonian in a complex way, so that they are not easy to fit. However, by using molecular-dynamics and a trial and error approach, it is possible to reproduce them rather accurately. This work requires a suitable parametrization of ϕ, ρ, U flexible enough to allow shape variations of the functions within the constraints given by the fit points.

From what it has been said before, it is clear that it is not possible to find an "optimal" realization of the glue Hamiltonian. The search for such an Hamiltonian terminates when a satisfactory realization is found.

The shapes of $\phi(r)$, $\rho(r)$, $U(n)$, obtained by this procedure are shown in Fig. 1.1.

Some remarks are to be done:

– $\phi(r)$ is an usual two-body potential with a cutoff $r_c = 3.50$ Å.

$\phi_o = \phi(d)$ is the depth of the potential, which, using (1.8), determines the partition of the cohesion between the two-body part and the glue part. It also determines the anharmonicity of the potential: a deep potential is more harmonic than a shallow one. This has visible effects, for instance, in the thermal expansion coefficient.

– $\rho(r)$ itself cannot fit any physical property. Only some combinations of $\rho(r)$ and $U(n)$ are related to quantities of the physical system (like, for instance, the equation of the bulk modulus (1.12), which has been used in

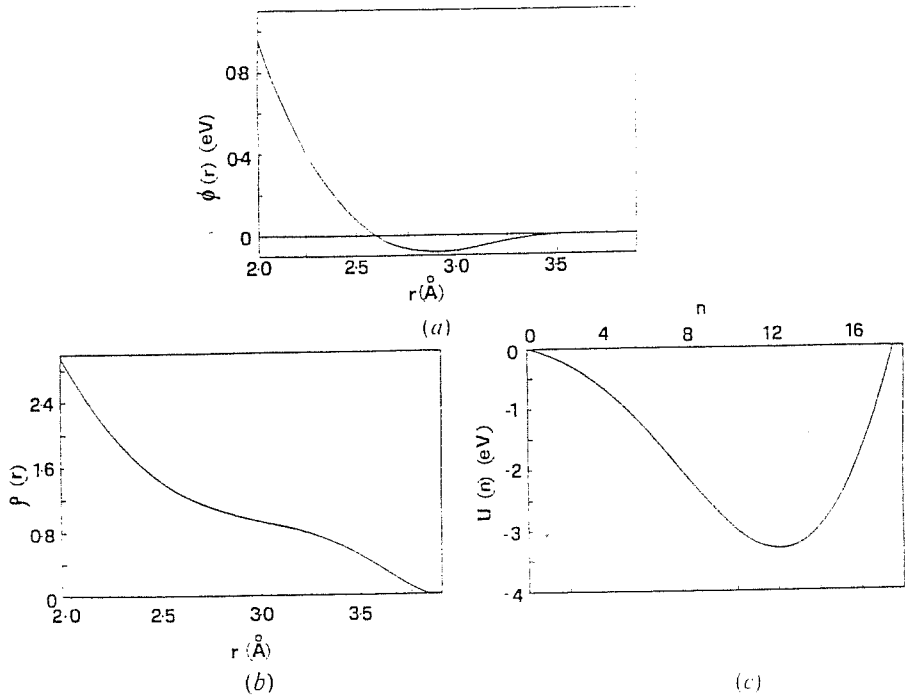

Figure 1.1:
The three functions (a)$\phi(r)$, (b) $\rho(r)$, (c) $U(n)$ optimized for gold.

the fit).

The cutoff region between 3.5 Å and 3.9 Å has been located in correspondence with the minimum between the first and second neighbours shell in the pair correlation function (as determined by high T simulations).

The shape of $\rho(r)$ in region around $r = d$ is very important because it determines how the atoms gain and loose coordination when their mutual distances are varied. Since the changes in the energy associated with coordination changes are large, slight modifications on $\rho(r)$ for r around the first neighbours distance can have dramatic effects on the thermal behaviour and in surface properties. For example the presence of surface reconstructions can be switched on or off by acting on $\rho(r)$ for $r \leq d$.

– $U(n)$, the glue function, is characterized by a strong rising above $n = 12$. This rise corresponds to a sort of core-core repulsion, but obtained through the glue term instead of the two body term. This peculiar behaviour permits to have a system with the right melting temperature and

enough anharmonic to yield a realistic thermal expansion. In particular, the core-core region is soft enough to allow large vibrational amplitudes of the atoms (thus obtaining a realistic melting temperature); the anharmonicity (which gives rise to a correct thermal expansion behaviour) is, instead, supplied by the glue: at high temperatures, in fact, the shape of the glue around $n = 12$ favours fluctuations which tend to decrease, rather than increase, the local coordination. The system reacts by increasing slightly the lattice parameter.

The realization of a Hamiltonian with a "hard" glue, which permits to maintain a soft two body potential, favours also surface reconstructions, involving large atom rearrangements and shrinkage of the bond lengths.

A final important remark to do is that the glue is central (or not directional), that is the glue energy depends only on the number of neighbours around an atom, while how these neighbours are disposed is not relevant.

As a consequence, when the interaction is limited to the first and second neighbours, the fact that the energies of fcc and hcp crystal structures are degenerate, can be attributed to this shortcoming. In fact, the first- and second-neighbour shells contain the same number of atoms at the same distances in the two structures, and the only difference is in the angular distribution of the second neighbours.

However, this lack of angular forces, even if absent in other alternative approaches, is very convenient from a computational point of view.

1.3 Other many-body force models

It should be pointed out that some alternative approaches lead to the same scheme as the glue Hamiltonian, by starting from first principles considerations. In particular, two families of such approaches can be found in literature: one is the "embedded-atom-method" (or EAM), the other is in connection with the tight-binding model.

Daw and Baskes [16,17,18] describe the EAM of treating metallic systems where fractures, surfaces, impurities can be included. This method is based on the earlier "quasi-atom-theory" [16]. In this scheme an impurity (called quasi-atom) is assumed to experience a local uniform or only slightly non uniform environment (uniform density approximation). In other words, each atom of the metal is seen as an impurity embedded in a host, com-

prising all the other atoms. In the density functional theory framework by Hohenberg and Kohn [19], using the uniform density approximation, the energy of this impurity can be written as a function of the host electron density (before the introduction of the impurity) $n_h(\vec{r})$ at the impurity site $\vec{R}$

$$E_{imp} = F(n_h(\vec{R})). \tag{1.13}$$

In the EAM the total energy of a solid can be calculated from the embedding energy. So they take the following ansatz for the total energy

$$E_{tot} = \sum_i F(n_i) \tag{1.14}$$

where n_i is the electron density at the site of atom i of a system in which atom i is missing. n_i can be approximatively constructed as a superposition of atomic densities:

$$n_i = \sum_{j,j\neq i} \rho(r_{ij}). \tag{1.15}$$

Here $\rho(r)$ is the electron density distribution of a free atom, taken from Hartree-Fock calculations. If we add a two-body potential to account for the core-core repulsion, the Daw and Baskes Hamiltonian is formally identical to the glue Hamiltonian. Also in their scheme it is necessary to use an empirical fit procedure to find the optimal functions for a given metal.

However, the function $\rho(r)$ is fixed in EAM, while it is available for the fit procedure in the glue scheme. Another difference is that n is the electron density in the EAM, while in the glue scheme it is simply an auxiliary variable which is similar to the atomic coordination.

A Hamiltonian based on the same spirit as the glue Hamiltonian has been proposed by Finnis and Sinclair [20] to calculate vacancy and surface energies in bcc transition metals. Their Hamiltonian contains a central pair potential and a many-body term (similar to the glue); its dependency from the coordination n_i has the analytic form

$$U(n) = -A\sqrt{n}. \tag{1.16}$$

Also in this case the coordination n_i depends from a density function $f(R)$, $n_i = \sum_j f(R_{ij})$, which, with the two-body potential $\phi(r)$, is built

empirically, fitting to experimental data for a perfect crystal many physical quantities.

The particular form for $U(n)$ in Eq. 2.16 comes from the second-moment approximation to the tight-binding model [21].

A similar scheme in which the role played by the atomic coordination is very important, has been developed by Tománek and Bennemann [22].

In their model surface reconstruction is a result of the minimization of the surface free energy, which at $T = 0$ reduces to the surface energy γ given by

$$\gamma = \frac{1}{N_S} \sum_{i=1}^{N_T} [E_{coh}(bulk) - E_{coh}(i)]. \tag{1.17}$$

N_S is the number of surface atoms, N_T the total number of atoms in the crystal; $E_{coh}(i)$ denotes the atomic binding energy of an atom at site i. $E_{coh}(i)$ is decomposed into an attractive band structure and a repulsive Born-Mayer part.

The model assumption of a single band solid, of local charge neutrality and the same band-shape (except for a rescaled band-width) at each site, allows to relate the band structure energy at each site to the bulk value, without assuming a model density of states (rectangular or Gaussian, for instance), which is a very simplification in the theory.

The repulsive part of $E_{coh}(i)$ is proportional to the coordination number Z, and can be therefore expressed using pairwise interactions, while the attractive part is, like in the Finnis-Sinclair Hamiltonian, proportional to $Z^{1/2}$.

They apply their general simple theory to study multilayer relaxations at fcc and bcc surfaces. At the surface with a lower coordination number $Z_{surface} < Z_{bulk}$ the attractive part of $E_{coh}(i)$ outweighs the repulsion and induces a surface contraction. This contraction, however, simulates a higher coordination number $Z > Z_{bulk}$ in the second layer with full bulk coordination. In this region the repulsion outweighs the attraction and causes an expansion of the next interlayer distance. In this way a damped oscillatory relaxation is induced in the following layers.

Within this model it has been possible to obtain damped oscillatory multilayer relaxations and predict results for the reconstruction at clean (110) and (100) surfaces of Ir, Pt, and Au.

1.4 Molecular dynamics for the glue model

Standard molecular-dynamics (MD) [23] have been used to investigate a variety of bulk and surface systems, using the glue force model introduced in the previous Sections.

Very briefly we can say that by MD, one can manipulate a system of N interacting particles to bring it to the desired thermodynamic state. The initial positions and velocities can be chosen in a variety of ways; we have used as initial positions regular arrays of points of opportune geometry, with suitably randomized small displacements and all zero-velocities. Starting from these initial conditions, the time evolution of the system is followed by numerical integration of the classical Newton's motion equations. If the system under study is ergodic, thermodynamic informations can be extracted by time averaging over runs of adequate length.

Following Rahman [23], the total energy E of such a system, which is a conserved quantity (microcanonical ensemble), is given by:

$$E = V + \frac{1}{2}\sum_{i}^{N} m_i \dot{r}_i^2; \tag{1.18}$$

the reduction of all $\dot{r}_i$ by a factor $\alpha < 1$ will reduce the energy E and vice versa for $\alpha > 1$. The choice of α, and the frequency with which it is applied varies according to circumstances. At this point, we can introduce the temperature scale for measuring the kinetic energy. Writing

$$\frac{1}{2}\sum_{i} m_i \dot{r}_i^2 = \frac{3}{2} N k_B T(t) \tag{1.19}$$

we shall say that the system has a certain "temperature" T at time t to imply that it has total kinetic energy at time t equal to $\frac{3}{2}Nk_BT(t)$. The average of $T(t)$ over a sufficiently long dynamical run will be referred to as the temperature of the system for that run.

Using this terminology, the reduction or increase in E, the total energy, is achieved by "cooling" or "heating" the system. Heating the system, has some problems; in fact if $T(t)$ at any moment t is high enough, the system will dissipate by a process of evaporation or explosion, depending on the circumstances. Also the cooling of the system has some limits. Firstly, the factor α equal to 0 is the ultimate in reducing the temperature at time t

to 0; however, immediately afterwards, the temperature will start rising by conversion into kinetic energy of some of the potential energy of the system at time t; thus, drastic temperature reduction cannot be achieved in one step; secondly, as the system is cooled, it gets more and more sluggish and takes longer and longer to sample the configuration space available to it.

It is therefore clear that MD can be also effectively used as an energy minimization tool, by removing kinetic energy from the system until the particles have reached an equilibrium position. To this purpose, we have used two different methods:

(a)"quenching", by which the system is driven, by a direct cooling, towards the nearest (or one of the nearest) energy local minimum; this is practically obtained by scaling the velocities by $\alpha < 1$ at each time step of the simulation;

(b)"simulated annealing", by which the system is thermally annealed at finite temperature, and then gradually cooled down to T = 0.

We must observe that with the quenching procedure, even if faster, the danger of trapping in a local energy minimum is high. Simulated annealing requires more computer time, but energy barriers can be overcome and the real energy minimum can be reached, if it is deep enough, even if the initial conditions were very far from this minimum. With respect to this, energy minimization using simulated annealing offers a clear advantage over traditional methods [25].

The problem of MD is to convert differential equations into a set of difference equations, which enable us to go from time t to $t + \Delta t$ with a suitably chosen Δt. This can be done with various algorithms. In our calculations, it has been used a fifth-order predictor-corrector algorithm, which can be found in a report by Gear [26].

The calculation of the forces is the most consuming part of the whole simulation, so that particular attention has to be paid so as to make it as efficient as possible. For this reason, the three functions $\phi(r)$, $\rho(r)$, $U(n)$ are pre-calculated and stored in tables, and quick numerical interpolations are performed by the program. Square-root computations can be avoided by tabulating $\phi(r)$ and $\rho(r)$ at constant r^2 (instead of r) intervals.

The standard MD programs, based on two-body interactions, can be easily extended to include the glue forces [14], given by:

$$\vec{F_i} = -\nabla V = -\sum_j \phi'(r_{ij})\frac{\vec{r_{ij}}}{r_{ij}} - \sum_j [U'(n_i) + U'(n_j)]\rho'(r_{ij})\frac{\vec{r_{ij}}}{r_{ij}}. \qquad (1.20)$$

The glue Hamiltonian is particularly convenient from the computational point of view, since the atomic positions appear only in the form of distances between pairs. In spite of the intrinsic many-body character of the glue, there are no explicit three-body or more complex terms in this expression.

To include the glue forces in MD programs, the number of computations required with respect to a pairwise system is roughly doubled. The procedure requires two passes over all the interacting pairs. In the first pass, the two-body forces and the total coordination are calculated for each particle. In the second pass, the glue forces are computed. This splitting is necessary because all the coordination n_i must be known to calculate the glue forces.

An important physical remark to do about the expression which gives the forces, is that $\vec{F_i}$ depends on the value of n_j for all atoms j, whose distance from i is less than r_m, the cutoff of $\rho(r)$. But n_j, in turn, depends on the positions of all atoms k within a distance r_m from j. Thus, an atom k, at a distance up to r_m influences the force acting on i, so that the "effective interaction range" of the glue forces is twice the range of $\rho(r)$. In a fcc structure, this means that a first neighbours ranged $\rho(r)$ can couple together neighbours up to the seventh shell.

A procedure, which avoids the expensive computation, at each time steps, of all the $N(N-1)/2$ distances is that invented by Verlet. One can state that for several Δt of MD, the neighbours up to a distance r_c, which is linked to the cutoff of the potential will be, in large majority, unchanged. A few move out of range r_c and a few will move within range. Thus, if at any moment we construct a list of neighbours not up to r_c, but up to $r_c + S$, where S denotes a skin thickness, then for several Δt after that moment, we need to consult only this list (and not the whole system) to identify the neighbours up to r_c and to throw away those beyond r_c. It could be shown that there is an optimum balance between the value of S and the number of Δt for which the list, once made, may be used.

The Verlet method is useful when dealing with moderately large systems. For very small systems (N from 100 to 200) such procedure is not of any use, and for very large systems (N larger than 5000) further elaboration of the procedure becomes necessary.

For what concerns periodic boundary conditions (pbc), that enable us to extend a parallelepiped box to infinity by an integral number of translations in the three directions, one can observe that for potential functions which are short-ranged, as our glue, compared to half the box size, the effect of pbc will be rather small.

In visualizing a system with pbc, it may be convenient to think in terms of a box with walls and particles "entering" from one face when leaving from the opposite face. However, since the box can be drawn anywhere in space, as long as it has the correct size and it is never tilted, one can always think of any particle as being at the center of the box rather than at one face or another. Both ways of visualizing pbc are equally valid.

Another consideration to do is that, when a particle goes beyond $\pm L/2$, where L is the measure of the box supposed cubic, it has to be reset so as to bring it back into the box from the opposite face. This operation simply recognizes that the image is already in the box and transfers the particle tag to its image.

When we study by MD a physical system with surfaces, we usually represent it by a "slab", i.e. a seminfinite system composed by a certain number of parallel layers with pbc only in the two in-plane directions (x and y) of the layers. In the direction z not subjected to pbc we choose the thickness of the slab in such a way that the two surfaces do not interact, or equivalently that the physical quantities do not depend any more on the chosen number of the layers.

Chapter 2

Previous applications of the glue model

2.1 Bulk and surface properties of gold

Using the standard MD technique, discussed in Section 1.4, the bulk thermal properties of gold have been studied, within the glue Hamiltonian. We can list very briefly the most important results, referring for a detailed description to Ref. [14].

(a) It has been proved the stability of the fcc structure of gold against the bcc structure up to the melting temperature, in the absence of pressure or stress. Such transition might happen, in fact, also spontaneously if at a certain temperature the two phases have the same free energy. For this purpose, a version of the MD program, using the Parrinello-Rahman technique [24], in which changes in the shape of the MD box are allowed, has been used.

(b)The variation of the lattice parameter with temperature is in good agreement with experimental results.

(c)The melting temperature obtained, $T_M = 1357 \pm 5$ K, is well comparable with the experimental value $T_M = 1336$ K. T_M has been determined as the temperature at which a liquid-solid interface remains stationary.

(d) The pair correlation function of the liquid has been calculated. The results show that there is a good agreement on the position, height, and width of the first peak. The calculated $g(r)$ has, however, the first minimum too deep and the second shell slightly too close when compared with the

experimental $g(r)$.

(e) The vacancy formation energy, taking into account the relaxations of the atoms around the vacancy, is also reproduced fairly well.

Besides bulk properties, the glue model can reproduce well also some particular gold surface properties, in particular the occurrence of reconstruction on all low Miller index surfaces (100), (110), (111) [28,29]. While, for Au(100) and Au(110) we report in the two next Sections the most important results predicted by this model, we refer to the next Chapter for a detailed description of all problematics concerning the Au(111) surface.

As a general consideration valid for all surfaces, to get the $T = 0$ surface energies σ, we have used the above described energy minimization strategy based on MD. To compute σ, we have used n layers-slabs, with suitable dimensions in x and y directions ($M \times cL$), where pbc are active. M is the size in x-direction, L in the y-one (in units of d =2.88 Å, first-neighbours distance); c is a geometrical factor, which depends by the geometry of the surface examined. σ is given by

$$\sigma = \frac{E(N) - N\epsilon_c}{2A}, \tag{2.1}$$

where N is the total number of particles in the sample, $E(N)$ the total energy of the slab (computed by MD), ϵ_c the cohesive energy per atom (3.78 eV/atom for Au), A the slab area and the factor 2 accounts for the 2 surfaces on the slab.

The xy size of the MD box must contain, of course, an integer number of surface unit cells. Surface reconstructions with long periodicities can therefore be studied only by using very large, appropriate MD boxes.

Moreover, reconstructions in noble metals usually imply the presence of a number of atoms N larger than in the corresponding non-reconstructed structure. Since N is conserved in MD, the extra atoms must be added from the beginning. This has been done in different ways, as discussed in more detail in the following.

For completeness, we recall that the glue model has been applied also to small clusters of atoms [14,27], where surface forces presumably play a crucial role in determining the structure. Usually reconstructed surface layers quite often yield a better energetics. Generally, cuboctahedra result

to be energetically favoured. However, amorphous clusters of high stability are also uncovered, which for $N < 200$ become favoured over clusters with a "crystalline structure".

2.2 Au(100) surface reconstruction

2.2.1 Experimental studies

It is now well established that the Au(100) surface reconstruction is characterized by a close-packed hexagonal overlayer on a square substrate. The first, low resolution LEED measurements indicated a (1×5) reconstruction cell [30,31]. This pattern was interpreted as due to a geometry where six rows of atoms lie on top of five [011] (henceforth y-direction) rows of substrate atoms in a $[01\bar{1}]$ (henceforth x-direction). This arrangement requires a 3.77% contraction of a perfect triangular lattice in the 6-onto-5 direction.

Later, LEED measurements with improved resolution [32] suggested (20×5) as a better unit cell for the reconstruction. This was interpreted to imply a small contraction also in the x-direction, so as to accommodate one extra row over 20 $[01\bar{1}]$ substrate rows.

In a RHEED study Melle and Menzel [33] confirmed the previous (20×5) model, although they mentioned some discrepancies from the LEED results in detailed points.

Subsequently LEED [34] and He scattering studies [36] suggested a much larger unit cell such as $c(26 \times 68)$.

In a recent STM real space investigation Binnig, Rohrer, Gerber and Stoll [35] propose a $\begin{pmatrix} 26 & 0 \\ z & 48 \end{pmatrix}$ unit cell where $-5 \leq z \leq 0$, implying the possibility of small rotation (about 0.1 degrees) of the whole overlayer over the substrate.

Very recent TED and TEM analysis [37] confirm the rotations of the hexagonal lattice with respect to the underlying square lattice. The hexagonal lattice results contracted by about 3.6% and 3.3% in the multifold and fivefold directions respectively. The superstructure has been found $(p \times q)$ with $p \simeq 28$ and $q \simeq 5$ and it has been interpreted as a periodic arrangement of the two kinds of the (1×5) reconstruction.

It may be interesting to observe that in TEM and in TED analysis the

periodicity of the superlattices in the five-fold direction fluctuates largely around $q = 5$ and reaches even $q = 4$ and $q = 6$. This uneven periodicity suggests that the periodicity is bounded by values which are commensurable with the lattice constant.

The long periodicity of 48 deduced by LEED, for example, can be due to a periodic array of commensurable periodicity ($q = 565565565..$) giving rise to an average value of 5.3 (48/9). Unevenly spaced superlattice fringes are often seen on narrow terraces in TEM images, while they are not noticed on experimental studies of flat rotated superlattices. So this effect might be caused only by steps and might have been concealed on flat surfaces.

These detailed studies by TEM and TED have clarified also the problem of the rotation of the hexagonal lattice with respect to the underlying square lattice, which seems an intrinsic peculiarity of the flat Au(100), going to disappear on stepped regions.

Profile Imaging [38] studies also confirms the (28×5) supercell, with a corrugation of the topmost layer with a period of about 14 Å. The observed amplitude of the corrugation (0.3 − 1.1 Å) is similar to the values (0.4 − 1.2 Å) reported by STM [35].

Detailed experimental studies on stepped reconstructed Au(100) have been also done, and they will be reviewed in Chapter 4.

2.2.2 Au(100) surface reconstruction at T=0 in the glue model

An investigation of the Au(100) surface structure predicted by the glue Hamiltonian has been carried out previously using standard MD [12,13]. This has been done by studies of 14-layers slab with in-plane periodic boundary conditions and initially $5\times5 = 25$ atoms per (100) plane. The area of the slab and its square shape have been kept rigid to prevent transformation into a (111) slab.

This procedure has been initially applied to the clean, unreconstructed (100) faces. In the first atomic layers, after annealing, one can note that the surface atoms have shrunken together, leading to formation of close-packed stripes (five atomic rows each) separated by a gap. This configuration has a surface energy of 109.6 meV/Å^2. This gap in turn can be seen as leading to the formation of two atomic steps, here very near to one another (as it is seen in Fig. 2.1). The second layer has remained a basically perfect (100)

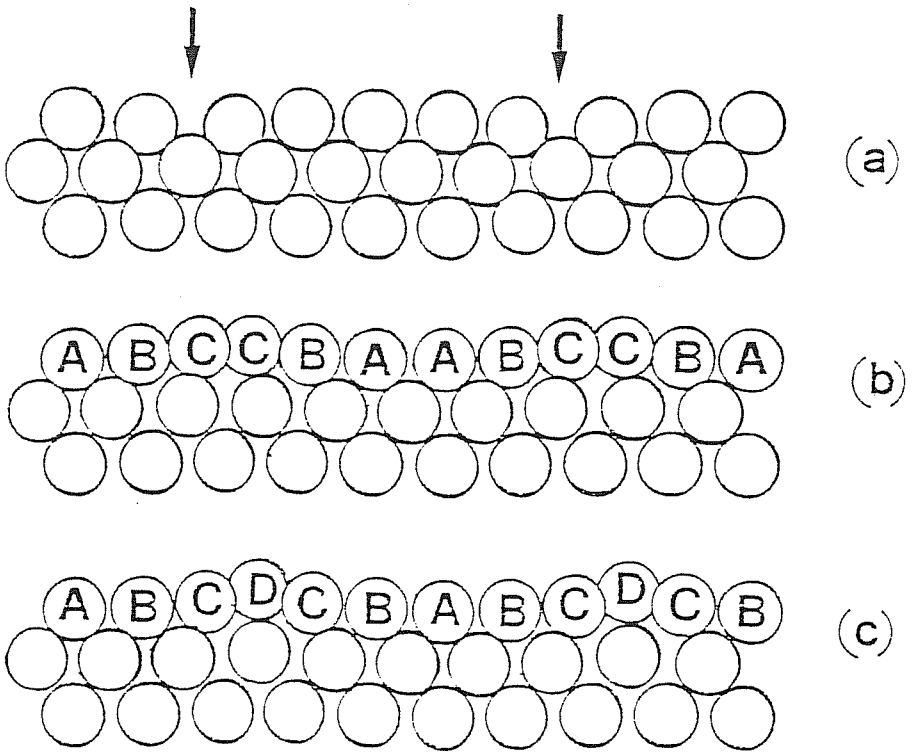

Figure 2.1:
Configurations of (100) slab after thermal equilibration and subsequent annealing. Two molecular dynamics cell in [011] direction with 3 layers in the [100] one are shown.
(a) The starting configuration was a perfect (100) slab. The atoms have shrunken in 5-rows wide stripes, leaving a gap (indicated by the arrow) in between; $\sigma = 109.6$ meV/Å^2.
(b) Respect to (a) 5 atoms have been added in the starting configuration. They are absorbed, giving rise to a 20% denser quasi-triangular reconstructed first layer with a $ABCCBA$ stacking; $\sigma = 102.3$ meV/Å^2.
(c) Respect to (b) the registry is different and the stacking is $ABCDCB$; $\sigma = 102.6$ meV/Å^2.

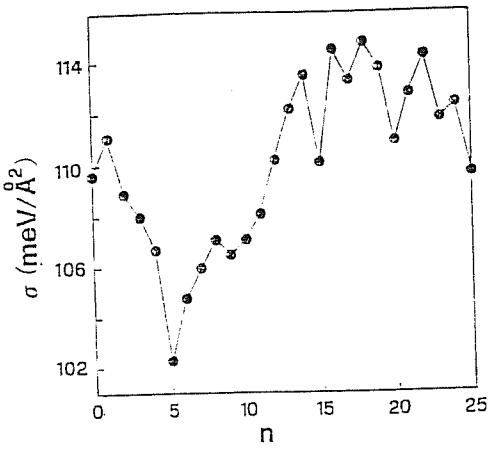

Figure 2.2:
Surface energy versus the adatoms present in the starting (5 × 5) (100) slab. The minimum is at $n = 5$ ($\sigma = 102.3$ meV/Å^2).

plane.

Instead, by a careful quench of a perfect crystal, not preceded by heating and thermal equilibration, a relaxed but perfect (100) surface has been produced. Its surface energy, however, is higher than that of the configuration with the gaps (128.5 meV/Å^2 vs. 109.6 meV/Å^2). Furthermore, such structure is unstable.

The formation of close packed stripes on the annealed samples is a clear indication that the Au(100) surface wants to reconstruct into a denser layer, even within the constraint of this small 5×5 cell. To test this, it has been done a series of runs where a number n of extra adatoms is added on top of the first layer; n is varied from $n = 1$ to $n = 25$. For n small, the extra atoms are absorbed into the first layer giving rise, after annealing, to a denser packing. A minimum in $\sigma(n)$ is obtained for $n = 5$ (102.3 meV/Å^2) (Fig. 2.2).

The fact that the minimum in $\sigma(n)$ is obtained for $n = 5$ in a (5 × 5) cell, has brought to the conclusion that the best configuration is given by a (1 × 5) superstructure with 6-onto-5 atoms in y-direction [011]; σ for this configuration is 102.3 meV/Å^2 (Fig. 2.1).

The amplitudes of the corrugation predicted for the first four layers are $\delta_1 = 0.47$ Å, $\delta_2 = 0.21$ Å, $\delta_3 = 0.13$ Å, $\delta_4 = 0.08$ Å. The relaxations of the distances between average layers positions are $\Delta d_{12}/d_{12}^0 = +3.6\%$, $\Delta d_{23}/d_{23}^0 = +2.2\%$, $\Delta d_{34}/d_{34}^0 = -0.2\%$. The increase of the distance between the first and the second layer, and the second and the third may appear unusual for a metal. However, it is an inescapable consequence of the glue Hamiltonian, where coordination plays a key-role. The first layer

Structure	σ (meV/Å^2)
(1×3) relaxed	108.6
(1×8) relaxed	103.3
(1×5) relaxed	102.3
(1×12) relaxed	103.2
(1×7) relaxed	103.7
non-reconstructed, ideal	143.1
non-reconstructed, relaxed	128.5

Table 2.1:
Surface energies values for several (100) geometries. $(1 \times 7), (1 \times 12), (1 \times 8)$ are configurations of the kind 8-onto-7, 14-onto-12, 10-onto-8 rows, while $(1 \times 3), (1 \times 5)$ are of the kind 4-onto-3 and 6-onto-5 rows.

reconstruction, while not succeeding in raising the first layer coordination to 12, has the effect of increasing that of the second layer above 12. Outwards relaxations of the first layer relative to the second (and of the second relative to the third) is required just to keep the second layer coordination from getting too high.

The stacking of the rows is $ABCCBA$; a local energy minimum has been also found at another stacking $ABCDCB$ (Fig. 2.1). In this arrangement the surface energy is slightly higher and the corrugation is larger ($\delta_1 = 0.74$ Å). In all cases this strain is not uniformly distributed: the surface density is higher in a hilltop row, and lower in a valley row, where the atoms are not far from their ideal hollow site positions over the square substrate.

It has been examined also the role played by the cell size in these calculations; so various cases have been examined corresponding to the different cell sizes, as seen in Table 2.1. All these surfaces reconstruct into a denser overlayer, but their surface energies are all higher than the (1×5) $ABCCBA$ structure. We observe that the (1×4) and (1×6) cannot be realized with a single surface unit cell because for the triangular reconstruction an even number of rows is required in the topmost layer.

For completeness we recall briefly that also the reconstruction in x-

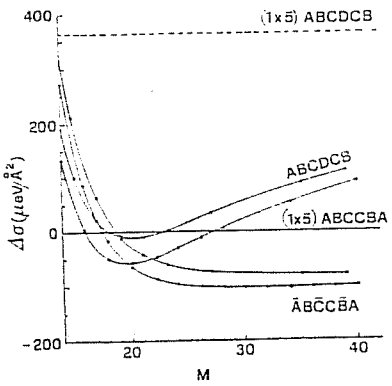

Figure 2.3:
Differences of σ of $(M \times 5)$-reconstructed $ABCCBA$ slab, as a function of M. The two basic y registries ($ABCCBA$ and $ABCDCB$) show a slightly different behaviour.

direction has been considered, following the suggestion of many experimental studies. The optimal contraction in the x-direction at $T = 0$ has been searched by studying the surface energies of reconstructed $(M \times 5)$ 12-layers-slab. It has been found that generally the odd M cells cost more energy to realize that the even M cells and that the best configuration is (34×5), but the minimum of σ is so flat as to make this precise value almost meaningless. Any value of M between 28 and 38 is about equally good (Fig 2.3). In particular the surface energy of (34×5) is only 0.003% less than (26×5), which is a unit cell very close to the suggested experimental cell (26×48).

In the y-direction the best structure remains the $ABCCBA$, but some of the small distortions that take place break the exact mirror-plane symmetry, giving rise so, effectively to an $\overline{A}B\overline{C}C\overline{B}A$ structure (Fig. 2.4). All details of the structure of this surface can be found in [13]. We want only recall that the strain in the x-direction is concentrated in highly corrugated regions which have a one-dimensional soliton appearance, with a width of about 10 Å. These solitons form a two-dimensional lattice six of them for each rectangular unit cell of size (34×5). Except for a small distortion, this arrangement corresponds to a centered rectangular lattice with two solitons per cell, of size $(34 \times 5/3)$.

In the dilute limit, i.e. M very large, from the fit of the soliton-related change in the energy $\Delta\sigma$, it is possible to extract the soliton-chemical potential (-48 meV) and the effective soliton-pairwise repulsion (1370 meV).

In the regions between the solitons, the corrugation-pattern in z, along y-direction, shows a single-maximum-single-minimum structure ("smooth" stripes), with a total excursion of 0.48 Å, in the middle of the area; on top

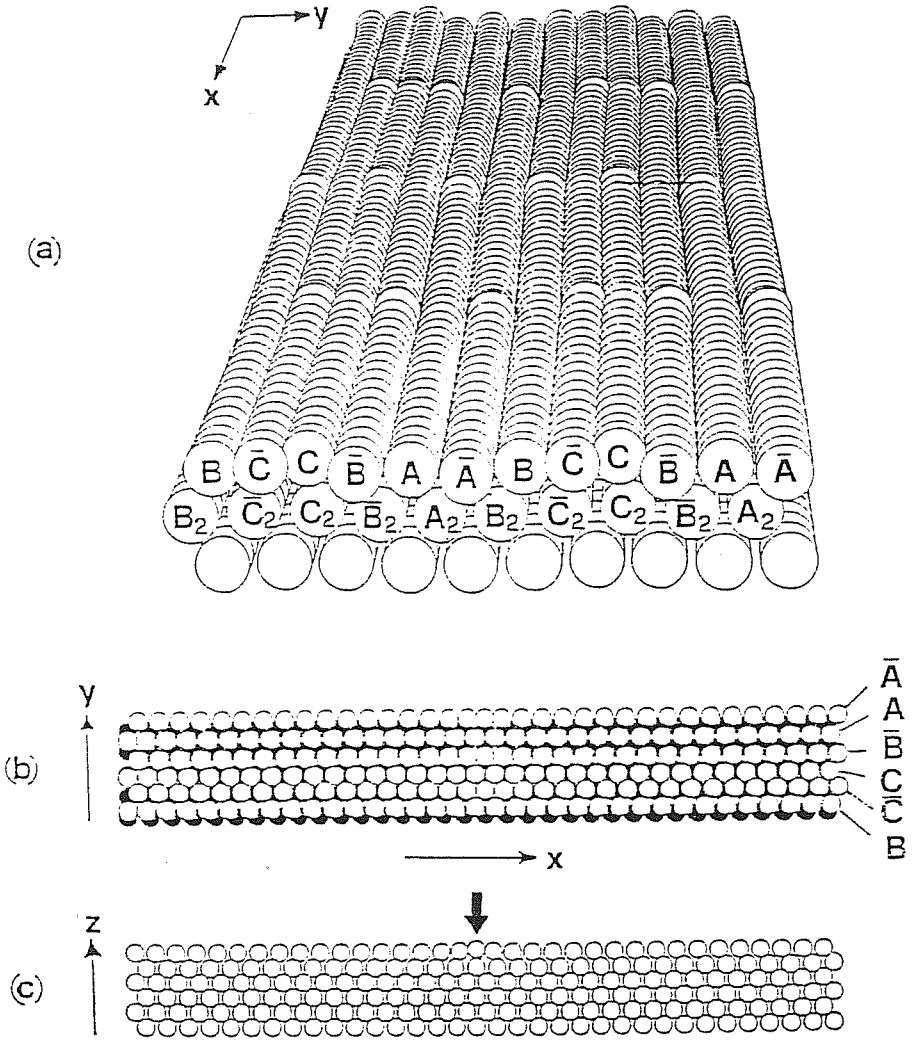

Figure 2.4:

The optimal $ABCCBA$ (34×5) surface.

(a) Perspective view, showing the soliton lattice. Two cells along x and y are shown.

(b) Top view of the first (white atoms) and the second (black atoms) layer.

(c) Side view of the first six layers. The first layer (a $\overline{B}$ row is shown) has a soliton in the middle.

of the solitons, instead, the corrugation in z, along y, is double-maximum-double-minimum, with a total swing of 0.80 Å ("rough" stripes). These morphological features compare well with STM experimental results [35]. The most serious difference is that the smooth stripes in the glue model are wider than the rough stripes, while in the STM picture their width seems nearly equal (about 20 Å). This difference might be due to temperature smearing effects.

From soliton theory, which will be explained in more detail in the next Chapter, we expect an arctg-behaviour for the phase ϕ_k of the solitons, defined for a given row as

$$\phi_k = \frac{2\pi}{d}(x_k - kd + b) \tag{2.2}$$

where k is an index running from 1 to 35 (number of atoms in a top row for a bulk cell of 34), x_k is the x-coordinate of atom k, d is $a/\sqrt{2}$ and b is a constant (equal for all the rows). We have referred the phase angle to an ideal perfect square lattice rather than to the actual substrate layer, which is slightly distorted. It is apparent in Fig. 2.5 that the 360^0 total

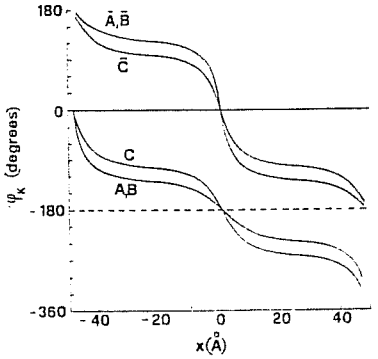

Figure 2.5:
Soliton phase (Eq.2.2) as a function of x for each row.

phase shift within a cell is achieved by a row through two distinct steps: a larger phase-shift across the soliton-region and a smaller phase-shift, when the row runs between two solitons.

The difference in energy between the even- and odd-M cases is related to a difference in the shape of the solitons, as explained in detail in Ref. [13].

The second and deeper layers, which have not reconstructed, have not retained their perfect square lattice positions. On the contrary, the second layer is severely strained and warped. Moreover, some "multilayer relaxations" propagate down to the third and fourth layers.

Finally, the average interplanar distance is also modified. By averaging over all atoms of each layer, we obtain Δd_{12}=+5% ($\Delta d_{12} = (d_{12} - d^o_{12})/d^o_{12}$; d^o_{12} is the bulk interplanar spacing), Δd_{23}=+2.1%, $\Delta d_{34} = -0.3\%$.

It may be interesting to note that the EAM of Daw and Baskes, used to calculate the reconstruction of the Au(100) surface [39], gives very similar results to those obtained by EPT [12] for the (1×5) reconstruction. However, the values for surface energy differ considerably with the predictions by EPT, and with estimates based on experimental data [40], being smaller by roughly a factor of 5.

For what concerns the observed rotation of the nearly-triangular topmost layer respect to the square-substrate [35], which was not considered at all in the calculations made by the glue model, we refer to Okwamoto and Bennemann [41]. They describe the top atomic layer as a two-dimensional isotropic continuum influenced by a square-net substrate potential, which can be expanded in Fourier series.

The Au(100) top layer lattice is described as incommensurate in two directions. The rotation observed at the Au(100) surface is explained as the Novaco-McTague rotation, observed for rare-gas monolayers on the basal plane of graphite, dominated by particular Fourier components ($V_{\pm 3 \pm 1}$) of the substrate potential. The extremely small rotation angle, from their calculation, results from the competition between the components V_{31} and V_{3-1}.

Their theory, which has been applied also successfully to the Au(111) surface reconstruction and which will be described in more detail in the next Chapter, is similar to that used for physisorbed gas-monolayers [42].

2.3 Au(110) surface reconstruction at T=0 in the glue model

A large amount of experimental data is available for the Au(110) surface. They have been obtained by LEED, He diffraction, low, medium and

high-energy ion scattering, STM, X-ray diffraction and TEM ([29]). These data show strongly that Au(110) (together with Ir and Pt (110)) exhibits a (1×2) reconstruction, meaning that the surface unit cell length is the same as in a truncated bulk along the $[\bar{1}10]$ direction, while it is twice as long along [001]. By now it is well established that the surface structure, giving rise to this reconstruction pattern, is the so-called "missing-row" structure, where every other $[\bar{1}10]$ row is missing on the topmost layer. Occasionally also $(1 \times n)$ unit cells, with $n = 3, 4$, are occasionally observed [44,45]. These are also interpreted in terms of the missing-row model.

A $(1\times n)$ missing row model consists of $n-1$ rows missing in the topmost (110) layer, $n-2$ in the second layer, and so on. This gives rise to (111) facets (each of them $n+1$ $[\bar{1}10]$ rows wide), forming an ideal angle of about 35^0 with the flat (110) surface plane.

Using MD as a tool for searching the energetically optimal configuration predicted by the glue Hamiltonian, simple quenching and annealing-quenching procedures have been applied to (110) slabs of sufficient thickness (twelve to twenty-four layers) and variable lateral (x, y) size with in-plane periodic boundary conditions [29,43].

In this case the optimization is not a "complex problem" because with both procedures the same minimum is obtained, differently from what happens for the Au(111) surface (see Chapter 3). This procedure has been applied to a flat Au(110) and then to the $(1 \times n)$ missing row reconstruction models.

The results are summarized in Table 2.2.

First of all, the (1×2) missing row structure turns out correctly to be the optimal structure. The surface energy gain of the relaxed (1×2) missing row with respect to the ideal bulk termination amounts to about 30%, of which about 10% comes from removing the missing rows and the remaining 20% from allowing subsequent relaxations. The energies of the $(1 \times n)$ missing row structures with $n = 3, 4, 5, 6$ are very close to the optimal surface energy. This confirms the suggestion of Binnig et al.[45], that the driving force for the Au(110) reconstruction is the tendency to form (111) facets, which is due in turn to the low (111) surface energy compared with that of the unreconstructed (110). In the glue model, atoms on a (111) face are energetically favoured by their high coordination number. In fact, as Table 2.2 shows, even the surface energy of a 35^0-tilted (111), corresponding to the $(1 \times \infty)$ limit, is lower than that of a relaxed (1×1) (110) either

Structure	σ ($meV/Å^2$)	Δd_{12} (%)	Δd_{23} (%)	Δd_{34} (%)
(1×1) ideal	150.4	0	0	0
(1×2) ideal	139.5	0	0	0
(1×1) relaxed	122.5	-33.9	+6.9	+1.3
(1×2) relaxed	107.4	-27.5	-4.7	-2.2
(1×3) relaxed	109.8	-30.8	-4.8	-10.2
(1×4) relaxed	109.5	-31.9	-5.2	-8.3
(1×5) relaxed	109.4	-36.0	-6.9	-10.0
(1×6) relaxed	110.0	-33.1	-14.1	-8.3
(1×∞) rel.(111)	118.3			
(1×∞) rec.(111)	108.0			

Table 2.2:
Optimal σ and multilayer relaxations for various models of Au(110). All the structures except the (1 × 1) are of the missing-row type; the values relative to (1 × ∞) are based on (111) surface energies; σ^{id}_{111}=105.1 meV/Å^2, σ^{rel}_{111}=96.6 meV/Å^2, σ^{rec}_{111}=88.1 meV/Å^2; these values for Au(111) surface are obtained in Chapter 3.

when the (111) is taken to be not reconstructed (118.3 vs 122.5 meV/Å^2) or reconstructed (108.0 vs 122.5 meV/Å^2).

The optimal (1×2) relaxed structure is shown in Fig. 2.6. In the inset, a view from the top, shows the sliding distortion of the top row atoms relative to the third layer atoms underneath. It can be seen that there is a large inward relaxation of the top row $\Delta d_{12}/d^0_{12} = 27.5$ %. Distortions of deeper layers are also present. The second layer shows a "pairing distortion" of the rows, which move slightly inwards, that is towards the top rows. The third layer undergoes a large buckling of total amplitude 0.37 Å. The atoms below the top rows are "pushed down" by them, while the others are not, and "float". By averaging the z-coordinates in each layer, there is indication of overall contraction also below the surface layer. All these features of the structure are in qualitative agreement with experiments, while in the detail the distortions obtained are a little too large.

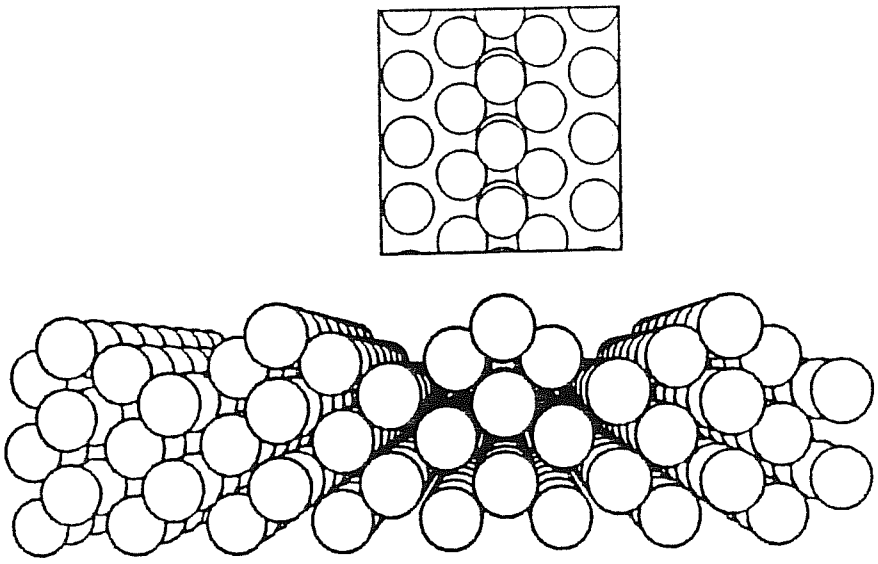

Figure 2.6:
Side view of the optimal Au(110) (1 × 2) "missing row" structure. The top row contraction, the second layer inwards pairing and the third layer buckling are visible.

Finally, all the relaxed structures exhibit a small sliding distortion of the top rows along $[\bar{1}10]$, i.e., parallel to themselves. On the optimal structure the distortion amounts to 0.26 Å for the top row atom and to 0.06 Å for the third layers atoms underneath. A MD study at finite temperature has shown that at around 230 K there is a phase transition by which the full average symmetry is restored. It is not well-established whether the true Au(110) should have a similar phase transition, or whether it is an artifact of the glue model.

Implications of the complex reconstruction/relaxation pattern of the missing-row surfaces on the surface dynamics, and in particular on the surface phonon spectrum, have been studied in detail [46]. In this work, as a typical signature of the missing row reconstruction, the existence of anomalous high frequency modes has been predicted.

The dynamical behaviour of the Au(110) missing-row surface in the glue model has been investigated by using MD, instead of the standard lattice dynamics. In fact by MD it is easier to take in account complex distortions, anharmonic interactions and temperature effects, including possible diffusive motions and phase transitions. Approximate surface phonon spectral

densities are extracted from the trajectories through the $\vec{k}$ resolved, first-layer velocity-velocity correlation functions.

The main striking feature of the spectrum obtained consists of two anomalous high frequency surface modes with rather flat dispersion (H_1, around 20 meV, and H_2 around 17 meV). To clarify their origin, it has been made a separate study of their eigenvectors. At $\vec{k} = 0$ they are so characterized :

(a) in mode H_1 the top rows atoms and the third-layer atoms just beneath move essentially along z, while the second-layer atoms move mainly along y with a small z component. These four atoms move essentially towards (or away from) their center of mass, thus clarifying the large stiffness of this mode. Third-layer atoms below the missing rows remain almost motionless. This form of this eigenvector indicates that this high frequency mode arises because of the deep sinking of the topmost row, giving rise to a stiffening of surface force constants.

(b) In mode H_2, all motions are essentially along y and only second-layer atoms exhibit some z component. This mode is very close to the bulk mode, and might be difficult to detect in practice, differently from the H_1 mode which should be easily detectable by either inelastic He-scattering or by electron-energy-loss-spectroscopy.

Chapter 3

Au(111) surface reconstruction

3.1 Review of the experimental facts and the proposed models

3.1.1 Experimental results

Concerning the surface reconstruction of gold, we know since earlier work by Fedak and Gjostein [30] that the gold surfaces (100) and (110) exhibit superstructures, respectively (1×5) and (1×2), but the (111) surface was generally described as an unreconstructed one [47,48]. However LEED photographs of Au(111) obtained during these studies, exhibit large areas of intensity at the integral order reflection positions, instead of sharp narrow beams.

Then, in 1974, Perdereau et al. [49] have observed by LEED a superstructure on a (111) gold surface. According to these authors, the outermost layer looks like an hexagonal one, compressed by nearly 5% compared with the layer in the bulk.

Zehner and Wendelken [50], using the same technique, have found that the geometry of the reordered layer is similar to that described by Perdereau et al. [49], but the compression is only 4%.

More recently, Melle and Menzel [33] have observed by RHEED a $(p \times \sqrt{3})$ superstructure with $p = 22 - 23$ of the Au(111) face; in the $[11\bar{2}]$ direction the outermost layer has the same parameter as the bulk, but in the perpendicular $[1\bar{1}0]$ direction, it is compressed by 4.2%. Therefore, the

surface net has only a twofold symmetry instead of a sixfold one.

The same superstructure has been observed by Yagi et al. [51,52] by UHV TEM and by Heraid and Metois [53] by TED.

Tanishiro et al. [2] have been the first who have studied the temperature dependence of the diffraction spots, increasing the temperature (Fig. 3.1). Their TEM and TED observations have led to the following scheme of

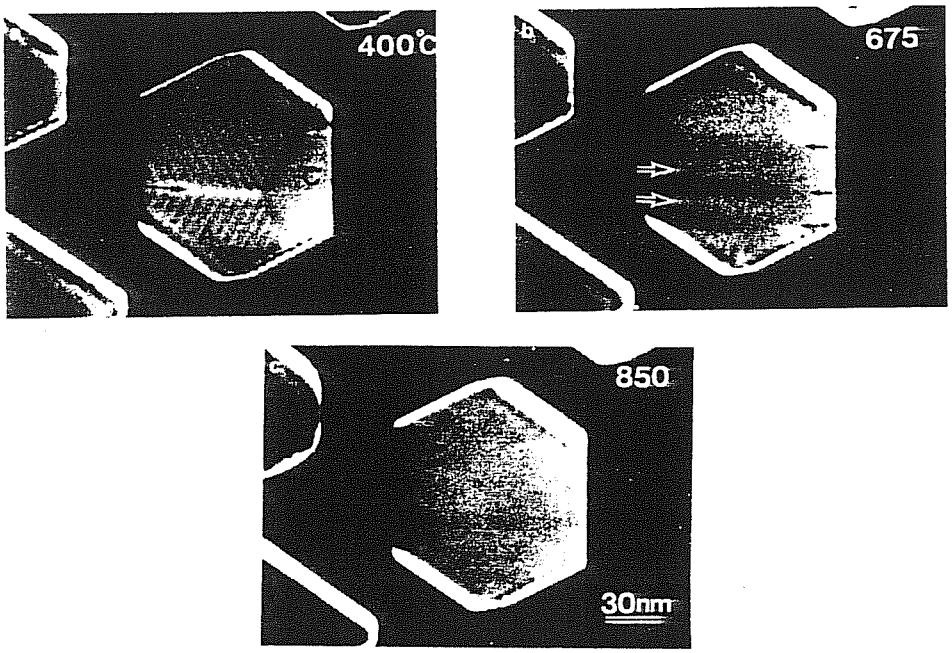

Figure 3.1:
Change of the surface structure image at high temperature. It is well evident the domain separation [2], with the fringes parallel to one of the $[11\bar{2}]$ direction. It can be noticed the change of the fringe orientation and the contrast.

the surface structure change: with increasing temperature the unidirectional shrinkage of the surface layer transforms gradually from anisotropic to isotropic at high temperatures. Moreover the amount of shrinkage seems to reduce. At about 1000 K the reconstruction disappears. This phase transition was also noticed by Melle and Menzel [33] in their RHEED study.

The most important evidence given by TEM is, besides the domain structure, that the fringes are not simple interference fringes due to the shrunk surface and the underlying lattice. The observation suggests the

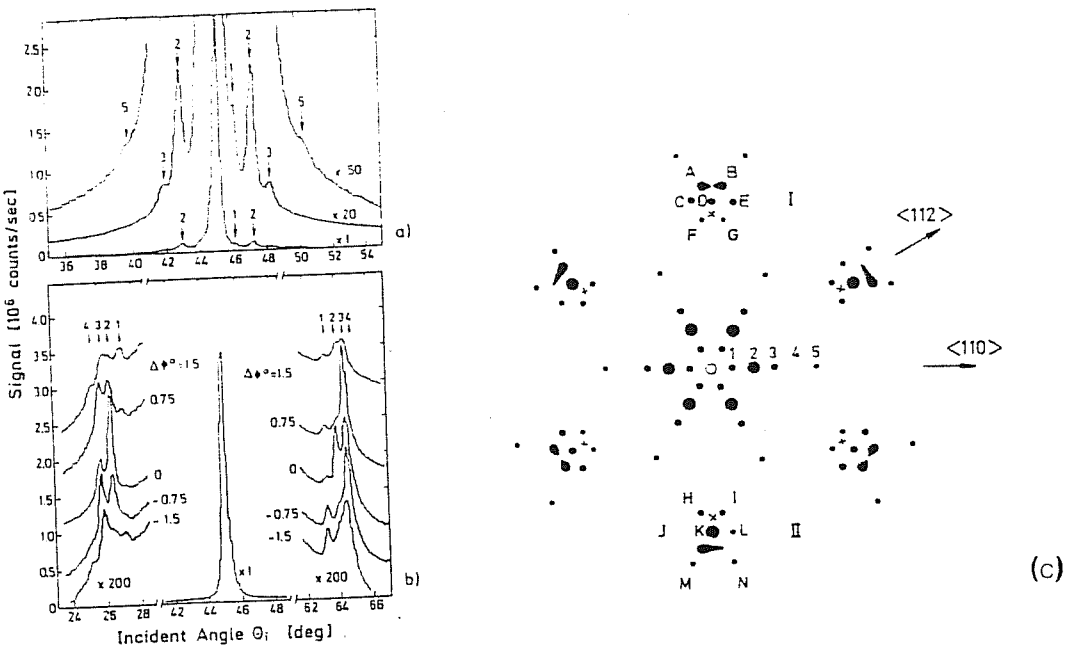

Figure 3.2:
He-Diffraction scans from the Au(111) surface. The crystal temperature was 300 K.
(a) Along $[1\bar{1}0]$ at $k_i = 3.90$ Å^{-1} ($E = 7.95$ meV);
(b) along $[11\bar{2}]$ at $k_i = 5.64$ Å^{-1} ($E = 16.6$ meV).
(c) Schematic representation of full diffraction pattern. The patterns in the $[11\bar{2}]$ have been shifted towards the center, but otherwise the relative positions are to scale. The crosses indicate the diffraction peaks locations expected for the unreconstructed surface. The central diffraction peaks D and K are shifted outwards by $\Delta G = 0.054$ Å from the expected location $G = 2.515$Å.

existence of some definite regions with structure strains like those of misfit dislocations, where the whole contraction should be concentrated. Such local displacements (strains) give rise to diffraction contrast in the bright or in the dark field electron microscopy image.

More recent highly resolved TED experiments by Takayanagi and Yagi [54] suggest that the shrinkage along $[1\bar{1}0]$ is not uniform, but localized in two very narrow transition regions, where the stacking changes abruptly from ABC (fcc structure) to ABA (hcp structure) per unit superlattice cell, the transition region containing 0.5 atom each.

The non-uniformity of the contraction along $[1\bar{1}0]$ direction has been confirmed by He-atom diffraction by Harten et al. [55] (Fig. 3.2), even if the above defined transition regions seem less narrow than those observed by TED. Their estimated half-width is, in fact, about 11.8 Å.

Recent experimental studies by Profile Imaging [38] have confirmed the

superstructure ($p \times \sqrt{3}$), with p $\simeq$ 21, slightly smaller than the precedent superstructures observed. The contraction along the $[1\bar{1}0]$ direction is seen both when the surface is seen in the Profile Image along the direction perpendicular $[11\bar{2}]$ and along the same $[1\bar{1}0]$ direction.

Anyhow, in contrast to these observations, Marks, Heine and Smith [56,57] have reported electron microscopy studies which reveal an expansion of about 5% both normal to and within the surface normal.

3.1.2 Models for Au(111) surface reconstruction

The first complete interpretation of the LEED diffraction pattern has been given by Van Hove et al. [34]: three 120^0 rotated domains, each domain consisting of rectangular $22 \times \sqrt{3}$ cells. They notice that a model consisting of 4.55% uniaxially contracted hexagonal top layer satisfies the observed diffraction pattern, the contraction direction being, as already said, a $[1\bar{1}0]$ direction.

Van Hove et al. [34] propose other two kinds of models. One is a domain structure model involving alternate stripes 11 atoms wide of different bulk termination. An interesting possibility is that half the stripes have the normal fcc termination, while in the other stripes an hcp termination occurs through slippage of the topmost layer to different hollow sites of the second layer. For this model to be stable the two types of termination should have only a small difference in surface energies.

Another possibility, according to Van Hove et al., is based on the concept of charge density wave. In fact, in general, some surface reconstructions have been suggested to be caused by charge density waves in which the conduction electron density has periodic fluctuations with a wavelength a few times the lattice constant, inducing a static wavelike deviation of the atomic equilibrium position with that same wavelength. For the Au(111) surface reconstruction, in particular, a possible model consists of charge density waves with an unusually long wavelength of about 22 lattice constants. Such possibility, however, was later ruled out by He-diffraction and electron microscopy experiments.

Takayanagi et Yagi [54], to interpret their TED experiments, suggest a refinement of the first Van Hove model, with a non-uniform shrinking along x-direction, but localized in transition regions where the stacking changes from fcc to hcp.

We must observe that only some phenomenological approaches to explain gold surface reconstructions have had success, as it will be clear after; in fact to make a theory at the "ab initio" microscopic level is a very difficult task.

Heine and Marks [58] have described a possible microscopic mechanism at the origin of contraction and expansion, observed in Au(111) surfaces by Marks, Heine and Smith [56,57]. It could explain, in general, all noble-metal surface reconstructions. They observe that in the bulk noble metals Cu, Ag, Au there is an opposition between two types of forces. The first is a pairwise repulsion between the atoms due to the full d shells, the second is a multi-atom electron gas attraction due to the sp electrons and $sp-d$ hybridization. They believe that it is the competition between these two kinds of forces, that causes the complex behaviour of noble metals surfaces, especially gold.

In this paper by Heine and Marks [58], perhaps the key result is that they can reconcile apparently conflicting experimental reports of both expansion and contraction, like observed in Au(111), without any difficulty, because the final result is strongly dependent upon the local geometry of the surface. In fact, the geometry of the samples in these experiments, in which the expansions were observed [56,57], was not that of a large, flat surface, but instead, that of a somewhat rough surface with many short surface rafts. These arguments, however, are rather qualitative and do not allow quantitative predictions to be made.

3.1.3 Models for Au(111) surface reconstruction with solitons

Since some models have been proposed to explain the non-uniform shrinking along the $[1\bar{1}0]$ direction, which are based on the theory of solitons [59], we recall very briefly how, from the Frenkel-Kontorova model [60] in the solution of Frank and Van der Merwe [61], the concept of soliton and the mathematical expression which describes it, are introduced. The Hamiltonian of Frenkel-Kontorova model is the following:

$$H = \sum_n (x_{n+1} - x_n - a_o)^2 + V(1 - \cos\frac{2\pi}{b}x_n). \qquad (3.1)$$

It describes at $T = 0$ an unidimensional array of atoms connected with

harmonic springs, which interact with a periodic potential of period b. a_o is the lattice constant which, in general, would be incommensurate with b.

Incommensurate structures generally show up in systems with competing periodicities. Rare gas monolayers adsorbed on graphite constitute a two-dimensional realization of this situation.

Another example is given by a reconstructed surface. A reconstructed surface, in fact, can be formed from the regular surface, by applying, for instance, a periodic lattice distortion. The two periodicities are evidently that of the regular surface and that of the distortion.

The ground state of the 1D-model now described was found in 1949 by Frank and Van der Merwe [61], with the extra assumption that the discrete index n can be treated as a continuous variable. Introducing the phase ϕ_n by the equation

$$x_n = nb + \frac{b}{2\pi}\phi_n \tag{3.2}$$

and transforming to the continuum limit

$$\phi_n - \phi_{n-1} = \frac{d\phi}{dn}, \tag{3.3}$$

the Hamiltonian becomes

$$H = \int \left[\frac{1}{2} \left(\frac{d\phi}{dn} - \delta \right)^2 + V(1 - \cos p\phi) \right] dn; \tag{3.4}$$

$p = 1$ and $\delta = \frac{2\pi}{b}(a_o - b)$ is the natural misfit between the two lattices.

With $p > 1$, H describes the transition to a commensurate phase of order p. The phase is the shift of the atoms relative to the potential minima. The phase $\phi(n) = 0$ is the commensurate phase and the imperturbed incommensurate phase is given by the straight line $\phi = \delta n$.

The ground state, which minimizes the Hamiltonian is found among the solutions of the 1D sine-Gordon equation:

$$\frac{d^2\phi}{dn^2} = pV \sin p\phi. \tag{3.5}$$

One of the solution of this equation is just the soliton

$$\phi(n) = \frac{4}{p}\arctan(\exp(p\sqrt{V}n)). \tag{3.6}$$

The solution describes a wall, centered at $n = 0$, which separate two commensurate regions, one with $\phi = 0$, the other with $\phi = \frac{2\pi}{p}$. The wall represents an extra atom which has been added to the chain within a region given by the soliton width $l_0 = \frac{1}{p\sqrt{V}}$.

In general the solutions are regularly spaced solitons, a soliton lattice (Fig. 3.3)

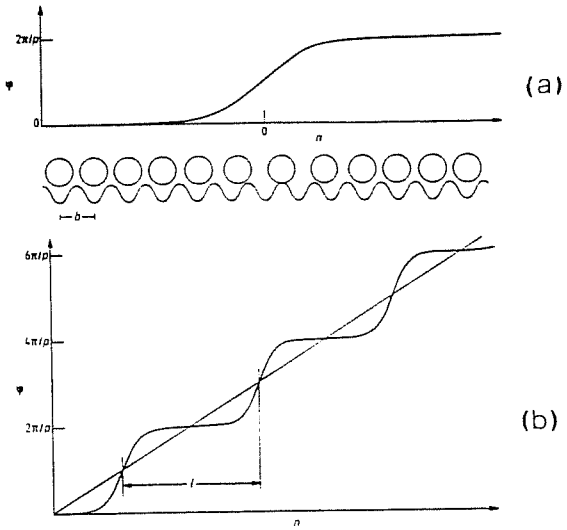

Figure 3.3:
(a) Single-soliton solution obtained by Frank and Van der Merwe. The soliton is a domain wall between two commensurate regions.
(b) Regular soliton lattice solution to the sine-Gordon equation. The straight line corresponds to an imperturbed incommensurate structure.

The soliton lattice is a compromise between the "umklapp" term cos pϕ and the elastic energy which favours $\phi = \delta n$. The concept of walls, now introduced, plays a very central role in all existing theories of commensurate-incommensurate transitions [59].

Introduced very briefly the concept of solitons, we can come back to review all models which use this concept to explain the Au(111) surface reconstruction.

Harten et al. [55] provide support for the model proposed by Takayanagi and Yagi [54], for whom the shrinking along $[1\bar{1}0]$ direction is not uniformly distributed.

The essential feature of their model is a division of the surface in fcc (C site) and hcp (A site) domains. It must be observed that in the case of Au(111) surface the C site should be favoured, if a continuation of the bulk structure occurs. But following the suggestion by Heine and Marks [58], a redistribution of *sp* electrons in the surface may favour a reduction of the interatomic separation from the bulk value.

The competition between occupying the C sites and reducing the mean interatomic separation in the surface layer, is resolved by accommodating both A and C sites, thus reducing the mean interatomic separation in the surface layer through the creation of local defects or, in this case, solitons.

In particular, in the model by Harten et al. [55], within fcc and hcp regions the atoms are at positions defined by bulk lattice spacing, i.e., in registry with the second layer. The transition between C and A regions is described by a gradual x-dependent shift (where x runs along $[1\bar{1}0]$), given by the soliton expression

$$f(x) = \frac{2}{\pi} \arctan\left(\exp\left(\frac{x}{\Delta S}\right)\right) \tag{3.7}$$

where $2\Delta S$ is the half-width of a soliton centered at the boundary between A and C regions. In this model the transition region is larger than the narrow transition region proposed by Takayanagi and Yagi [54].

In such a region, where the soliton causes a very gradual shift from the A to the C stacking, the atoms are raised up in the z-direction by a x-dependent amount $H(x)$ modeled by a Gaussian with height H and half width ΔS centered at the solitons. There is an undulation in the y direction ($[11\bar{2}]$), whose periodicity is the double of the periodicity of the corrugation in the z-direction (see Fig. 3.4). In their model it is also allowed that the C and the A regions have a different relative size R (which removes the otherwise twofold rotation symmetry of the surface layer).

To test their model, they have performed hard-wall eikonal [62] calculations, to compare the calculated diffraction peaks with those obtained by their High-Resolution-He-Atom-Diffraction experiments. The agreement is very good for the choice of parameters $R = 0.7$, $\Delta S = 5.9$ Å, $H = 0.15$ Å, and assuming an additional uniform contraction of 2% extending to subsurface layers.

The diffraction pattern remains unchanged when the temperature is varied between 120 K and 700 K. For this reason Harten et al. [55] conclude

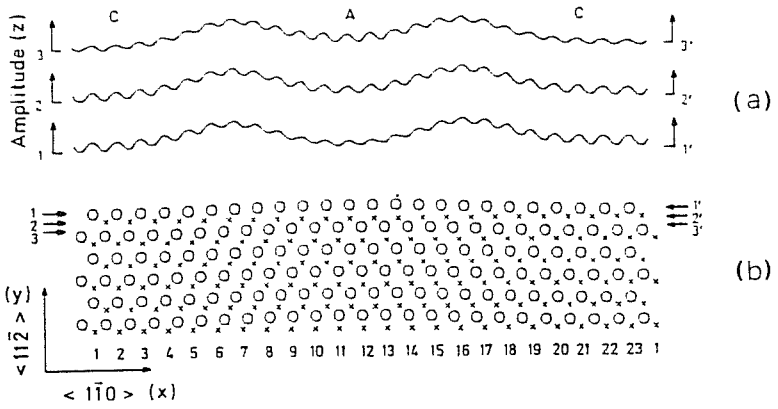

Figure 3.4:
(a) Hard-wall corrugation functions at three points of the unit cell.
(b) Crosses represent the second-layer and circles the surface-layer atoms.

that the interaction between solitons is probably so strong that it overrides the entropy contribution to the free energy, which might otherwise cause temperature-driven transitions between phases of different soliton density or disordering of the walls.

To resume the physical situation, we can say that the soliton superlattice may be indicative of the existence at the surface of two competing potential contributions of different periodicities. In the top layer, due to a change in electronic structure relative to the bulk, as it has been hypothesized [58], it is favoured a contraction to a smaller lattice constant, but the competing interaction with the bulk compels the surface atoms to stay in their normal bulk positions. Then, this situation may well be a physical realization of the Frenkel-Kontorova model of competing interactions [60]. The ground state of this model is a lattice of regularly spaced soliton type walls, which separate commensurate regions. So, the soliton superlattice can be regarded as a compromise between a fully incommensurate, and in this case compressed, structure in which the surface layer forces dominate, and an unreconstructed surface with bulk forces dominating.

In a following model [63] the reconstruction of the Au(111) surface has been interpreted in terms of a new type of misfit dislocations, namely double-sine-Gordon-type-dislocations (DSG). It is just an improvement of the sine-Gordon (SG) solitons by Harten et al. [55], since the simple SG model cannot justify a priory the unequal areas of the regions with stacking

A (hcp-like) and C (fcc-like).

In the case of the fcc surfaces the topology of the underlying substrate potential is that the minimum energy path for the transition from one site type (fcc) to the other (hcp) is effected across the shared bridge sites. Potential energy minima are located at the A and C sites, while a saddle point is found at the bridge site. The resulting zigzag shape of the underlying potential can be described by a one-dimensional potential. The non-degeneracy of the A and C site energy minima suggest a DSG-like substrate potential, while it cannot be taken into account at all with a simple SG chain.

The corresponding Frenkel-Kontorova Hamiltonian has the form

$$H = \frac{\mu}{2}\sum_{i=0}^{N}[x_{i+1}-x_i-(a-b)]^2+\frac{8V}{(4+R)^2}\sum_{i=0}^{N}\left\{\left[1-\cos\left(\frac{2\pi x_i}{b}\right)\right]+\left[1-\cos\left(\frac{4\pi x_i}{b}\right)\right]\right\}. \tag{3.8}$$

V is the peak-to-peak amplitude, b is the potential periodicity, a the equilibrium interparticle spacing, x_i is the displacement of the ith particle from the bottom of the ith C well, μ the elastic constant of the surface layer, N the number of atoms in the chain; the range of the parameter R ($0.0 \leq R \leq 4.0$) makes the potential at the C site take the minimum zero-value, and at the A site vary from zero at $R = 0$ (SG case) to V at $R = 4.0$.

The continuum limit of the motion-equation has stable solution of the form

$$\tan(\pi u) = \left(1+\frac{4}{R}\right)^{1/2} csch\left(\frac{4\pi n}{(R+4)^{1/2}l_o}\right), \tag{3.9}$$

with $u = x/b$ and $l_o^2 = \frac{\mu b^2}{2V}$. The solution can be viewed as a configuration of two bound π solitons, each with an effective length of $\frac{l_o}{2}$ and center to center separation $L \simeq \frac{l_0}{4\pi} ln\frac{1}{R}$ (in the limit $R \ll 1.0$) (Fig. 3.5). El-Batanouny et al. [63] have fitted the He-Diffraction data [55] to the DSG (with the mismatch 22/23, $l_o \simeq 8b$, R $\simeq 0.01$).

First of all, to determine the equilibrium metastable configurations of such a DSG chain they have used molecular dynamics [64]. Subsequently, to construct the $(23 \times \sqrt{3})$ unit cell of the reconstructed Au(111) surface, they have used the equilibrium positions of the particles, constituting the DSG soliton, as the x-coordinate (along $[1\bar{1}0]$) of the atomic centers, while the

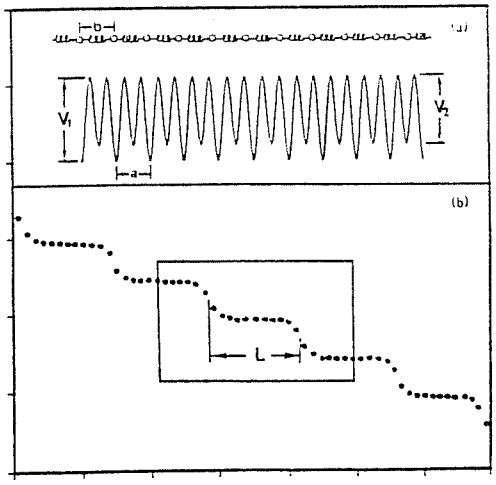

Figure 3.5:
(a) A schematic diagram of a DSG-like Frenkel-Kontorova model where $V_1 = W$ and $V_2 = (1 - R)W$.
(b) Profile of a DSG soliton chain showing the displacement u_n of the nth C-type well. Inset: Individual DSG soliton [63].

y-coordinates (along $[11\bar{2}]$) and z-coordinates (along [111]) were determined from a hard-sphere stacking model with the interatomic separation of the bulk. A typical planar view of the atomic arrangement is shown in Fig. 3.6 and it is very similar to that obtained by Harten et al. [55].

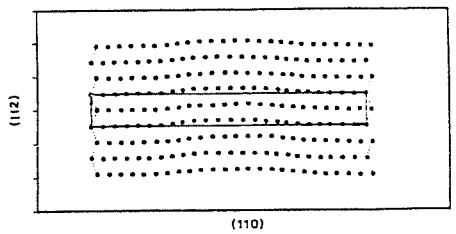

Figure 3.6:
Planar view of the atomic arrangement involving DSG soliton. Notice the atomic displacements in the $[1\bar{1}0]$ direction and the zig-zag stacking of solitons along the $[11\bar{2}]$ direction.

The soliton stacking pattern in the $[11\bar{2}]$ direction results in a zigzag like pattern. Similarly to the previous authors, they superimposed a Gaussian charge distribution on the atomic center positions in order to reproduce the surface corrugation, and the atomic beam diffraction intensity were

computed, using the hard-wall and eikonal approximation [62]. The results are similar to that obtained by Harten (Fig. 3.4, [55]).

Another phenomenological model, which tries to explain the non-uniform shrinking in the reconstruction direction, due to the presence of solitons, is that by Okwamoto and Bennemann [65], who have applied a similar model to the Au(100) reconstruction [41]. They improve a precedent model by Kanamori and Kawakami [66], who have studied the reconstruction of Au(111) surface, by applying a two-dimensional elastic model to the surface layers of the atoms. In this precedent model, it is assumed that the top-layer tends to contract isotropically and the minima of the substrate potential form a triangular lattice commensurate with the bulk (111) layer structure.

Okwamoto and Bennemann, taking into account the experimental observations of the domain wall structure, modify the Kanamori-Kawakami theory. Taking into account also a theory used for physisorbed gas monolayers [42], they treat the surface layer of atoms as a two-dimensional isotropic continuum, with structure induced by the potential of the underlying substrate lattice, considered as a rigid substrate, with the structure of a perfect bulk. They also do the following hypotheses:

(a) the minima of the substrate potential are at positions of fcc and hcp termination, i.e. they form an honeycomb lattice;

(b) the structure with hcp termination is degenerate with the one having fcc structure;

(c) the top layer contracts isotropically, when the top layer lattice becomes uniformly incommensurate in two directions with respect to the substrate lattice. This is called the "unstrained state" of the top layer.

Obviously there are two competing lengths: the lattice constant "c" of the unstrained state of the top layer and the lattice constant "a" of the triangular lattice of the second layer.

With these hypotheses, and keeping from the theory of the physisorbed gas-monolayers [42], in the continuum approximation, the expression for the strain energy of the top-layer, which contains μ (the shear-modulus) and K (the bulk-modulus), they can obtain an expression for the total energy. Variation of the total energy with respect to $\vec{u}$, the atomic displacements, gives an equation from which it is possible to get the equilibrium structure of the top layer at zero-temperature. They calculate the energy for three types of domain-walls (extremely narrow with large contractions (10%)),

in three slightly incommensurate lattice structures:

(a) unidirectionally contracted in x-direction;

(b) unidirectionally contracted in y-direction;

(c) isotropically contracted ("unstrained state", triangular lattice).

For all the three cases, it has been calculated the critical value of c_c, below which the incommensurate structure becomes stable relative to the commensurate structure.

On the basis of their results for the three cases examined, and taking into account qualitatively the effects of the difference of the substrate potential energies, referring to fcc and hcp-positions (called "Δ"), they conclude that the unidirectional contraction occurs in the $[1\bar{1}0]$ direction at the Au(111) surface, since the calculations show that $c_c^x > c_c^y$ for $K/\mu < 10$. Without taking into account the effects of Δ, instead, the favoured structure becomes the isotropic one. Furthermore, they speculate from the expression, which gives the wall-width, that the ratio K/μ is larger than 2.

Within their scheme, including quantitatively the effects of Δ, it could be possible to study the phase transition from the unidirectionally contracted state to the isotropically contracted one [67], observed by TEM [2].

3.2 Simulation studies of Au(111) surface reconstruction in the glue model

3.2.1 Au(111) surface reconstruction at T=0

After the review of the complex experimental and theoretical situation about the Au(111) surface, we describe in this Section our investigation on structure and energetics of the Au(111) surface using the glue Hamiltonian. As shown in the previous Chapter, this model successfully predicts the occurrence of reconstruction on Au(100) and Au(110). In both cases, the reconstruction appears to be driven by the tendency to form close-packed, (111)-like topmost layers. On Au(100), this is accomplished by the formation of quasi-triangular overlayer, while Au(110) facets into a sequence of tiny (111) microfacets. Au(111) is already well-packed, and in fact it does not reconstruct on Ir and Pt, which both exhibit (100) and (110) reconstruction very similar to Au. However, as we have seen in the previous

Section, in Au the tendency of surface atoms to pack seems to be so strong so as to induce even a (111) reconstruction by in-plane contraction. As it turns out, this tendency is even stronger in the glue model, giving rise to a (111) reconstructed surface whose in-plane density is larger than that given by experiments. The qualitative aspects of structure and energetics appear however to be in good agreement with experimental data.

For this study, we have investigated by the usual MD strategy both surface energy and shape of a series of 10-layers slabs, with free boundary conditions in the [111] direction, and periodic boundary conditions in the in-plane directions $[1\bar{1}0]$ (henceforth x-direction) and $[11\bar{2}]$ (henceforth y-direction).

The size of the periodically repeated MD box has been taken $M \times L\sqrt{3}$ (in units of $d = a/\sqrt{2}$, where $a = 4.07$ Å is the $T = 0$ lattice parameter). M and $L\sqrt{3}$ are the lengths in x and y directions respectively.

The number of atoms in a general layer is $2LM$, while that in the outermost surface layers is permitted to increase to $2L(M+1)$, by requiring each atomic row in the $[1\bar{1}0]$ direction, which is the reconstruction direction, as suggested from the experiments, to compress so as to accommodate $M+1$ atoms over M. Since the number of particles must be constant in MD, these extra atoms must be already present in the initial state, which has been constructed as an uniformly compressed triangular lattice. L does not play any role in the reconstruction (the reconstructed unit cell has $L = 1$), so that we have fixed it to be $L = 2$ in most calculations for computational convenience [1].

The relaxed, but unreconstructed Au(111) (calculated with a very small cell $3 \times 2\sqrt{3}$ where no extra atoms were added) is found to have a surface energy $\sigma_1 = 96.6$ meV/Å^2. The slabs are relaxed to a minimum-energy configuration either by a direct quenching or annealing/quenching procedure, as discussed in Section 1.4. The surface energy σ is defined as usual as in Eq.(2.1). It can be seen that the increase of the density by contraction in the x-direction leads to a lowering of this value.

The problem has been to find the size M of the cell in $[1\bar{1}0]$ direction, which corresponds to the optimal density $(M+1)/M$ to the minimum σ.

The results are summarized in Table 3.1, where also multilayer relaxations are reported. It can be seen that σ decreases to the minimum value

[1] A MD box with $L = 1$ can not be used, since it would imply interaction of each

Structure	σ(meV/Å^2)	Δd_{12} (%)	Δd_{23} (%)	Δd_{34} (%)
$(4\times\sqrt{3})$	114.4	+1.4	+2.4	-0.3
$(5\times\sqrt{3})$	99.4	-0.5	+2.5	-0.3
$(6\times\sqrt{3})$	93.2	-1.8	+2.6	-0.3
$(7\times\sqrt{3})$	90.4	-2.6	+2.6	-0.3
$(8\times\sqrt{3})$	89.1	-3.2	+2.6	-0.3
$(9\times\sqrt{3})$	88.5	-3.7	+2.6	-0.3
$(10\times\sqrt{3})$	88.3	-4.1	+2.6	-0.3
$(11\times\sqrt{3})$	88.1	-4.4	+2.6	-0.3
$(12\times\sqrt{3})$	88.3	-4.6	+2.6	-0.3
$(13\times\sqrt{3})$	88.4	-4.8	+2.6	-0.3
$(15\times\sqrt{3})$	88.8	-5.1	+2.6	-0.3
$(18\times\sqrt{3})$	89.3	-5.4	+2.5	-0.3
$(23\times\sqrt{3})$	90.2	-5.8	+2.5	-0.3
$(33\times\sqrt{3})$	91.4	-6.1	+2.4	-0.3
$(50\times\sqrt{3})$	92.5	-6.4	+2.4	-0.3
non-reconstructed, relaxed	96.6	-7.9	+1.2	-0.1
non-reconstructed, ideal	105.1	0	0	0

Table 3.1:
Surface energies and variations of the average interplanar distances $\Delta d_{i,i+1} = (d_{i,i+1} - d_0)/d_0$, where $d_o = 2.35$ Å is the bulk (111) spacing, for several (111) reconstruction geometries.

$\sigma_o = 88.18$ meV/Å^2 for the optimal choice $M = 11$, which is smaller than that expected from experimental data $M = 22 - 23$. For this best case, we have also checked that the results are independent from the choice of L, by repeating the calculations for $L = 3, 5, 6$. Increasing M, in the limit $M \to \infty$, the density and $\sigma(M)$ are expected to recover the unreconstructed case.

It is seen that the average first-second layer distance d_{12} exhibits a contraction. This is another mechanism by which surface atoms can gain coordination in our model. The contraction decreases when M is decreased to compensate for the increment of in-plane packing. For the optimal structure $(11 \times \sqrt{3})$, the average first-second layer spacing is contracted by 4.4% (0.10 Å) with respect to the bulk value, while the second-third layer spacing is increased by 2.6% (0.06 Å).

From the examination of the values of σ, the surface energy minimum at $M = 11$ is very asymmetric and shallow, only if M is increased above 11. For example is still as low as 90.2 meV/Å^2 when M is as high as 23. This means that grand-canonical fluctuations (allowed in presence of source terms, which could be present in the form of steps, etc.) might tend to increase the average value at finite temperatures. In turn, this would bring the theoretical result closer to the experimental value $M \simeq 23$.

The behaviour of $\sigma(M)$ is reproduced reasonably well by a second order expansion in powers of $1/M$:

$$\sigma(M) \simeq a + \frac{b}{M} + \frac{c}{M^2} \tag{3.10}$$

with $b \simeq 200$ meV/Å^2 and $c \simeq 1200$ meV/Å^2. b can be regarded as the chemical potential of the reconstruction stripes.

It should be noted that an exact energy minimization of reconstructed Au(111) turned out to be a difficult optimization problem. In fact, for a given M there is a very large number of local energy minima, which are very close to each other; typically they are all within 0.1 meV/Å^2 in surface energy, corresponding to $\simeq 10$ K per surface atom. Structurally, these minima differ for tiny registry shifts of the topmost layer relative to the second, along the reconstruction direction $[1\bar{1}0]$. A direct quenching procedure brings the surface into the local minimum corresponding to the

particle with itself through periodic boundary conditions.

registry nearest to that of the initial configuration. A thermal annealing procedure followed by quenching, on the other hand, is not able to select the global minimum due to the exceedingly small energy differences between minima, and brings the surface into any of the minima essentially at random.

The small energetic differences make, however a precise determination of the global minimum somewhat academic and almost meaningless, since, for example, already at 100 K the thermal fluctuations overwhelm those due to this sort of "spin-glass" problem. For this reason, we have attempted an exhaustive search by using a direct quenching and starting from 36 different initial registries, only in the case $M = 11$. The values for σ, that we have obtained range from 88.14 to 88.22 meV/Å^2. The values, reported in Table 3.1, correspond in each case to a single, arbitrary initial configuration, and therefore they probably all contain an intrinsic error of less than 0.1 meV/Å^2 with respect to the true surface energy minimum.

All these $T = 0$ structures present a typical division in narrow domains in which the epitaxy is alternatively of the type fcc ($ABCABC$ stacking) or hcp ($ABAB$ stacking). These domains are separated by wide smooth transition regions, in which the atoms of the topmost layer are in bridge with those of the second layer (Fig. 3.7, Fig. 3.8 and Fig. 3.9).

An example of the registry shift discussed above can be seen by comparing the two configurations in Fig. 3.7 and in Fig. 3.8. While they look almost identical, there are small differences in the atomic positions. In that of Fig. 3.7 with $\sigma = 88.14$ meV/Å^2, the lowest value obtained, the centers of the regions fcc and hcp and of the transition areas pass just in the middle of the atoms. In that of Fig. 3.8, which has $\sigma = 88.18$ meV/Å^2, the centers of the regions fcc, hcp and of the transition areas, instead, do not pass through the centers of the atoms, but among them.

What disagrees with some experimental results [54,55] is the fact that the shrinking in the x-direction for each $[1\bar{1}0]$ row is nearly uniformly distributed along the whole row, instead of being localized in narrow soliton-type regions, separating wide fcc and hcp regions, as Harten et al. suggest [55] (see Section 3.1.2).

The absence of solitons has been confirmed by the calculation of the phase ϕ, that, for each row can be defined, following the suggestion of Frank and Van der Merwe [61] and similarly to the Au(100) case, as

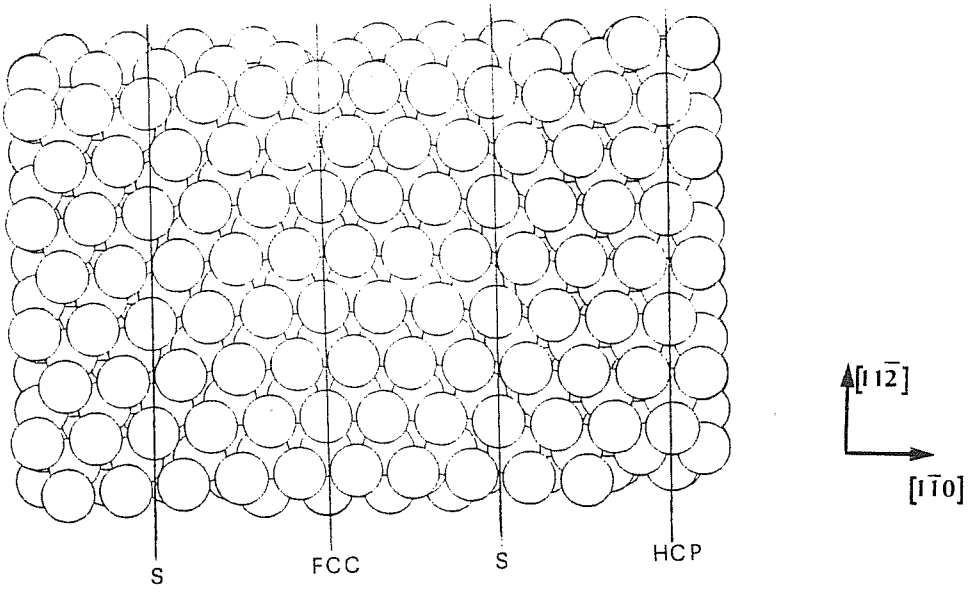

Figure 3.7:
Top view of the $(11\times\sqrt{3})$ configuration with σ = 88.14 meV/Å^2. 4 MD boxes have been drawn along $[11\bar{2}]$ for visual convenience. The vertical lines indicate the centers of regions fcc, hcp and the transition regions in which the atoms in the topmost layer are in bridge with those of the second layer.

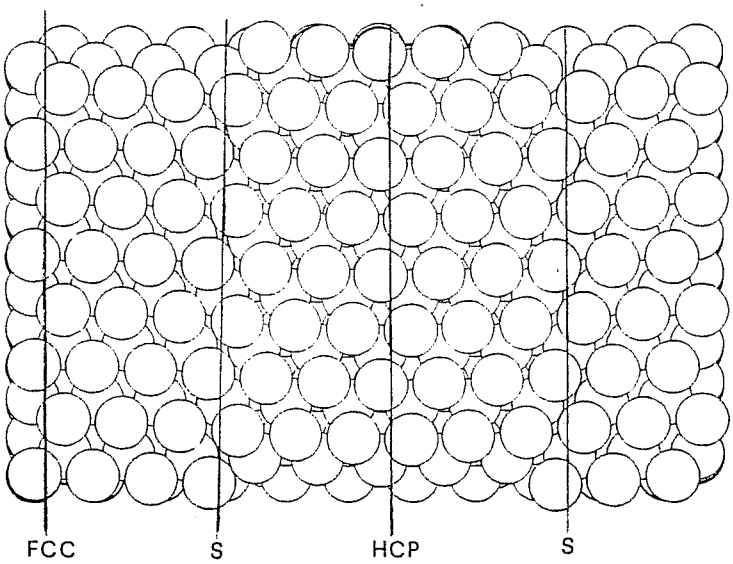

Figure 3.8:
Top view of the $(11\times\sqrt{3})$ configuration with σ = 88.18 meV/Å^2. 4 MD boxes have been drawn along $[11\bar{2}]$ for visual convenienence. The vertical lines indicate the centers of regions fcc, hcp and the transition regions in which the atoms in the topmost layer are in bridge with those of the second layer.

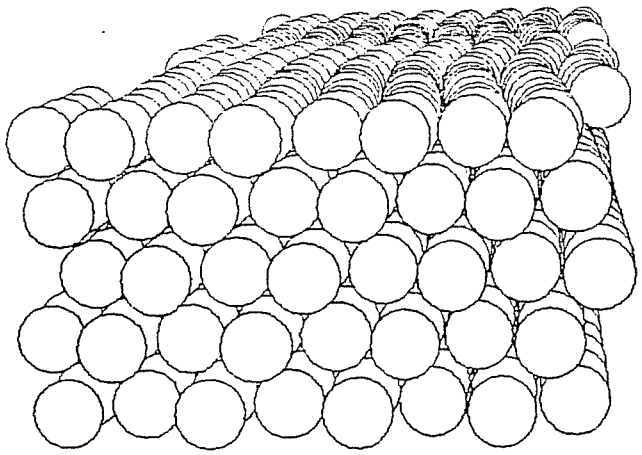

Figure 3.9:
Side view of (111) slab in the $[11\bar{2}]$ direction. Only the top 5 layers are shown. Note the undulation in $[11\bar{2}]$ direction.

$$\phi(x_n) = \frac{2\pi}{d}(x_n - nd + c) \tag{3.11}$$

where n is an index running from 1 to 12 (number of atoms in a top row for the optimal cell of M =11), x_n is the final coordinate of the n atom of the quenched sample; nd should be the position of the n-atom, in absence of reconstruction; c is a constant, which is taken equal for all the rows.

Instead of finding for $\phi(x_n)$ the expected arctg-behaviour [59], we have got altogether an almost linear trend (Fig. 3.10), which indicates that the strain in the $[1\bar{1}0]$ direction is not concentrated in small soliton-like portions of the row, but rather distributed all over the row.

Another characteristic of the morphology of the structure of Au(111) at $T = 0$ is the "undulation" in y-direction on each single top layer atomic row, with maxima and minima corresponding to atoms in fcc and hcp positions respectively. The total amplitude of this undulation (that is the $[11\bar{2}]$ distance between the atoms in fcc and hcp positions) is about 1.0 Å.

A corresponding small vertical undulation is also present, with the maximum z-coordinate reached by the atoms in bridge positions and the minimum by those in the centers of regions hcp and fcc; so the periodicity of this undulation is half of that in the xy plane. The entity of this corrugation is very small ($\simeq$ 0.12 Å), but comparable with that proposed by Harten

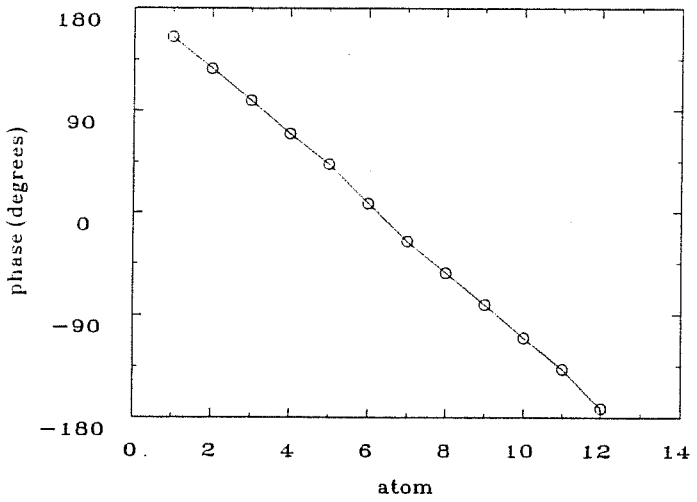

Figure 3.10:
The phase ϕ (Eq. 3.11) for the atoms on a $[1\bar{1}0]$ row, versus the atom number. Note the almost linear trend.

et al. (0.07 Å) [55]. Finally, note that the extension of the fcc areas is nearly equal to that of the hcp areas in our scheme, while experimentally the fcc areas seem to be slightly larger [55]. This is to be expected, since the glue model defined in terms of first neighbour interactions is not able to differentiate energetically the fcc and hcp structures.

3.2.2 Au(111) surface reconstruction with increasing temperature

Within the same MD scheme and the glue model, we have undertaken a study of the temperature dependence. In particular, we have been interested in studying the high temperature behaviour. Experimentally, as reviewed in Section 3.1, Au(111) exhibits a transition from a configuration in which the shrinkage in the topmost layer is unidirectional along $[1\bar{1}0]$, to a configuration in which the shrinkage becomes isotropic (i.e., shared between $[1\bar{1}0]$, $[01\bar{1}]$ and $[\bar{1}01]$) and a slightly smaller one. Moreover, around 1000 K the reconstruction disappears [2].

First of all, we have followed the simple hypothesis that the lowest energy configuration is $(11\times\sqrt{3})$ also at temperature different from zero. Of course, a more appropriate procedure, which we have not attempted, would have been to calculate and to minimize as a function of the cell length, the surface *free* energy, at each temperature.

Following a simpler way, the only modification which we have done to our MD box to perform runs at finite temperature has consisted of changing for each temperature the lattice parameter, following the bulk thermal expansion, as obtained by a previous simulation of bulk gold by the same model [14]. At each temperature the system has been run for 4500 time steps, of which the first 1500 are required to reach equilibrium and are not considered in subsequent data analysis.

To study better the region of high temperatures, where we could expect large fluctuations of the fcc-hcp domain walls, possibly leading to the disappearance of reconstruction, we have used a big MD box, multiple of the elementary one, as large as $(22\times10\sqrt{3})$. In this case, to reduce the number of particles, we have worked with 5 layers only and, among these, the two bottom ones have been assumed to be rigid in their bulk- like positions to mimic the contact with a seminfinite bulk. In total our system has 2240 particles, of which 1360 are moving and the remaining are kept fixed.

With these big samples we have seen that the reconstruction is still present at temperatures as high as 1400 K, i. e. above the melting temperature, while experimentally it seems to disappear around 1000 K [2]. The fcc and hcp domains are still recognizable and the walls, which separate them, are only slightly disordered, as it can be seen in the series of snapshots reported in Fig. 3.11 and in Fig. 3.12, where the region of very high temperature is showed.

This fact has been confirmed by the analysis of the phases ϕ along the $[1\bar{1}0]$ rows, that show no important variations with temperature, calculated using both instantaneous and averaged coordinates over the MD run. They, in fact, retain their almost linear shape with increasing temperature.

Only above 1400 K we have observed in the snapshots the formation of dislocations and it becomes no longer possible to individuate well the walls which separate fcc and hcp areas.

All this means that the reconstruction has an extremely strong character and that very high temperatures are required to destroy it. In fact, it turns out that reconstructed Au(111) in the glue model is so stable to allow overheating of the system above the bulk melting point in MD simulations. Usually, instead, in two-body systems the surface becomes very disordered, well below T_M, and it acts as a suitable nucleation site for the liquid phase when T_M is approached.

These facts have been confirmed by more careful calculations made by

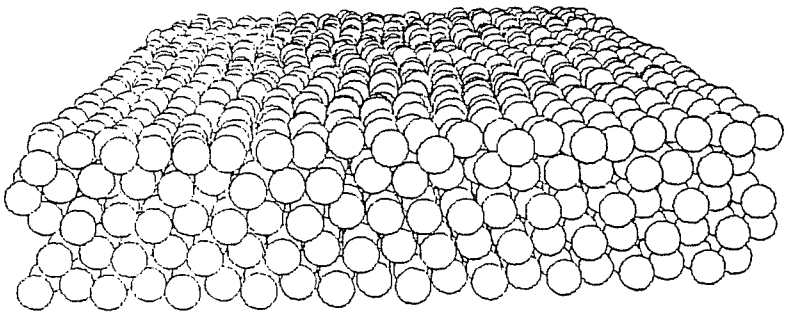

(a)

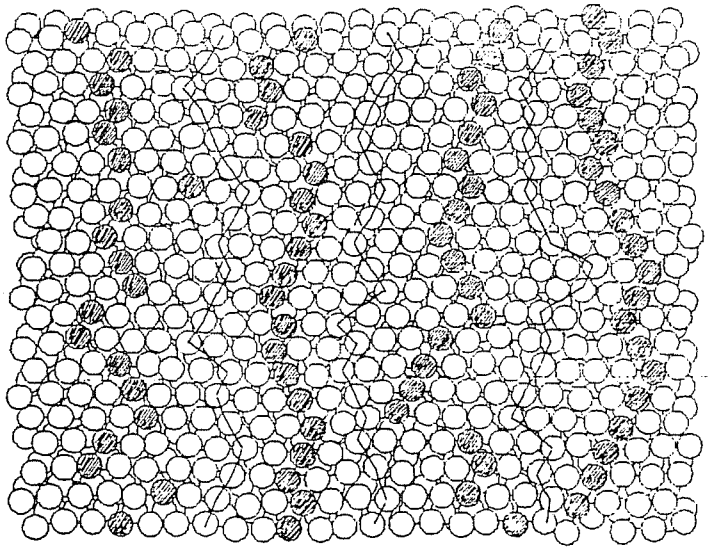

(b)

Figure 3.11:
Snapshots of the Au(111) reconstructed surface at $T = 900K$. A MD box, containing a 2×10 array of $(11 \times \sqrt{3})$ reconstruction unit cells is shown.
(a) Whole sample.
(b) Top view.

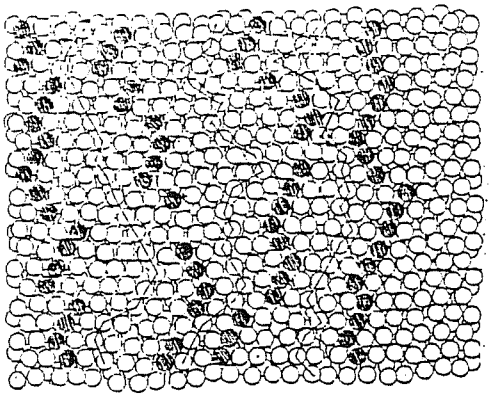

(a)

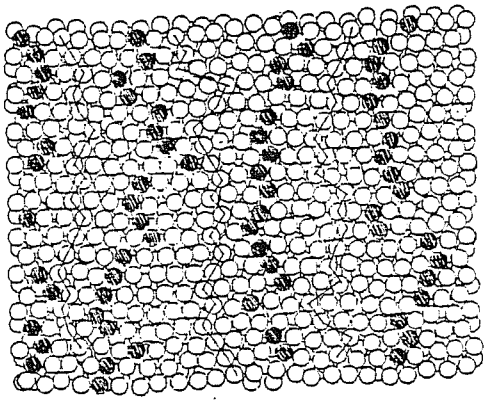

(b)

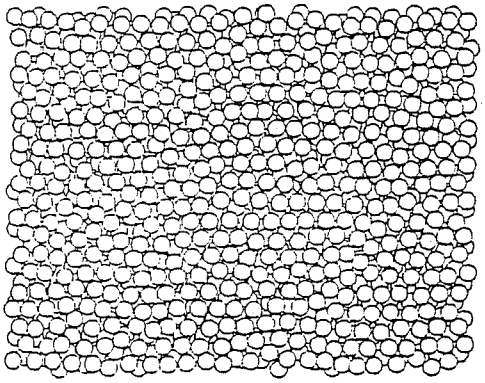

(c)

Figure 3.12:

As Fig. 3.11.
(a) Top view at $T = 1100K$.
(b) Top view at $T = 1300K$.
(c) Top view at $T = 1500K$.

Carnevali, Ercolessi and Tosatti [70] on the surface melting behaviour of the Au(111) surface in the same glue scheme. Their most important conclusion is that the reconstructed Au(111) surface does not show any evidence of surface melting, at least within their equilibration times range ($10^{-10}s - 10^{-9}s$ which, with a time step $\Delta t = 7.14 \times 10^{-15}s$, equal to that used by us, correspond to $10^4 - 10^5$ time steps). Such MD runs are much longer than ours, which are $\simeq 5000$ time steps long. This can explain the fact that they obtain a melting temperature $T_M = 1357 \pm 5$ K, that compares very well with experimental results $T_M = 1336$ K, while in our calculations the system is not yet melted at 1500 K.

So these calculations indicate us that all crystalline states above 1357 K that we have got, studying in temperature the reconstructed Au(111) surface, are in reality not effectively stable equilibrium states, but only *metastable* ones.

This non melting behaviour seems to be an effect of the many body forces. Specifically, the energetics of surface atoms, very poor in a system with two body forces (such as LJ), becomes much better once the many-body forces are included. As a consequence, all entropy related quantities, such as thermal vibration and expansion, and defect concentration, are expected to rise much higher near T_M in a two-body system than in a many-body system. The case of Au(111) is perhaps extreme and surface stability, due to the glue term, is so strong as to prevent microscopic melting, allowing even the surface to be overheated at least in the absence of surface steps.

We have continued the study in temperature, even if by metastable states, monitoring the behaviour of in-plane phase correlations at various temperatures to check a possible variation in their trend before and after the disappearance of reconstruction.

From the theory of commensurate-incommensurate transition [59] we know that the "order parameter" correlation functions take the following forms in the various commensurate and incommensurate phases ($\vec{q}$ is the wave-vector of the phase) at long distances:

(a) commensurate :$\langle S(0)S(\vec{r})\rangle \simeq \cos(\vec{q_o}\cdot\vec{r}+\phi)$, $\vec{q_o}$ commensurate,

(b) incommensurate :$\langle S(0)S(\vec{r})\rangle \simeq \cos(\vec{q}\cdot\vec{r}+\phi)$, $\vec{q}$ incommensurate,

(c) fluid :$\langle S(0)S(\vec{r})\rangle \simeq \exp(-\alpha r)\cos(\vec{q}\cdot\vec{r})$,

(d) floating :$\langle S(0)S(\vec{r})\rangle \simeq r^{-\eta}\cos(\vec{q}\cdot\vec{r}+\phi)$.

It is important to remark that the floating phase with incommensurate wavevector and power-law decay, is believed to exist only in two dimensions, because in two dimensions an incommensurate phase with long-range order cannot exist. Shortly, we can say that for large separation $\vec{r}$ a non-zero constant limit of the correlations indicates long-range order, an exponential decay indicates disorder, and a power-law decay of the correlations is expected for a two-dimensional incommensurate (or floating) phase.

We expected that the reconstruction related ordering have been disappeared over 1400 K, the temperature at which in our precedent study the disorder starts to appear and that this transition (commensurate - disorder) was present also in the behaviour of phase correlations.

We could expect such a behaviour, following the suggestion of what happens for the W(001) surface [71], where the transition from the commensurate (2×2) phase to a disordered one occurs through a sequence of narrow, but well defined intermediate phases, which results, just from the behaviour of surface spatial phase correlations, to be incommensurate.

In the case of Au(111) we have calculated the spatial correlations of the cosine of the phases, defined in the previous Subsection 3.2.1 (Eq. 3.11). The correlation function is defined to be, in this case,

$$C_x(R) = \left\langle \cos\frac{2\pi}{d}x_l \ \cos\frac{2\pi}{d}x_m \right\rangle \tag{3.12}$$

where R is the distance between the two generic l and m atoms. We have calculated it by averaging over a circle or row by row. When we calculate them row by row, we mean that the atoms l and m are on the same row in x direction and the average is done on all atoms on it, whose distance is less than $L_x/2$, where L_x is the length of the MD box along x. When we calculate them on a circle, we mean that the atoms l and m are within a circle of radius $min(L_x/2, L_y/2)$. The same we have done in y-direction, substituting d with $d\sqrt{3}$, the distance between two nearest neighbour atoms in y-direction:

$$C_y(R) = \left\langle \cos\frac{2\pi}{d\sqrt{3}}y_l \ \cos\frac{2\pi}{d\sqrt{3}}y_m \right\rangle . \tag{3.13}$$

We have calculated spatial phase correlations also in y-direction both row by row and on a circle, to study especially the behaviour of the undulation observed in this direction.

For what concerns the phase correlations in x-direction, up to 1400 K, we expected to get, in a graph with $lnC(R)$ in function of $ln(R)$, a straight line with angular coefficient equal to $-1/2$. In fact the coefficient η for the power law decay of correlations $r^{-\eta}\cos(\vec{q}\cdot\vec{r})$ in a floating phase is shown to be $\eta = 2/p^2$ by Schulz [72], with p linked to the number of domains separated by the walls of solitons. In our case $p = 2$ for the presence of the fcc and hcp regions.

Over 1400 K, instead, we expected to get a straight line in a graph with $lnC_i(R)$ $(i = x, y)$ in function of R, that is a power law decay of correlations, being in a completely disordered phase. But the shape of the graphs has not resulted like we expected but rather as a series of slowly decaying rapid oscillations. As we expected, instead, we have seen that the correlations decrease if the distance increases. As an example in Fig. 3.13 and in Fig. 3.14 the trend of x-correlations on a circle at the two temperatures 1000 K and 1500 K has been reported.

We have got the same results, independently by the various sizes of the MD box ($11 \times 2\sqrt{3}$, $22 \times 2\sqrt{3}$, $22 \times 13\sqrt{3}$) used. With the biggest one we have worked with 5 layers and the two bottom ones had fixed particles, while the two smaller boxes had two free surfaces.

An oscillating behaviour has been, in fact, obtained for all kinds of correlations calculated. Having the suspect that the persistent oscillating behaviour was linked to the fact that the walls, which separate fcc and hcp domains, bend very slowly in the intervals of time used initially for the simulation (around 5000 time steps), making a periodical structure to persist, we have followed for longer runs the movement of these walls. We have had the confirm that also in reasonable intervals of time in which we can expect large movements, the walls never cross each other, but remain almost in their positions, keeping the fcc and hcp domains well separated and clearly distinguishable.

To summarize, by the glue model and MD, it has not been possible to study the transition from the uniaxial shrinkage to the isotropic one at around 1000 K and to check the disappearance of the reconstruction, by the trend of phase correlations, which we would expect to show a transition from an incommensurate phase to a disordered one.

We must admit, in fact, that our method has resulted to suffer of various shortcomings. By fixing the shape of the MD box from the beginning,

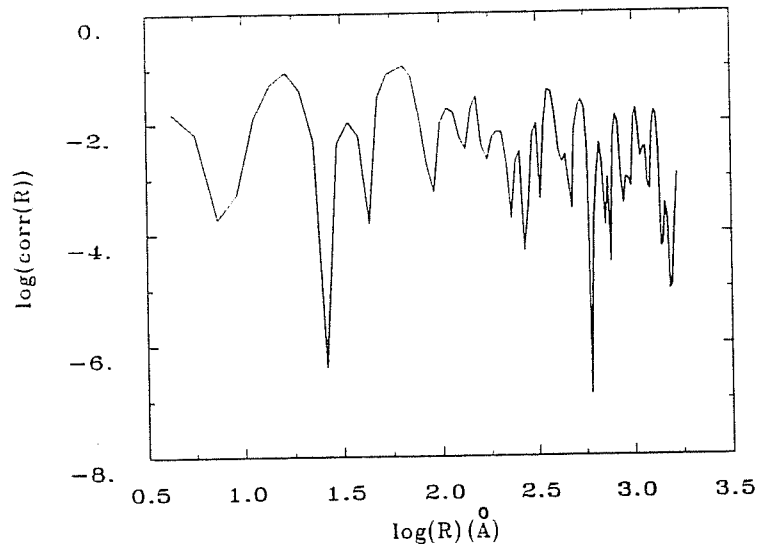

Figure 3.13:
Trend of the phase correlations (Eq. (3.12)) at 1000 K calculated with a MD box $22 \times 13\sqrt{3}$. We expected to be in a floating phase.

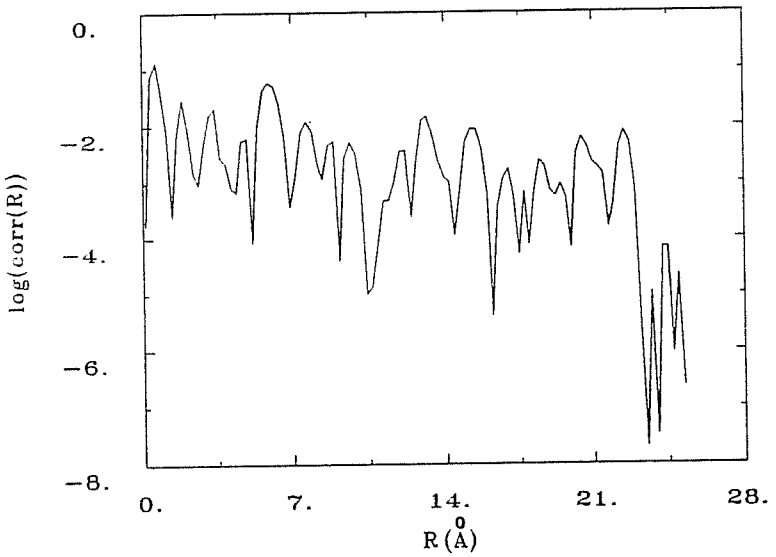

Figure 3.14:
Trend of the phase correlations (Eq. (3.12)) at 1500 K calculated with a MD box $22 \times 13\sqrt{3}$. We expected to be in a disordered phase.

it is already predetermined whether one will go for an uniaxial or hexagonal reconstruction. In fact, one should from the beginning construct an hexagonal cell to be able to get an isotropic compression. However, this cell shape poses a problem for the uniaxial reconstruction, in that if $[1\bar{1}0]$ is the reconstruction direction, the fcc/hcp domain walls must be oriented along $[01\bar{1}]$ or $[\bar{1}01]$ instead of the orthogonal $[11\bar{2}]$ direction in order to have a match through the periodic boundary conditions. A similar problem is encountered when using a 60^0-parallelogram box.

We have seen, moreover, that the many-body term together with the fixed number of atoms, contribute to keep very stable the reconstruction with the typical division in fcc and hcp domains, allowing overheating of the system.

Furthermore, the size of the box in a MD simulation cannot be large enough and, perhaps, the simulation times cannot be sufficiently long to allow roughening of the walls, and formation of vortices, as one expects in such systems. Just these phenomena should cause disappearance of the reconstruction.

Chapter 4

Review of physical properties of vicinal surfaces

4.1 Surface crystallography

By cutting a crystal a few degrees away from a low index orientation, it is possible to create a surface, which does not correspond to one of the equilibrium faces of the crystal. This particular surface is called a "vicinal".

For clean vicinal surfaces it is often more energetically convenient, as it will be clear further, to assume a stepped configuration, than to break up into large facets of low index orientations, i. e., they assume terraces of the nearby low index plane and they can be, usually, one or a small number of atomic layers high.

The model of a vicinal surface, composed of terraces of low-index orientations separated by monoatomic steps, is an example of the Terrace-Ledge-Kink (TLK) model, first introduced and investigated by Kossel et al. [73] and Stransky et al. [74]. The TLK model is based on a very simple scheme of a crystal (Kossel crystal); it is viewed as a compact structure packed together out of rigid elementary building blocks, which may, for instance, be of cubic shape, corresponding to lattice cells. It completely ignores lattice vibrations, electronic structure, dislocations, relaxations and other essential features of realistic crystal surfaces. In the TLK model the step direction and the average step separation are determined by the orientation of the vicinal surface. Also the distance between steps (that is, their density) is simply related to the inclination angle towards the low index plane. If the

normal of the macroscopic vicinal surface is inclined to the normal of the low index surface by the angle θ and the step height is d (which is equal to the separation between the low index planes), the average distance between neighbouring steps is then given by $\Lambda = d \tan\theta$. The average direction of the steps is parallel to the line of intersection between the low index and the vicinal surface. The step direction may coincide with the direction of close-packed atom rows (low-index direction). In this case the edges are smooth. For other directions the edges will contain kinks which connect portions of smooth edges.

Usually there are two ways to indicate vicinal surfaces, that is simply by the Miller indices of the direction, which forms the angle θ with the low index direction, or by a more complete nomenclature due to Lang et al. [75], which indicates the terrace orientation, the terrace width and the edge orientation. In general a stepped surface is represented in this scheme by

$$E(S) - [m(h,k,l) \times n(h',k',l')]. \tag{4.1}$$

E designates the element, the postscript S means "stepped", m gives the number of rows in the terrace of (h,k,l) orientation, n the number of atomic layers giving the step height and (h',k',l') the edge orientation.

There are three main types of structural features that can appear on vicinal surfaces; besides the configuration characterized by one atom high steps separated by terraces of width m, already described (the monoatomic height step terrace configuration), there are multiple height step configurations (where the steps are higher than one interplanar distance) and the "hill and valley" structure. This consists of very large ($\simeq$100 Å) low Miller index facet planes, separated by multiple height steps, which would give to the surface an aspect of an ensemble of hills with valleys between them.

4.2 Experimental observations

Stepped surfaces may be prepared either by cleavage or by standard metallographic procedures. In the first case the overall surface orientation is that of the low index cleavage plane. Regions of various step densities and step orientations are more or less randomly distributed over the so prepared surface. Temperature treatments of cleaved surfaces will tend to

establish the low index plane all over the surface because this is the state with the lowest surface energy.

If, instead, a macroscopically flat vicinal surface has been prepared by usual metallographic techniques and has been given an annealing process, it will develop either a regular step structure or a "hill and valley" structure formed by facet planes of lower Miller indices, as above.

Ordered steps have been sometimes observed on both metals and semiconductors; so they might appear on Miller index surfaces of all types of crystalline materials, independently of the chemical bond. Many experimental and theoretical studies, as it will be explained later, have been done about the stability of this type of surfaces with respect to that of the lowest free energy low-index surfaces.

Anyhow, it is especially on metal vicinals that regular step structures are predominantly observed and are stable up to temperatures close to the melting point. This is true especially for vicinals of close packed low index planes with edge directions parallel to low index orientations. When, instead, the edge directions are not parallel to a low index orientation, there is the formation of kinks which are usually randomly and not periodically spaced. Vicinals with high kink concentration show a marked tendency to form "hill and valley" structure (that is they are composed of microfacets of neighboring orientations). Such stabilized structures on vicinals with step edges parallel to low index directions have been observed on Cu(100), Pt(100), Pt(111), W(110), Pd(111), Ni(100), Ni(111), Au(111), Ir(111) [76] by LEED. Also on semiconductors Ge(111), Ge(100), Ge(110) [76] ordered step structures have been observed at least up to 850°C , which is already close to the melting point of 937° C.

He-atom diffraction studies have been done on Pt(997) and Cu(117) [77,78]. They can give informations also about the electron charge distribution at the step. A rounding of the electron distribution at the step-edge in both cases is observed.

To study the nature of roughening transition much experimental work has been done on vicinal surfaces. In this respect the (K,1,1) surfaces of fcc metals, especially Cu and Ni have been studied with He-Atom-Diffraction [79,80,81] and Synchrotron X-Ray-Scattering [82].

Also copper, nickel and silver (100)-vicinals under oxygen, sulphur and nitrogen [83,84,85,86] have been investigated, and in particular their faceting behaviour. It is seen that they obey a structural relationship between the

stable vicinal facet appearing after faceting and the superstructure-mesh on the low index-face at the same coverage.

Recently a series of studies has been initiated to check a possible faceting of vicinal faces of bare reconstructed low-index orientations. In particular, regular and stabilized stepped structures have been observed on metal surfaces, which are intrinsically reconstructed, in particular on Au(111) and Au(100) [3,38,88], and also on semiconductor surfaces, like Si(111) [89]. For more details see Section 4.5. This fact has made us suppose, as it will be explained later, that a mechanism, which can compel vicinal surfaces to have a regular stepped structure is just the reconstruction.

In general the structural properties may be drastically changed by impurity adsorption. Usually the tendency for facets formation is enhanced by this process, but there are also indications that impurities can stabilize regular step structures. Also in other physical situations regular step structure on vicinals become favourite, for instance in kinetics of step motion under condensation and evaporation and in capillarity driven shape change of metal surfaces [76].

Experimental observations on vicinal surfaces (like Pt [91]), which are stable up to the melting temperature have been performed; many studies have been done to explain why the various mechanisms, which should destabilize the stepped structure (surface diffusion, evaporation, bulk diffusion) cannot be sufficient to destroy the ordered configuration. The remarkably strong thermal stability is probably due to the difficult routes which the crystal must take to develop an equilibrium shape.

From the experimental observations one may so conclude that the regular step structure on vicinal surfaces is one of the possible equilibrium state of lowest free surface energy. The other state conforms with a "hill and valley" structure set up by lower index facet planes. The theoretical reasons for the prevalence of one structure or another will be clear in Section 4.3.

The differences in free surface energy of the two possible states may be quite small and may change sign with temperature, as indicated by the reversible surface structure of Ge(110) vicinals [90]. If the vicinals show irreversible faceting at higher temperatures, one may regard this as the state of lowest energy in the entire temperature range. One might attribute the initial lack of well developed facets to the rather low mobility of surface atoms, not allowing the equilibrium structure to form within a reasonable time.

4.3 Theoretical considerations: the Wulff plot and the faceting of a vicinal surface

One of the most important theoretical problems connected with the stepped surfaces is that of their stability at high temperatures. In fact many studies have been done about the reasons for which a vicinal in some cases chooses a regular stepped structure instead of an "hill and valley" structure and about the surprisingly high stability of regular stepped configurations with respect to thermal effects.

Before reviewing briefly these problematics, we must recall the meaning of the most important variable in surface thermodynamics, the surface free energy (called also the specific surface work or, sometimes, surface tension) [92,93]. It can be defined as the reversible work γ required to form the unit area of new surface by cleavage at constant temperature and pressure, that is the partial derivative of the Gibbs energy G of the whole system with respect to the area of surface formed (at constant T, pressure P, and number of moles for each component n_i) $G = G(P,T,n_i,A)$, $\gamma = (\partial G/\partial A)_{P,T,n_i}$. It can be symmetrically defined in terms of the free energy in conditions of constant volume or, more frequently, in terms of the grand potential Ω (at constant T, volume V, chemical potential μ).

Once introduced this thermodynamical variable, the "geometrical thermodynamics" studies the dependence of γ from the orientation of the faces, solving the problem of how this function can be used to determine the equilibrium form of the crystal.

The equilibrium shape of a crystal is determined by the condition for the free energy F to be a minimum (for given T, μ, and volume V of the crystal) or, which is the same thing, by the condition for its surface part to be a minimum [94]:

$$F_s = \int \gamma ds = minimum \tag{4.2}$$

the integral being taken over the whole of the crystal. Let $z = z(x,y)$ be the equation of the surface of the crystal, and let $p = \partial z/\partial x$, $q = \partial z/\partial y$ denote the derivatives, which determine the direction of the surface at each point; γ can be expressed as a function of these partial derivates, $\gamma = \gamma(p,q)$. The equilibrium form is given by the condition

$$\int \gamma(p,q)\sqrt{1+p^2+q^2}dxdy = minimum \tag{4.3}$$

with the added condition of constant volume

$$\int zdxdy = constant. \tag{4.4}$$

This mathematical condition, can be shown to be equivalent to the well-known geometrical construction introduced by Wulff [95]. It consists of plotting radially $\gamma(\theta)$, as a function of the angle θ, which the high index Miller surface forms with the corresponding low index Miller direction. The equilibrium crystal shape is then obtained drawing planes perpendicular to the radius vector at each point of the γ plot. Then the volume, which can be reached from the origin, without crossing any of the planes has a shape similar to the equilibrium shape of the crystal. In other words the interior envelope of the family of planes, described above, is a convex figure, whose shape r(ϕ,T) is that of the equilibrium crystal, where ϕ is the angular variable in describing the crystal shape.

It is interesting to note that there is a relation, which connects θ, the angular variable in the Wulff plot, with ϕ, the angular variable on the crystal shape: the plane perpendicular to the direction θ is tangent to the equilibrium crystal shape at a point (or points) labelled by ϕ; this relation may or may not be one-to-one, as it will be described further below. If the surface free energy is $\gamma(\theta,T)$, the Legendre transformed free energy with natural variable ϕ and T is just the equilibrium shape r(ϕ,T). This is natural, if we think that the Wulff plot provides tangents to the crystal shape, and it is this geometrical notion of tangency which is at the center of the idea of the Legendre transformation (Fig. 4.1). If the γ plot has strong cusps in a certain direction, the equilibrium crystal shape will be a polyhedron formed by planes, whose normals coincide with the cusps directions. These directions correspond to orientations of low Miller indices. All planes that are not part of the equilibrium shape are unstable.

In summary, the equilibrium shape of crystals at low temperatures [96] is characterized by the presence of facets, i.e. plane sections, each of which corresponds to the emergence to the surface of a crystal face with definite Miller indices.

This nonanaliticity of the shape is a manifestation of the dependence of the surface energy of the crystal on the angles determining the orientation

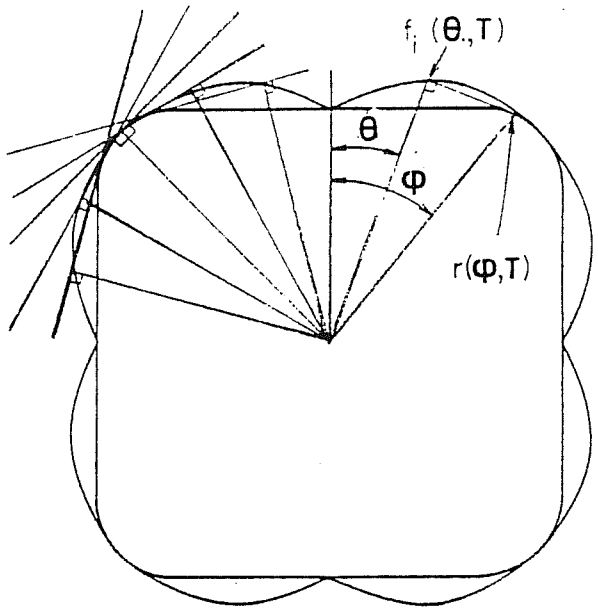

Figure 4.1:
The Wulff construction. The outer curved line is the polar graph (the Wulff plot) of $\gamma(\theta, T)$ at fixed T. The inner figure is the corresponding crystal shape $r(\phi, T)$. Straight lines illustrate the construction described in the text.

of the faces. Specifically the surface energy is a continuous function of the angles, but this function has discontinuous derivatives everywhere. The linear dimensions of the planar parts for the various faces are proportional to the corresponding jumps of the angle derivatives of the surface energy, which in turn are proportional to the step energy for the face in question. All these quantities have their greatest value in the case of the most closely packed faces, and rapidly decrease with increasing Miller indices.

The thermal motion washes out the planar parts of fairly small dimensions; therefore, at any finite temperature only facets with not too large indices occur on a surface. A rise in temperature usually leads to the disappearance of the planar parts for the increasingly close-packed faces, and, finally, to the total disappearance of the facets. Therefore each crystal is characterized by a set of critical faceting-transition temperatures (or roughening transition temperatures). The highest of them is the temperature below which the crystal first assumes its nonanalytic equilibrium shape. The rest are connected with the appearance of planar parts of the various types

of faces. It may also be said that the discontinuities of the angle derivatives of the surface energy or the finite step-energy values first appear at the critical points of the faceting transitions. The concept of roughening-phase transition was introduced by Burton and Cabrera [97].

The roughening transition of a crystal surface is characterized macroscopically by the disappearance of a facet of a given orientation from the equilibrium crystal shape. This corresponds to the disappearance of a cusp in the Wulff plot. Microscopically, instead, the roughening transition is characterized by the free energy of a step on the facet becoming zero, or alternatively by the appearance of strong fluctuations in the location of the facet. A microscopic description of the roughening transition [98] can be achieved within the solid-on-solid model (SOS model). It describes the interface in terms of a set of discrete-valued variables h_{ij}, defined on a two-dimensional lattice, describing up to which height the interface is built up at each lattice site $[ij]$. One obtains a statistical mechanical model by assigning to each interface configuration h_{ij} an energy $E(h_{ij})$. A SOS model is shown to undergo an infinite-order phase transition of the Kosterlitz-Thouless type at the roughening temperature T_r (which results, usually, one-half of the experimental melting temperature T_M). The roughness of the surface is described by the height-height correlation function in reference to the low-temperature smooth surface. The correlation-length associated with this function diverges exponentially as $T \to T_r$ and stays infinite for $T > T_r$.

For vicinal fcc (K,1,1) surfaces a statistical description of the thermal roughening of the steps line was recently given by Villain, Grempel and Lapujoulade [79] based on a modified SOS model. In this model, the hamiltonian describing the atomic picture of a rough surface assumes two interaction energies, the step-step repulsive energy w_n and the kink creation energy W_0. Having $w_n \ll T \ll W_0$ under general experimental conditions, the theory derives the roughening transition temperature T_r from the relation

$$(w_n/T_r)\exp(W_0/T_r) = R. \tag{4.5}$$

Coming back to the description of the equilibrium crystal shape, derived from the Wulff plot, we must observe that besides the planar parts, the

crystal surface may contain singular lines and points at low temperatures. The first of them are the so-called edges, along which finite jumps occur in the orientation of the normal to the surface; the second are conical (or angular) points, near which the crystal surface has the shape of a cone. The appearance of these anomalies, as the temperature is lowered also determines a set of critical temperatures characteristic of the given crystal.

Analysing in more detail the construction of the Wulff plot, we must observe that every point on the equilibrium crystal shape has a tangent plane belonging to one (or more) directions θ in the Wulff plot, whose perpendicular planes are not tangent to the equilibrium crystal shape. When this happens, the equilibrium crystal shape lacks tangent planes with certain orientations. As a result, it posses sharp edges (or points). Such regions, which do not contribute to the equilibrium crystal shape, have no significance, and, indeed, from a fundamental statistical point of view they are not even well defined! Passive regions of the Wulff plot are like metastable states in bulk thermodynamics [99]. They appear at $T = 0$ and in mean-field approximations, where such states can be given a clear definition; however, for $T \geq 0$ they are not and cannot be defined thermodynamically, since they do not persist at long times. In fact, as it will be explained in more detail later, it has been shown by Herring [100] that, if θ does not contribute to the equilibrium crystal shape, then a lower free energy can always be achieved by taking in place of the flat interface a "hill-and-valley" formation, which uses only orientations which appear on the equilibrium crystal. Thus, what happens in practice is that the flat surface does not equilibrate but rather reconstructs (on an appropriately long time scale) into Herring's "hill and valley" formation. Such reconstruction, called thermal faceting, is in fact, observed experimentally on high index surfaces of certain metals at relatively high temperatures. It may be interesting to observe that thermal faceting is visible only when it occurs on accessible time scales. Large-scale "hill-and-valley" formations require macroscopic times. What is typically observed experimentally is only the initial stages, which require transport only over short distances. Unstable interfaces may remain unreconstructed for long times. In conclusion the upshot is that the flat surface in these particular directions never equilibrates, so the equilibrium measurements cannot be made. Thus passive regions of the Wulff plot lack thermodynamic significance; in other words, the directions belonging to these regions are forbidden.

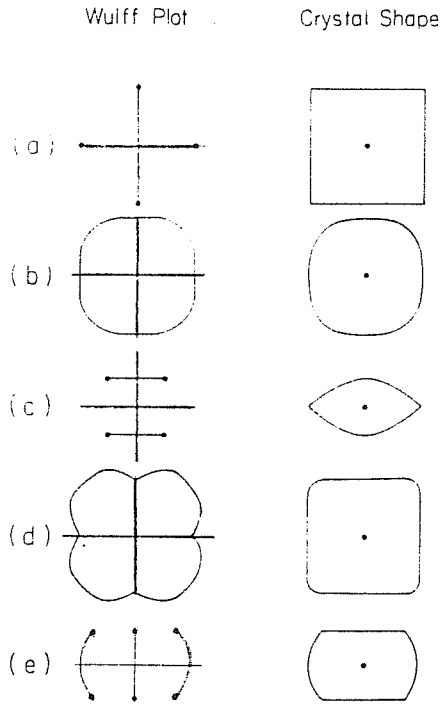

Figure 4.2:
A generic selection of equilibrium crystal shapes with corresponding Wulff plots. Faceted and curved surfaces may appear, joined at sharp or smooth edges in a variety of combinations:
(a) entirely faceted, no curved surfaces;
(b) entirely curved, no facets;
(c) curved surfaces with edges, but no facets;
(d) facets and curved surfaces, no edges;
(e) facets, curved surfaces and edges.

In summary, from the precedent analysis, we can say very briefly that the equilibrium form of the crystal determined by this procedure, will include a number of plane areas (corresponding to crystal planes with small values of the Miller indices), which are joined by rounded regions instead of intersecting at sharp angles. The size of the plane areas rapidly decreases as the Miller indices increase.

To show some examples, various equilibrium crystal shapes, which can be derived from the various Wulff plots, are displayed in Fig. 4.2, with the corresponding Wulff plots [99]. Of course, it is the interatomic forces which determine which one of these possibilities is actually realized.

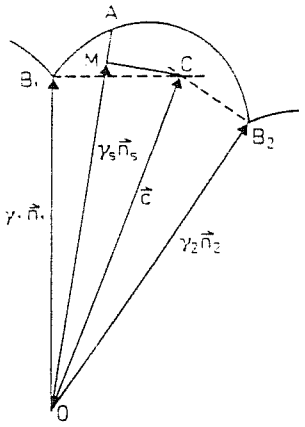

Figure 4.3:
Section of γ plot illustrating reduction in surface energy for direction $\vec{n_s}$ by a "hill and valley" structure formed by facets of orientation $\vec{n_1}$ and $\vec{n_2}$.

A theoretical question, linked to the problems now examined, is connected with vicinal surfaces [76], whose γ values are described by portions of the γ plot in vicinity of the corresponding low index cusp directions. The question is, whether a regular monoatomic stepped structure or a "hill and valley" structure leads to a lower value of the surface free energy per unit length. Herring [100] has been the first, who has given a general treatment of the conditions for faceting from the shape of the γ plot, and, later, Bennema [101] has reviewed in more detail Herring's theories.

Very briefly this condition consists in observing the position of the point (called M), which is given by the projection (onto the radius vector of a particular vicinal) of the vector joining the origin with another special point (called C), obtained as the intersection of three facet planes, drawn normal to three radius vectors (called, for istance OB_1, OB_2, OB_3). If M lies inside the γ plot, the vicinal may lower its free energy by forming the facets ("hill and valley" structure) with the normals over indicated. If, instead, it lies on the γ plot, the terrace-step structure is favourite (see Fig. 4.3). We must observe that the surface free energy of a faceted surface per unit area of the macroscopic surface would be

$$\gamma_s = \gamma_1 f_1 + \gamma_2 f_2 + \gamma_3 f_3, \tag{4.6}$$

where γ_1, γ_2, γ_3 designate the surface energies of the three facet planes and f_1, f_2, f_3 are the areas of the planes per unit projected area in the plane of

the macroscopic surface.

Various models [93] of γ have been derived from different types of interaction potentials, especially for pairwise interatomic interactions. In all these models the crystal is taken to be semi-infinite and defect-free and γ is simply equal to the energy per unit area of surface associated with breaking at $T = 0$ of the bonds that would connect the crystal to that part occupying the other half of space.

It is interesting to note that the Wulff plot, derived from these broken bond models with only first neighbour interactions, is composed of spheres which meet each other in steep cusps and valleys. Cusps correspond with flat faces occurring on the equilibrium form and valleys to stepped faces. The spherical areas correspond to kinked faces.

The conclusion, derived from the analysis of different types of interaction, seems to be that faceting is an indication of the deviation from the ideal pairwise bonding behaviour. In fact the inclusion of longer range interactions leads to the occurrence of additional cusps (in the limit a cusp would be predicted at all rational orientations [100]). With a simple pairwise interaction, the portions of the Wulff plot between two cusps, corresponding to low index orientations, are spherical.

Besides the pairwise interaction model, spherical portions in vicinity of a cusp can also be phenomenologically rationalized in terms of a step structure, for which an additional step energy β per unit step length has been introduced [76]:

$$\sigma(\theta) = \cos\theta \left(\gamma_o + \frac{\beta}{d} \sin\theta \right) ; \tag{4.7}$$

γ_o is the free surface energy of the low index direction, d the step height, θ the angle between the vicinal and the low index surface direction. It can be shown that the Wulff plot derived from the precedent expression has a spherical shape with a radius, which increases with the strength of β.

Herring has showed that the condition of stability of a stepped structure respect to faceting in facets with normals $\vec{n_1}$, $\vec{n_2}$, $\vec{n_3}$ is fulfilled when this spherical portion of the γ plot lies over or inside the sphere given by the equation $\vec{c} \cdot \vec{n_i} = \gamma_i$ where $\vec{c}$ represents the vector joining the origin with the $i-th$ point, obtained as the intersection of the three facet planes with normals $\vec{n_i}$ i=1,2,3. This condition is naturally equivalent to that before described.

The condition of stability respect to faceting may be fulfilled or not depending on the material and on the orientation. β is higher for kinked steps, giving less stability to the vicinal.

4.4 The interaction among steps on a stepped surface

If we introduce higher order terms in the phenomenological expression above described (4.7), we can take into account the step-step interaction without making any hypothesis about the nature of the interatomic forces, other than that the step interaction energy goes to zero at sufficiently large step distance. The expression, which has been utilized, results:

$$\sigma(\theta) = \cos\theta(\gamma_o + \frac{\beta}{d}\tan\theta + \alpha_2\tan^2\theta + \alpha_3\tan^3\theta + ...). \qquad (4.8)$$

By this model it has been possible to estimate, from the plot of Cu(100) vicinal the value of $(\beta/d) \simeq 10^{-2}$ eV per atom at 100 K.

We have followed a similar way for our studies of interacting steps on gold surfaces, as it will be explained in Chapters 5 and 6.

The nature of the interactions between surface steps has been a very controversial question. The problem has been considered, using the pair interaction model by Wymblatt [102] for steps on the (100) surface of a fcc cubic crystal. The interactions were represented by the Morse potential:

$$\psi(r_{ij}) = D(e^{-2\alpha(r_{ij}-r_o)} - 2e^{-\alpha(r_{ij}-r_o)}). \qquad (4.9)$$

D, r_o, α are empirical constants derived from known bulk properties; r_{ij} is the separation of a pair of atoms. The interactions of pairs of steps have been found to be weak and repulsive.

Also considerations made on the entropy associated with the formations of the kinks of the step edges [104] take to the conclusion that the interaction among steps must be repulsive.

The origin of the step-step repulsive energy arises from the lattice strain in vicinity of a step. In particular, the possibility of a long-range elastic interaction, due to the overlap of the displacement fields at the steps has been suggested by Blakely et al. [103].

The interaction energy between two steps separated by a terrace long l can be thought similar to the interaction energy of two parallel walls lying a distance l apart, deduced within an elastic model [105]. It results that the interaction energy per unit length of the wall (or the step) is a long-range interaction, which is proportional to the inverse of the square of the distance l between walls (or steps). This kind of step-step interaction, both short- and long-ranged, gives a cubic term in the step density [106] in the free energy per unit area.

We should recall that also dipolar interactions between steps have been also considered; they have a l^{-2} dependence too and can be attractive and repulsive, while longer ranged interactions related to Friedel oscillations have a much more complicate trend [42].

If the interaction energy between two steps (per unit length) separated by the distance l is proportional to l^{-2}, the energy change w_k when a step is shifted with respect to the neighbouring ones is expected to vary as l^{-4} [79,80]. This dependence seems roughly to be verified in Cu(100)-vicinals (K,1,1), for which some estimates of w_k and W_0, the kink formation energy, from roughening temperature measures have been given [80].

4.5 Experimental observation on interplay between steps and reconstruction

Recent experimental observations of regular arrays of steps on Au(111), Au(100), Si(111) [3,37,38,89,88,87] vicinals seem to suggest, being all these surfaces intrinsically reconstructed, that reconstruction on a crystal surface may be very effective in "locking" the distance between steps. In particular, steps might tend to rearrange themselves so as to form terraces, whose length is such to accommodate an integer number of reconstructed unit cells.

In particular, for the Au(111)-vicinals by STM [3] regular $[1\bar{1}0]$ [87] and $[11\bar{2}]$ steps have been observed, the latter with a periodicity in the $[1\bar{1}0]$ direction, which exactly fits the well-tested reconstruction periodicity of 23 of the flat surface; for the Au(100)-vicinals by LEED [88] and Electron-Microscopy (Profile Imaging, TEM, TED) [38,37], $[01\bar{1}]$ steps have been seen with a periodicity of five (or slightly longer) in [011] direction, which recalls the (1×5) structure of flat Au(100); for Si(111)-vicinals [89], inclined

along the $[11\bar{2}]$ zone-axis, a study in temperature has shown that the inclination of the surface changes continuously and reversibly from 6.3 ± 0.4^0 (steps of height 3.12 ± 0.07^0 Å and separation 28.4 ± 1.6 Å) at high temperature ($T \geq 810K$), where there is no reconstruction to 17.0 ± 3.0^0 (steps of the same height with separation 10.4 ± 1.7 Å) at low temperature, where the (7×7) reconstruction appears.

4.5.1 Experimental studies of (K,1,1) Au(100)-vicinals

The first studies on stepped Au(100) were done by RHEED [33] by Melle and Menzel. They found a rotation of the structure, a $\begin{pmatrix} 26 & 0 \\ -1 & 5 \end{pmatrix}$ reconstruction on stepped surfaces inclined along the $[01\bar{1}]$ zone-axis. The close packed atomic row is then rotated by α_1=0.7° respect to the [011] direction of the fcc lattice.

Also Sotto et al. [88] by LEED have observed several faces, cut along the $[01\bar{1}]$ zone-axis, (K,1,1) vicinals. The LEED patterns, even if very intricate, have shown that, except for the faces having large terrace widths (i.e, vicinals with Miller index K$\geq$ 11) and the (5,1,1), a faceting occurs on the other faces. In all cases, there appear reconstructed (100) facets and a regrouping of (5,1,1) facets.

T. Hasegawa et al. [38] by Profile Imaging have observed on the terrace of the (K,1,1) vicinals the (28×5) superstructure. In Fig. 4.4 it is shown

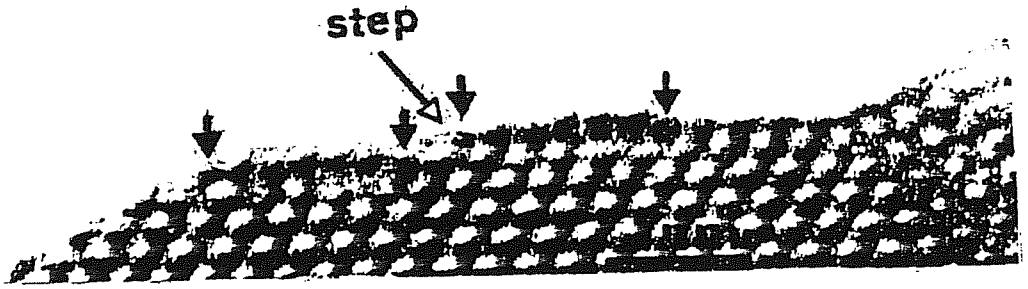

Figure 4.4:
(100) reconstruction around a step. It is seen the 7-onto-6 terrace-configuration [38].

that in the [011] direction, the five-period superlattice persists right up a

step, while over a terrace it seems that a 7-onto-6 reconstruction prevails. The atoms, for each [011] row dispose symmetrically around the central atom, which rises up in the [100] direction. The atoms at the end of the row, on the terrace, instead, are in valley. In their measurements, it has been also noted that the relative shift of the structure at the step is 3/2 of the atomic distance.

More detailed studies by TEM and TED [37] have confirmed for stepped Au(100)-vicinals the superstructure as $(p \times q)$, where p and q fluctuate around the central value of 28 and 5. Their experimental observations have been interpreted in terms of an alternation of the two hard spheres models, the top-center and the two-bridge models, by which also the (1×5) reconstruction of flat Au(100) has been explained. This alternance keeps also across the steps, as it is shown in Fig. 4.5. The names of these two

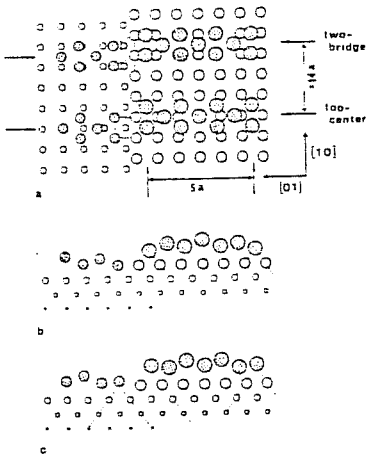

Figure 4.5:
(a) Top-center and two-bridge sites of the hexagonal lattice of the (28×5) structure (top view). The alternating top-center site and two-bridge site along the multifold direction continues on the lower terrace.
(b)Side-view of the (28×5) structure for the top-center site and for
(c) the two-bridge site.

models, which give an hexagonal arrangement in the topmost layer, derive from the fact that in the two-bridge model the atoms in the first layer in registry with the second one occupy twofold bridge-sites, while in the top-center model they are positioned directly on top of the atoms in the second layer.

Since the two models appear alternatively on flat surfaces, they are expected to have a similar energy on wide surfaces. Anyhow, the preference of the top-center model on narrow terraces was found to be due to the fact that the reconstruction can be terminated at up and down steps by the most stable hollow-site atoms in the top center model.

These experimental studies have also described the rotation of the top-most hexagonal layer on the terraces with respect to the underlying square lattice. The conclusion seems to be that the rotation of the unit cell vectors of the hexagonal lattice respect to the square substrate is a characteristic of the flat (100) surface, since in regions of low step density (large terraces) is bigger than in regions of high step density (small terraces). Besides that, this rotation is minimum for terraces with $[01\bar{1}]$ steps respect to terraces with [011] steps.

It may be interesting to observe that in TEM and in TED analysis the periodicity of the superlattices in the fivefold direction fluctuates largely around $q = 5$ and reaches even $q = 4$ and $q = 6$. The unevenly spaced superlattice fringes are often seen on narrow terraces in TEM images, while it is not noticed on flat rotated superlattices. So this effect might be caused only by steps and might have been concealed on flat surfaces.

4.5.2 Experimental studies of (M+1,M−1,M) Au(111)-vicinals

Several scanning-tunneling microscopy (STM) studies of surface steps on Au(111) have recently appeared [3,87,108,109]. From these studies, one can extract a fair amount of information on the step structure and on their interplay with the reconstruction of flat surfaces.

The first STM study of Au(111) surface and Au(111) vicinals has been performed by Kaiser and Jaklevic [3]. In their experiments, the resolution is not sufficient to resolve individual atoms. However, the presence of steps can be unambiguously detected, as shown in the maps in Fig. 4.6. A first topograph (Fig. 4.6 (a)) shows an array of monoatomic steps (each 2.35 Å in height) parallel to the $[11\bar{2}]$ direction in the surface plane. There is no sign of any isolated atom or single row on this surface. Scans along various directions showed no evidence of any corrugation effect (within their vertical resolution 0.1 Å). Interestingly, the steps are almost equally spaced with a periodicity of 23 ± 2 atomic rows, i.e., nearly equal to the

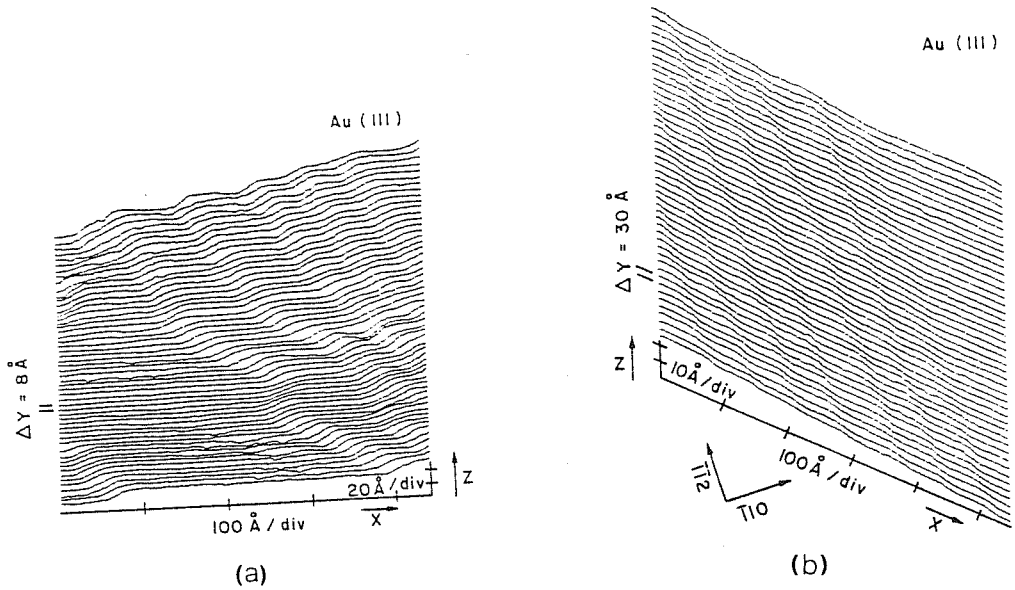

Figure 4.6:
(a) Surface topograph of Au(111) showing an array of monoatomic steps aligned with the $[11\bar{2}]$ direction. The array extends through the entire area covered by this image: (550 Å$\times$ 1400 Å). The array forms an ordered step reconstruction with a period of 66$\pm$6 Å (23 $\pm$ 2 atomic row spacings).
(b) Surface topograph of Au(111) showing an array of wide, flat terraces linked by large amplitude steps. The image covers a region of (450 Å$\times$ 425 Å). The step-height is uniform through this large area and is equal to seven atom-layers. The facets exposed at these steps are (311) and (100) type.

Au(111) reconstruction periodicity length [34,50,2,54,55] The regularity and periodicity of these steps continues over many periods and over a very large surface region.

The precedent observations suggest, for Kaiser and Jaklevic, a picture of the reconstruction on Au(111) in terms of step arrays rather than a top layer contraction. In other words, they believe the stepped configuration to be the stable reconstructed surface, which, in their interpretation, should be lower in energy than the flat (111) surface. Our calculations will demonstrate that their conclusion is wrong because a stepped surface is always in a metastable state respect to that of the flat one. However, reconstruction may play a role in *stabilizing* the distance between the steps to a value close to the reconstruction periodicity, thus explaining their observations.

In a second topograph (Fig. 4.6 (b)), a region with an average 10^0 slope, instead of consisting of many closely spaced narrow monoatomic steps, is found to facet into wide flat (111) regions separated by seven-atom-height steps exposing a (3,1,1) facet. (100) facets also appear. In this

case, the absence of periodic monoatomic steps contradicts their previous interpretation, and it rather indicates that a 10^0 slope corresponds to a vicinal surface *unstable* with respect to faceting.

Finally, in a very recent STM study, Brodde et al. [87] investigate a stepped Au(111) sample, with the steps oriented along the $[1\bar{1}0]$ (i.e., orthogonal to those studied in [3]). Also in this case, the distance between steps (about 30 Å) appears to be rather stable. Moreover, neighbouring steps tend to run parallel to each other even in the presence of kinks, indicating that they interact rather strongly. However, these results are difficult to interpret in terms of a reconstruction-induced stabilization, since the steps are aligned with the contraction direction.

In other recent STM studies with high resolution on Au(111)-vicinals it has been observed that the terraces on stepped Au(111)-vicinals are not flat, as Kaiser and Jaklevic affirmed [3], but show approximatively a corrugation of 0.3 Å [108]. Finally by STM [109] it has been seen also surface features change with time. Individual $[11\bar{2}]$ steps on Au(111) have been observed to move by acquisition of atoms diffusing across terraces or along the steps themselves, at temperatures around 30^0 C.

Motivated by these observations, we have undertaken a study of the structure and energetics of gold vicinal surfaces [107]. We have used the glue force model, which, as discussed in the previous Chapter, is able to explain the occurrence of reconstruction on all the low-index surfaces of Au and therefore constitutes a good starting point for this investigation.

In particular, we have studied the stability of these vicinals with respect to the corresponding low index surfaces and the interplay between steps and reconstruction, testing the idea, suggested by experimental results, that, among the vicinals, those with terrace sizes, which contain about one or few reconstructed unit cells, could be energetically favoured. The results of these calculations are reported in the next two Chapters 5 and 6.

Chapter 5

Simulation of Au(100)-vicinals

5.1 General description of (K,1,1) Au(100)-vicinals

We have undertaken a quantitative study of the Au(100)-vicinals inclined along the zone $[01\bar{1}]$ axis, giving rise to faces with Miller indices (K,1,1), with K odd [107]. These consist of $[01\bar{1}]$ (henceforth x-direction) straight steps, separated by (100) terraces which are $M = (K+1)/2$ atoms wide in the [011] (henceforth y) direction, and infinitely extended along x, as it is shown in Fig. 5.1.

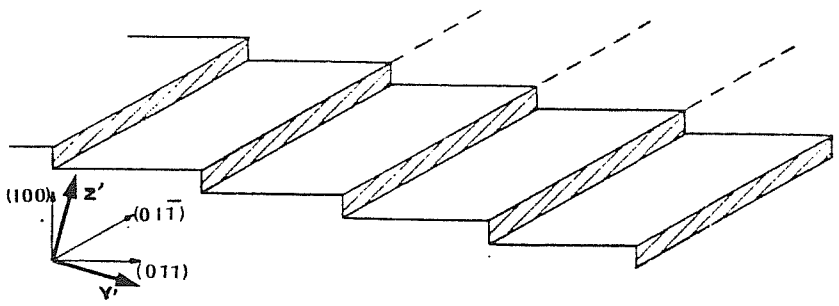

Figure 5.1:
Au(100) vicinals inclined along the $[01\bar{1}]$ zone-axis (geometrical scheme); the dashed line indicates the infinite extension along the $[0\bar{1}1]$ direction.

The length of the terrace along y determines the angle of inclination of the vicinal, $\theta = \arctan(\sqrt{2}/K)$. We also shall call z the [100], y' the [$\bar{2}$KK], and z' the [K11] direction.

$xy'z'$ form an orthogonal system, obtained by rotating the xyz system by an angle θ along the x-axis.

We have seen in the previous Chapter that the basic nature of the flat Au(100) (1×5) surface reconstruction is characterized by groups of five consecutive atoms along a [011] row, which are replaced by groups of six atoms arranged in a zig-zag chain, so as to give rise to a nearly-triangular atomic structure on the topmost layer. Accordingly, we take each (100) terrace to be reconstructed by replacing every [011] row of M atoms with a row of $M + N$ atoms, arranged in a zig-zag chain, creating again a nearly-triangular [1] overlayer. We shall call N the "reconstruction order"; $N = 0$ is the unreconstructed case, in which the perfect square lattice is preserved also on the topmost layer.

Moreover, we require the triangularity of the surface structure to be preserved even across the steps.

In the starting configurations, the atoms are arranged in lattice-like positions, which could be rather far from the true equilibrium positions for our force model. To relax the systems in order to study structure and energetics, we have used energy minimization techniques based on MD, already used for flat surfaces, which we recall to be:

(a) "quenching", where the system is directly driven towards the nearest (or one of the nearest) energy local minimum, by adding friction forces to the dynamics;

(b)"simulated annealing", where the system is thermally annealed at finite temperature, and then gradually cooled down to $T = 0$. For a more detailed description of these techniques, we refer to Section 1.4.

To this end, we have set up a MD box with the edges oriented along $xy'z'$. Periodic boundary conditions are used along x and y', while free boundary conditions are employed along z'. The length of the box along y', L'_y, is such as to accommodate two terraces (and two steps), giving $L'_y = Kd/\cos\theta$ for a (K,1,1), where d is the bulk first-neighbours distance.

[1] A perfect triangular lattice has to be contracted by a factor $(2/\sqrt{3})(M/(M+N))$ along [011] to fit with the terrace length.

Due to the reconstructed nature of the terraces and the requirement that the triangularity has to be preserved across the steps, two terraces correspond to the minimum periodicity length in this direction. Moreover, these two terraces must be kept equivalent from the point of view of the relative positions between the first- and second-layer atoms. This can be achieved by a proper choice of the top-layer registry ($d/4$) along x (see Fig. 5.2 b). In Fig 5.3, instead, an unreconstructed sample is shown with the square lattice also on the topmost layer.

The x-direction, parallel to the steps, does not play any particular role, and the choice of the cell length L_x can be driven by mere convenience. We have chosen $L_x = 5d$; this particular value is low enough to avoid excessive use of computer resources, and has the additional advantage to allow a reorientation of the (1×5) reconstruction parallel to the steps, if the system finds it favourable to do so. This, however, never occurred in our simulations.

For practicality, these MD boxes have been constructed by starting from a (100) slab with two steps in a xyz-oriented box, and applying a rotation operator on the particles coordinates to pass to a $xy'z'$-oriented box. As a result, the area of the slab increases by a factor $1/\cos\theta$. The rotation creates a perfect match between the box and its image at the box boundary. For example, the first layer of one box connects smoothly with the third layer of the adjacent box.

Instead of setting up such a "tilted MD box" we could have constructed a vicinal by starting from a (100) slab with two steps in a xyz oriented box, and modifying only the periodic boundary conditions in such a way to get the match between the first layer of a box with the third layer of the adjacent box. But this way has resulted to be much more complicate than that described previously, due to the various modifications which would have to be done to MD programs.

Initially, our system consisted of 12-layers slab with two surfaces identically treated. The result of an annealing-quenching procedure applied to a (9,1,1) slab of this type is shown on Fig. 5.4.

It is evident that the presence of steps on both surfaces generate forces, which elastically deform the whole slab, tending to flatten the steps and thus lowering the surface energy at the expense of bulk elastic strain energy.

This phenomenon would clearly disappear in the limit of a slab with infinite thickness. The impossibility to simulate significantly larger systems

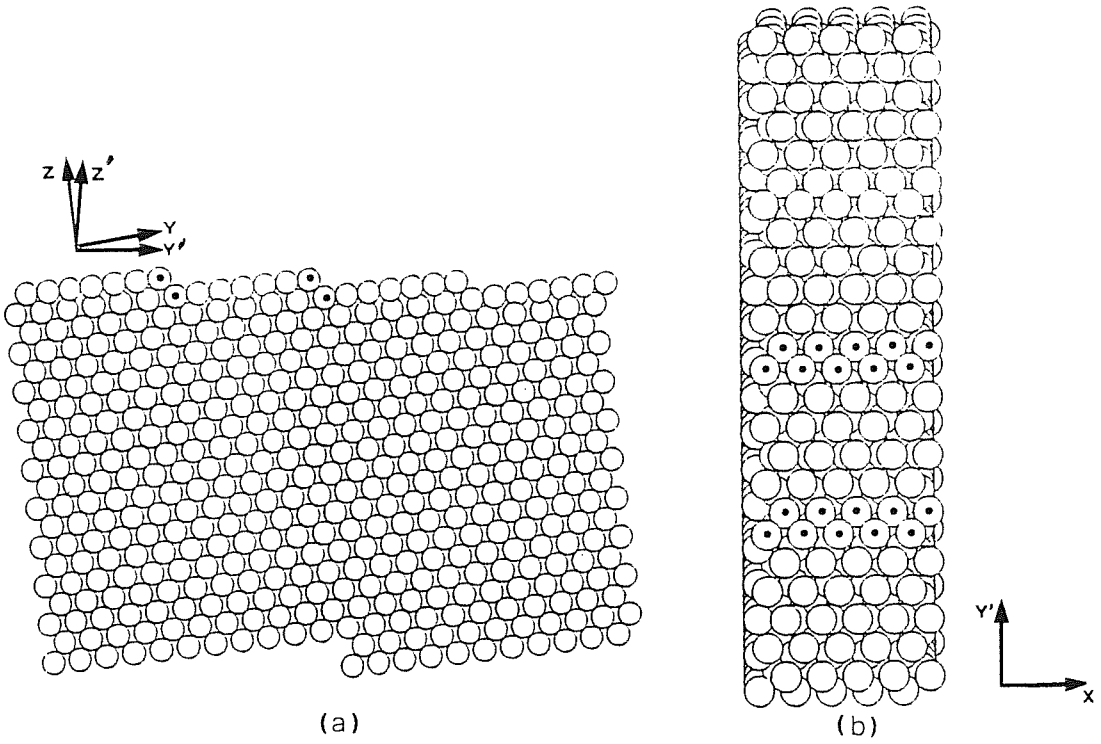

Figure 5.2:
(9,1,1) in the case $N = 1$. Perfect sample. Two MD boxes are represented in y' direction. The atoms at the step-zone are drawn with a •.
(a) Slab profile.
(b) Top view. Note that the triangularity is preserved across the steps.

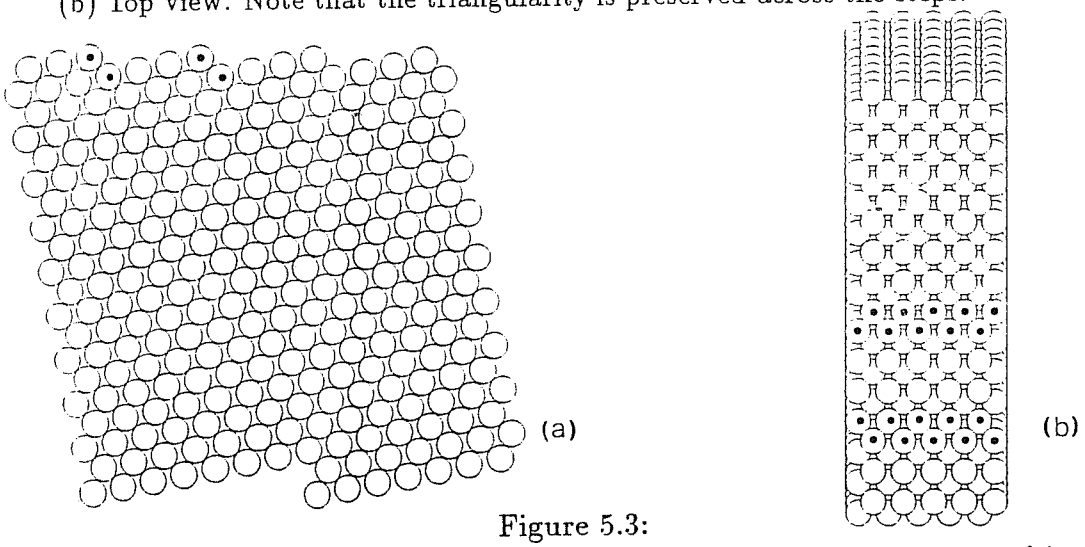

Figure 5.3:
(7,1,1) in the case $N = 0$. Perfect sample. Two MD boxes are represented in y' direction.
(a) Slab profile.
(b) Top view, where the square lattice is well visible.

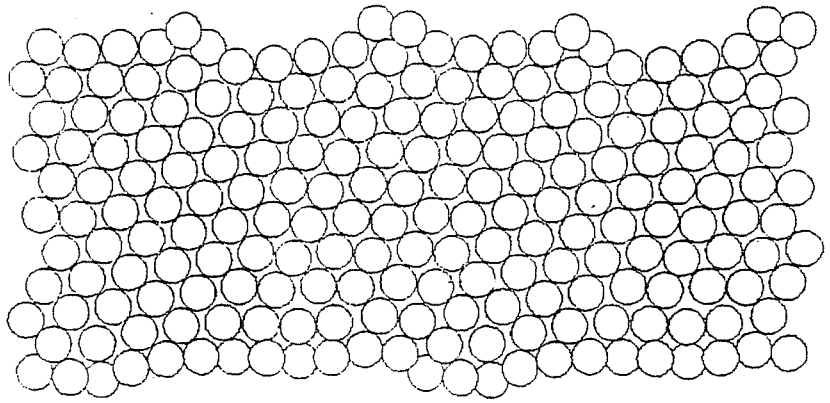

Figure 5.4:
Slab profile with two MD boxes along y' direction in the case $N = 1$ of an annealed (9,1,1) sample with two free surfaces.

forced us, however, to overcome this problem in a different manner.

In particular, we have constructed a 20-layers slab, with five atomic layers frozen (i.e., with the atoms kept fixed in their lattice positions). Due to the short-range character of the interactions in our model, such a small thickness is sufficient to avoid surface effects from the rigid side, that is all moving atoms "see" the rigid side as an infinite bulk. In this way we effectively simulate 15-layers on a fixed seminfinite substrate. Just to have an idea of the size of the samples constructed, the biggest sample considered (59,1,1) in the case $N = 1$, contains 3160 particles and among them 750 are not moving.

To calculate the surface energy we have kept the usual definition

$$\sigma(\theta) = \frac{E(\theta) - N(\theta)\epsilon_c}{A(\theta)} \tag{5.1}$$

taking into account that we are considering vicinal surfaces by the fact that now $A(\theta)$ indicates the area of the tilted surface. $E(\theta)$ is, as usual, the total energy of the slab, ϵ_c the cohesive energy per atom, N the total number of atoms.

5.2 Structure and energetics of quenched and annealed samples

Our MD simulation results are shown in Table 5.1, Table 5.2 and Fig. 5.5, and will be commented in the next Subsections. Anyhow, from the first examination of the surface energy in function of the Miller index K for the orders of reconstruction $N = 0$, $N = 1$, $N = 2$, $N = 3$, we can notice (Fig. 5.5) at once:

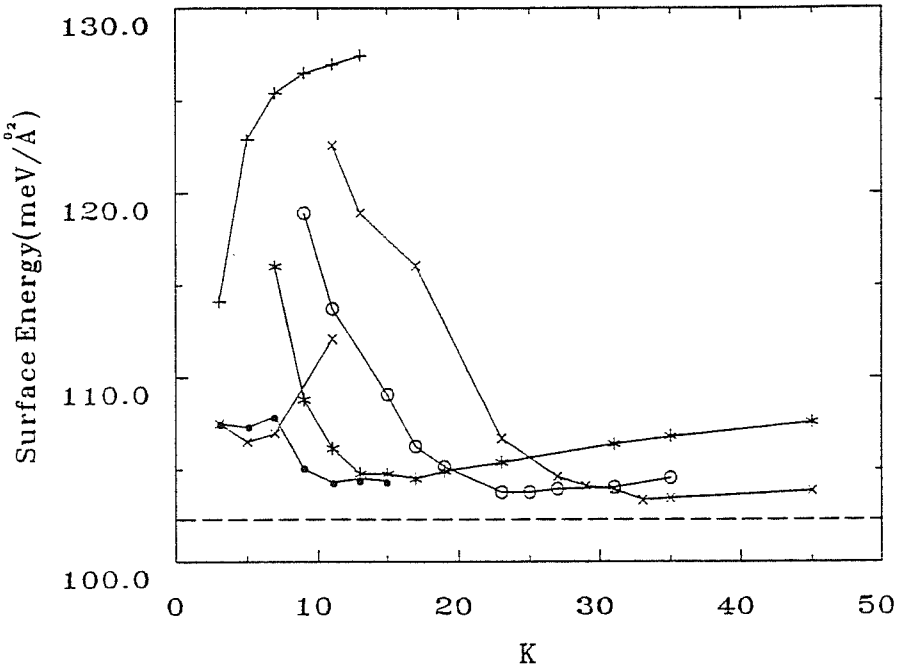

Figure 5.5:
Surface energy versus the Miller index K for vicinals $(K,1,1)$. $+$, $*$, $\circ$ and $\times$ refer to quenched samples for the orders of reconstruction $N = 0$, $N = 1$, $N = 2$, $N = 3$ respectively. $\times$ and $\bullet$ for small K (vicinals with high inclination) refer to few annealed samples in the cases $N = 0$ and $N = 1$ respectively. The dashed line indicates the limiting value (102.3 meV/Å^2) to which the lower envelope of the family of curves tends.

(1) in the cases $N = 0$ and $N = 1$, for which we have performed both direct quench and annealing-quenching cycles, the differences in the

surface energy between the direct quenched and annealed samples are big, especially for the vicinals with higher inclination.

(2) If we compare only annealed samples, the differences in surface energy between the cases $N = 0$ and $N = 1$ are very small, particularly up to the vicinal with $K = 7$; in both cases there is a shallow minimum in correspondence with $K = 5$.

(3) In the case $N = 1$, there are two distinct minima in the surface energy in function of K: one for the annealed samples at $K = 11$, the other for the quenched samples at $K = 17$; the lower in energy is in correspondence with the (11,1,1).

(4) If we limit ourselves to examine only quenched samples for the three orders of reconstruction $N = 1, N = 2, N = 3$, each curve has a minimum in correspondence with $M_{min} \simeq 5N + R$ with $R \simeq 3$. We recall that $5N$ is the optimal periodicity in the reconstruction direction for the Au(100) flat case, varying the order of reconstruction. It is the presence of the steps, which shifts the position of the minima towards bigger cells, as it will be clear further.

(5) The lower envelope of the family of curves tends, for $K \rightarrow \infty$ to a limiting value $\sigma_0 = 102.3$ meV/Å^2, i.e., the surface energy of the flat reconstructed Au(100), as it is natural to expect, considering that the step contribution should vanish in the limit of infinite terraces. The lower envelope of the family corresponds to vicinal surfaces where the top layer atomic density is always kept around the optimal value (corresponding to keeping $M/N \simeq 5$).

5.2.1 The (3,1,1), (5,1,1) and (7,1,1) vicinals

For the smallest cells (i.e. vicinals with higher inclination) $K \leq 13$, we have tried several kinds of annealing schedules, differing substantially in the heating temperatures and in the cooling rates. The results for the $N = 0$ and $N = 1$ cases, corresponding to a non-reconstructed and a reconstructed (with extra atoms) starting point, are reported in Table 5.1.

It can be seen that, with a single exception, the surface energy for a given vicinal depends very weakly on the annealing schedule chosen, the differences being of the order of 1%. Somewhat unexpectedly, for (3,1,1), (5,1,1) and (7,1,1) the surface energy is nearly independent on the choice of the initial configuration ($N = 0$, $N = 1$). This fact will be discussed

Table 5.1:
Surface energies of the vicinals with highest inclination, using three different annealing schedules.

Structure N=0	*250 K-Anneal* σ *(meV/Å²)*	*300 K-Anneal* σ *(meV/Å²)*	*500 K-Anneal* σ *(meV/Å²)*
(3,1,1)		107.51	107.50
(5,1,1)		106.55	106.52
(7,1,1)		108.59	106.95
(11,1,1)		112.10	
Structure N=1			
(3,1,1)	113.72	107.50	108.40
(5,1,1)	106.55	107.70	107.31
(7,1,1)	107.91	107.92	107.91
(9,1,1)	105.05	105.04	105.05
(11,1,1)	104.31	105.58	104.31
(13,1,1)	104.77	104.54	104.53
(15,1,1)		104.38	
(17,1,1)		104.48	
(19,1,1)		104.72	
(23,1,1)		105.31	

below.

Table 5.2 reports the surface energies of several directly quenched vicinal surfaces. Comparison with Table 5.1 indicates that

(a) the surface energy for the case $N = 0$ is much higher in the quenched samples, indicating that extensive rearrangements of the atomic positions with respect to the initial state, unattainable by simple quench, are required to energetically optimize the surface;

(b) in the case $N = 1$, annealing still gives better results than quenching, but the difference is not so dramatic, and tends to vanish as the terrace length increases (see, for istance vicinals with $K > 13$). Visual examination

Table 5.2:
Quench results for several vicinals and different orders of reconstruction.

Structure	*N=0* $\sigma(meV/Å^2)$	*N=1* $\sigma(meV/Å^2)$	*N=2* $\sigma(meV/Å^2)$	*N=3* $\sigma(meV/Å^2)$
(3,1,1)	114.12			
(5,1,1)	122.88	123.59		
(7,1,1)	125.41	116.03	120.86	
(9,1,1)	126.51	108.79	118.91	125.67
(11,1,1)	126.98	106.14	113.73	122.60
(13,1,1)	127.44	104.77		118.90
(15,1,1)		104.76	109.08	
(17,1,1)		104.50	106.26	116.07
(19,1,1)		104.91	105.14	
(21,1,1)		104.93	104.52	
(23,1,1)		105.39	103.78	106.69
(25,1,1)			103.78	
(27,1,1)		106.40	103.95	104.61
(29,1,1)			104.24	104.12
(31,1,1)		106.52	104.04	103.93
(33,1,1)				103.35
(35,1,1)		106.82	104.56	103.47
(45,1,1)		107.58		103.87
(59,1,1)		108.42		

of the final states helps to understand the differences in energy in the case $N = 0$. As an example, Fig. 5.6 and Fig. 5.7 show respectively the structure of a $N = 0$ (5,1,1) vicinal for a quenched and an annealed sample. It can be seen that in the quenched case the square structure present in the initial configuration is perfectly retained. In the annealed samples, on the other hand, in spite of the lack of extra atoms, $[01\bar{1}]$ rows slide laterally and form a nearly-triangular reconstructed structure which has a much lower surface energy. In fact, the surface density is effectively higher in these configurations, since relaxations tend to flatten the steps, almost fully exposing to the surface atoms, which were previously covered by other atoms.

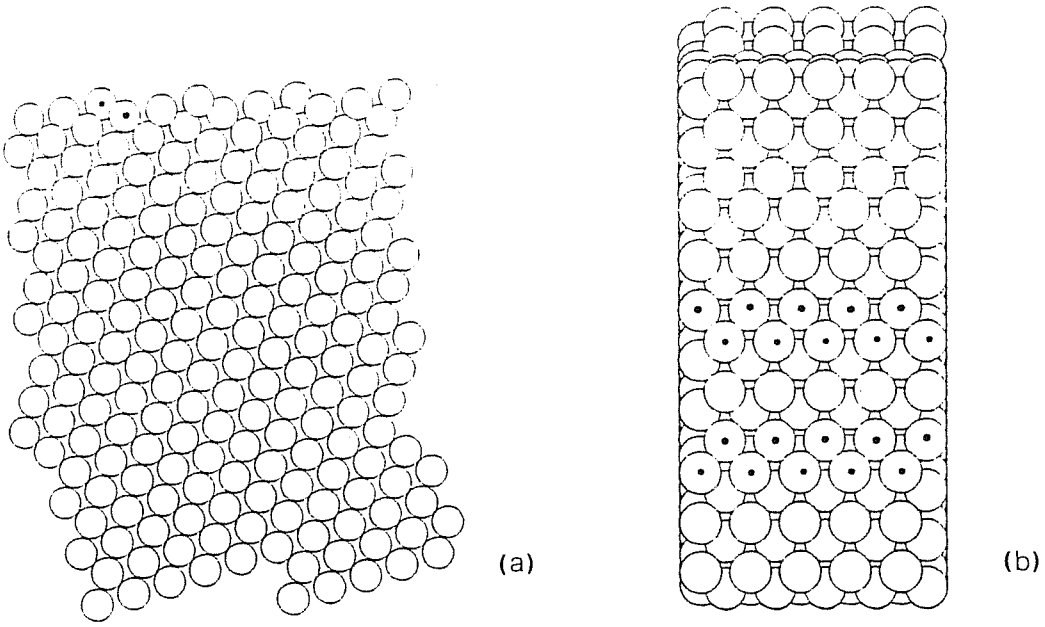

Figure 5.6:
(5,1,1) in the case $N = 0$. Quenched sample. Two MD boxes are shown in y' direction. For details see Fig. 5.2.
(a) Slab profile.
(b) Top view.

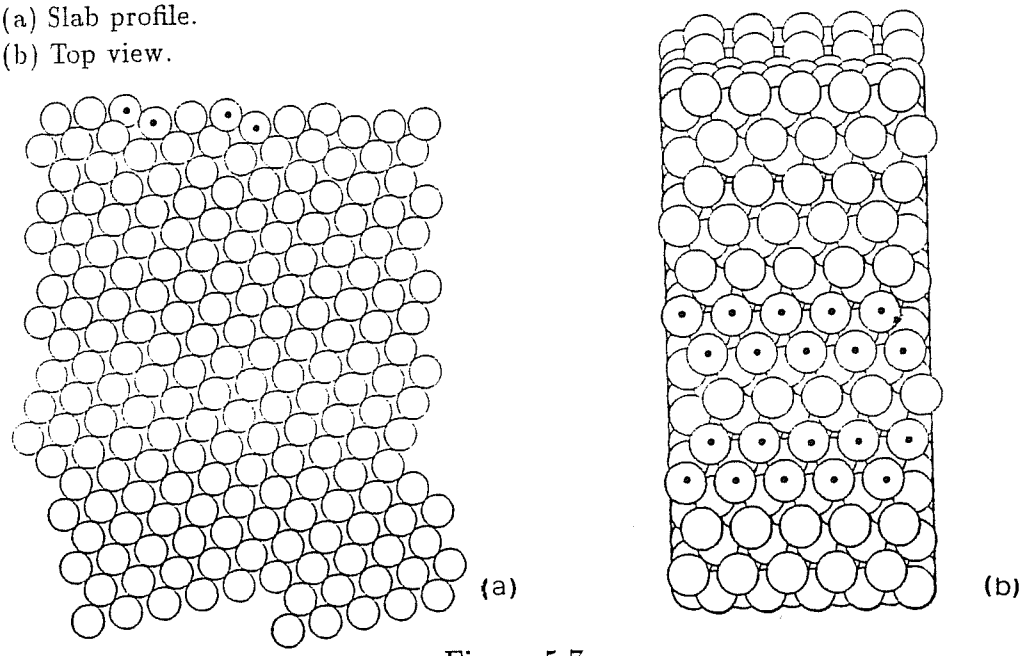

Figure 5.7:
(5,1,1) in the case $N = 0$. Annealed sample. Two MD boxes are shown in y' direction. For details see Fig. 5.2.
(a) Slab profile.
(b) Top view.

In the quenched stepped surfaces, whose terraces retain the initial square lattice structure, the surface energy *increases* as $\theta \to 0$, tending to 128.5 meV/Å^2, that is the value of the metastable state of the unreconstructed (100) flat surface (obtained by a careful quenching [14] of a perfect crystal). This peculiar behaviour seems to indicate that the square structure on a flat Au(100) is so much disfavoured so as to give a local surface energy higher than that found in the regions around the steps. This clearly anomalous and unrealistic situation changes drastically when thermal annealing takes place. Annealing, in fact, systematically destroys any square structure for the smallest cells up to $K = 7$.

Table 5.1 also shows that the surface energy of the (5,1,1) vicinal, 106.5 meV/Å^2 in the best case $N = 0$, is remarkably low, lying below that of the less inclined (7,1,1) and only 4% larger than that of the flat, reconstructed (100). This can be qualitatively understood by noting its very regular and well-packed quasi-triangular structure in Fig. 5.7 b. In particular, this high degree of packing is obtained by a relaxation mechanism (Fig. 5.7), where the atoms at the base of the step increase their distance (up to 13%) from the neighbouring atoms of the "bulk part" in the same (100) layer, this fully becoming part of the surface layer. At the same time, atoms at the top of the step strongly relax inward. This mechanism effectively rises the surface layer density, allowing the triangular reconstruction to take place by an alternate sliding of the $[1\bar{1}0]$ rows. Besides, this fact causes also the presence of a less sharp step, that is the step orientation is less tilted than in the unrelaxed case, with a consequent minor cost in the energy.

This might explain why this surface is found to be particularly stable in experiments, whereas (7,1,1) and (9,1,1) tend to facet into (5,1,1)+(100) [88].

Basically, the same relaxation pattern (for the $N = 0$ case) appears on the (7,1,1) surface (Fig. 5.8). In this case, however, the surface energy is higher in spite of the lower step density. Presumably, this is due to the lower degree of packing which can obtained, since the terraces are longer (4-instead of 3-atoms wide). A better packing is obtained in the case $N = 1$, where the starting point consists of terraces already reconstructed by the insertion of an extra row. However, terraces on (7,1,1) are not long enough to make this configuration particularly convenient, as insertion of the extra atom causes an *excessive* amount of packing. In other words, the (7,1,1) terraces length fits badly with the reconstruction periodicity. The situation

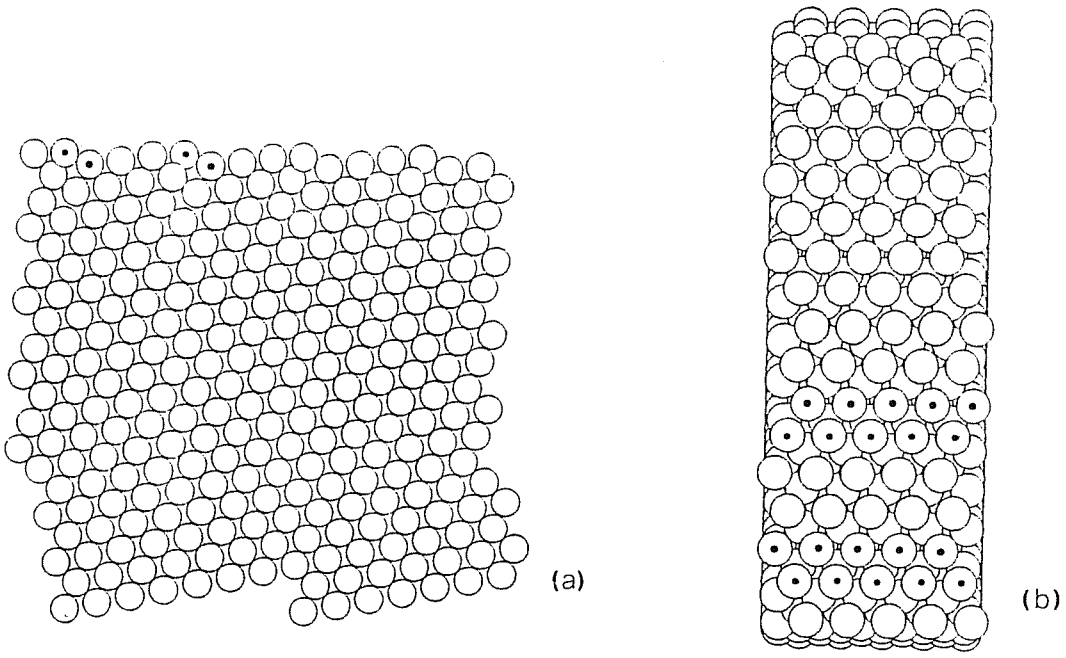

Figure 5.8:
(7,1,1) in the case $N = 0$. Annealed sample. Two MD boxes are shown in y' direction. For details see Fig. 5.2.
(a) Slab profile.
(b) Top view.

changes with (9,1,1) and (11,1,1), where the $N = 1$ case is clearly favoured (see Table 5.1).

Before proceeding to analyse larger cells, let us note that annealed (3,1,1), (5,1,1) and (7,1,1) have almost the same energy in the $N = 0$ and $N = 1$ cases, perfectly the same for the vicinal (3,1,1). While this can be understood for (7,1,1) in terms of the previous discussion, it seems rather surprising for (3,1,1) and (5,1,1), where compression should be enormously large in the $N = 1$ cases.

However, the final configuration after the annealing procedure looks very similar; it can be seen, for instance, comparing Fig. 5.9 with Fig. 5.7, and observing also Fig. 5.10, where the final configuration of (3,1,1) in the case $N = 0$ is reported, which is almost undistinguishable from the case $N = 1$, according to the nearly equal to zero differences in the surface energy.

The final effect of the extra atoms is simply that of increasing slightly the slab thickness. This confirms the substantial correctness of the structure found by simulated annealing, since the same structure is obtained by starting from two very different initial states.

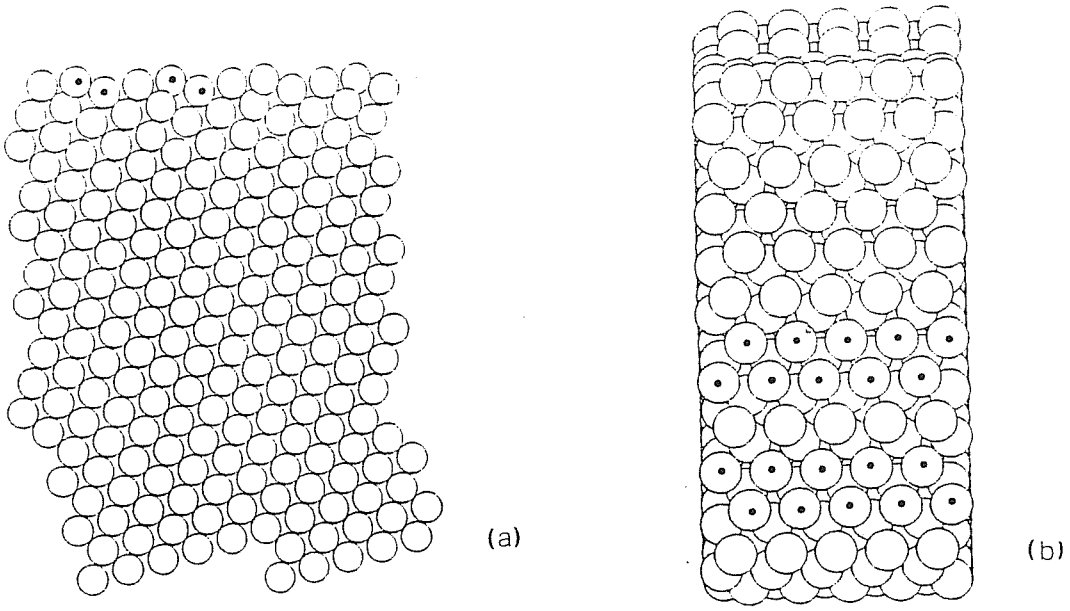

Figure 5.9:
(5,1,1) in the case $N = 1$. Annealed sample. Two MD boxes are shown in y' direction. For details see Fig. 5.2.
(a) Slab profile.
(b) Top view.

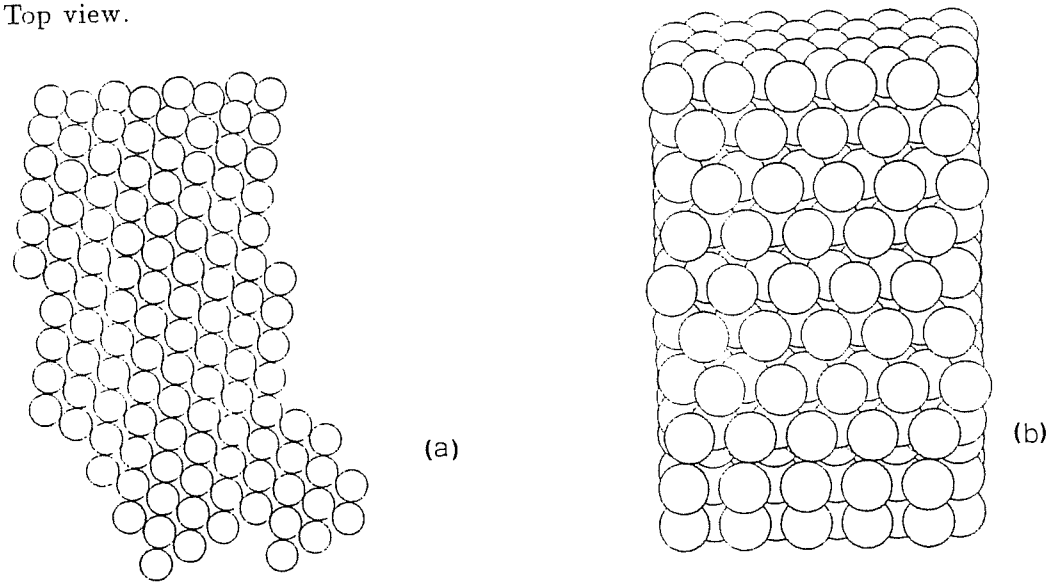

Figure 5.10:
(3,1,1) in the case $N = 1$. Annealed sample. Two MD boxes are shown in y' direction. For details see Fig. 5.2.
(a) Slab profile.
(b) Top view.

5.2.2 Sharp and smooth steps

Let us now proceed by analysing larger cells, in particular the (9,1,1) vicinal. This surface has 5-rows wide terraces, and therefore it seems ideally suited to accommodate on each row a (1×5)-like, 6-over-5 reconstructed structure. This is what indeed occurs. However, the final configuration is strongly dependent on the optimization strategy adopted (annealing or quenching). While for the simple quenched configuration (Fig. 5.11) we have a (1×5) smooth structure with stacking resembling the $ABCCBA$, found on flat (100) surface [12,13], the structure of the annealed slab (Fig. 5.12), is characterized by a strongly asymmetric disposition of the atoms in the first layers, with those in the fifth position having higher z-coordinate than the others, giving rise to a sharp step.

The origin of this difference can be better understood, by observing the trend of the energy per atom and of the coordination for the atoms on the terrace; for the annealed sample the atoms in fifth position have a big maximum in the energy (and consequently a deep minimum in the coordination), while for the directly quenched sample there are no sharp peaks, but rather a regular increase, except for a little minimum for the atoms in fifth position up to the end of the terrace. Anyhow, the sharp step structure is energetically slightly favoured because for the atoms in third and fourth positions the energy is much lower, as it is seen in Fig. 5.13. The opposite trend is found, naturally, in the coordination, with deep minima in correspondence with high maxima of energy and vice versa (Fig. 5.14).

The same differences are well evident in the (7,1,1), (11,1,1) and (13,1,1) vicinals too. For istance, for (11,1,1) two different annealings give different results for the surface energy (see Table 5.1), just for the reason that in one case the structure is much more asymmetric, with the characteristic sharp point (Fig. 5.15), than in the other case, which results similar to the directly quenched sample (Fig. 5.16)

Sharp step structures are also sometimes observed on (13,1,1), while only smooth step structures are found for larger cells. For example, Fig. 5.17 and Fig. 5.18 show that similar smooth-step structures are obtained by quenching and annealing for (17,1,1), with only a small stacking difference.

We can summarize the results for the vicinals in the interval (7,1,1) - (13,1,1) in the following Table 5.3:

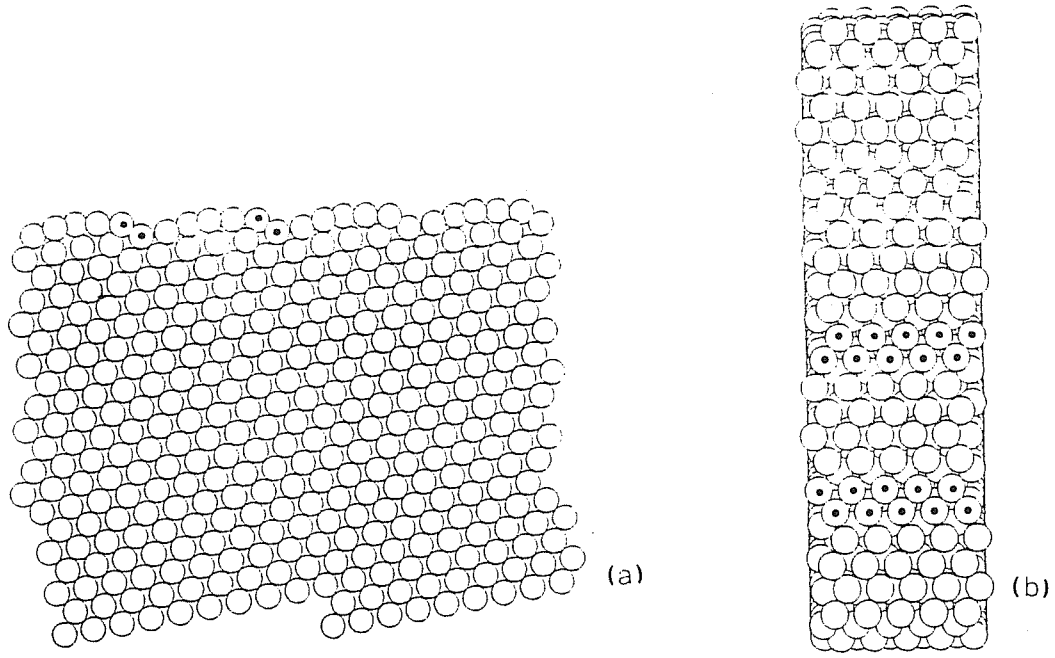

Figure 5.11:
(9,1,1) in the case $N = 1$. Quenched sample. Two MD boxes are shown in y' direction. For details see Fig. 5.2.
(a) Slab profile.
(b) Top view.

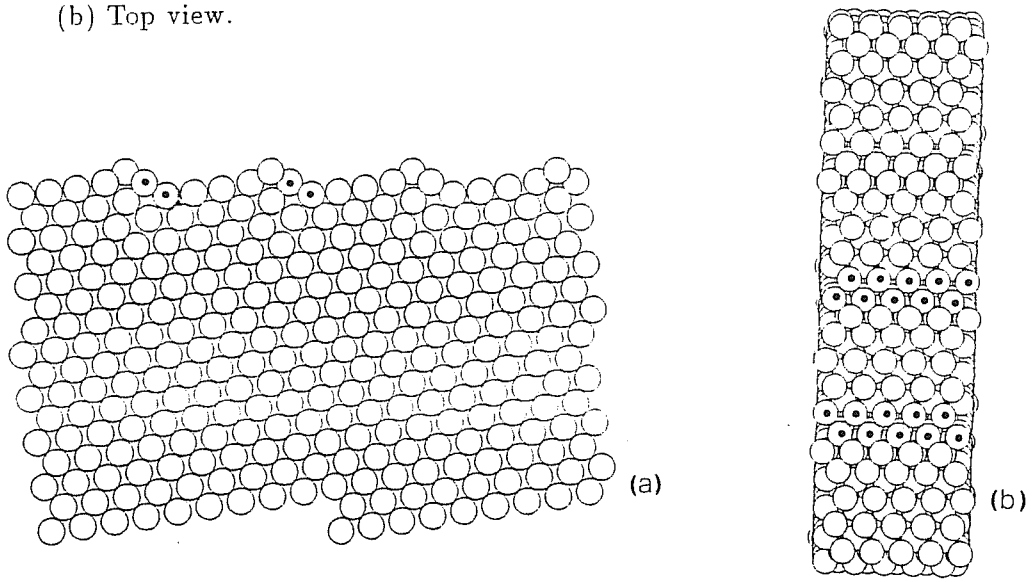

Figure 5.12:
(9,1,1) in the case $N = 1$. Quenched sample. Two MD boxes are shown in y' direction. For details see Fig. 5.2.
(a) Slab profile.
(b) Top view.

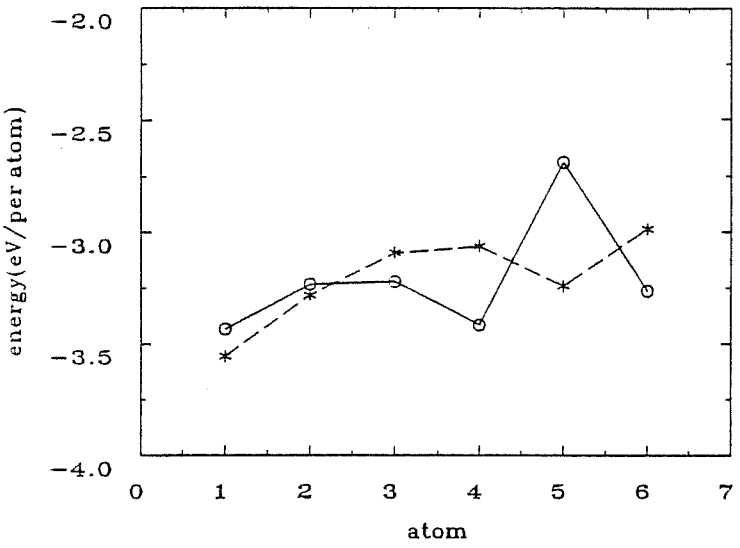

Figure 5.13:
The energy per atom for the 6 atoms in a row in the y' direction on the topmost layer for the annealed and quenched (9,1,1) samples. o refers to the annealed sample and $*$ to the quenched one.

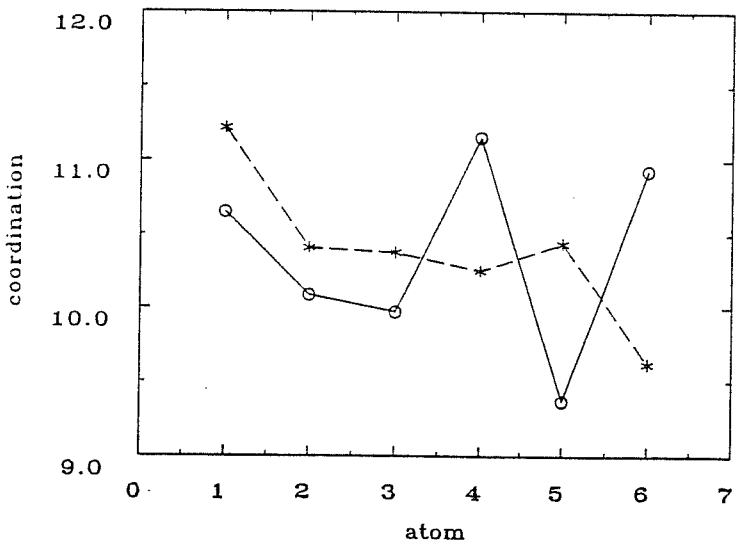

Figure 5.14:
Coordination per atom for the 6 atoms on a row in the y' direction on the topmost layer for the annealed and quenched (9,1,1) samples. o refers to the annealed sample and $*$ to the quenched one.

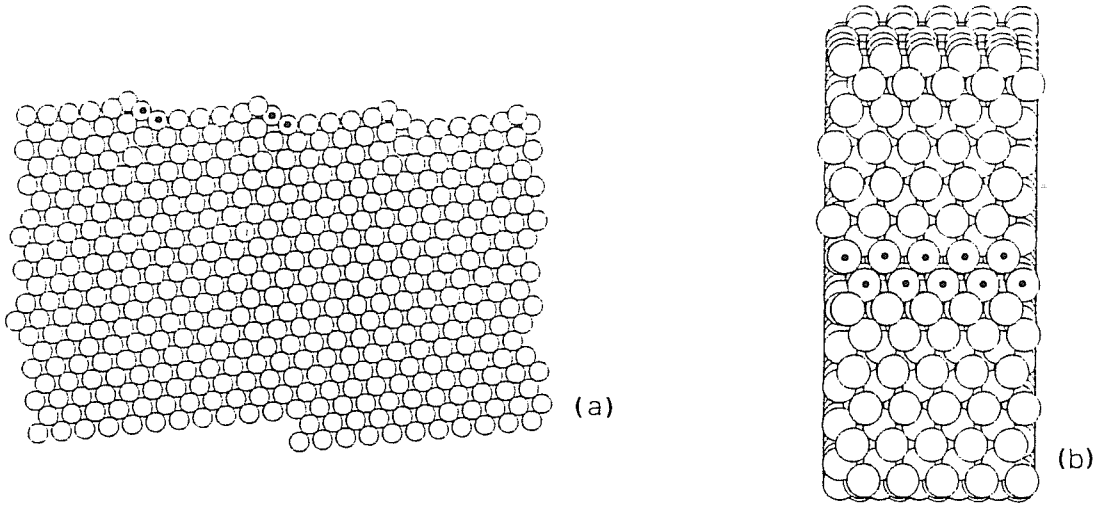

Figure 5.15:
(11,1,1) in the case $N = 1$. Annealed sample. For details see Fig. 5.2.
(a) Slab profile. Two MD boxes are shown in y' direction.
(b) Top view.

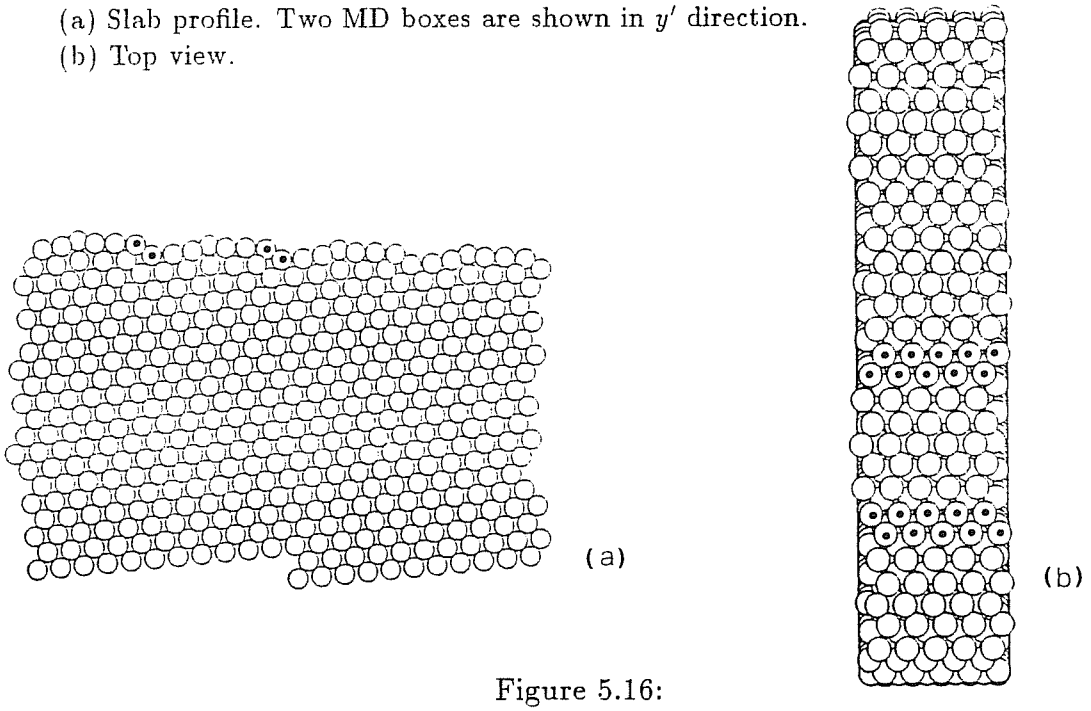

Figure 5.16:
(11,1,1) in the case $N = 1$. Quenched sample. Two MD boxes are shown in y' direction. For details see Fig. 5.2.
(a) Slab profile.
(b) Top view.

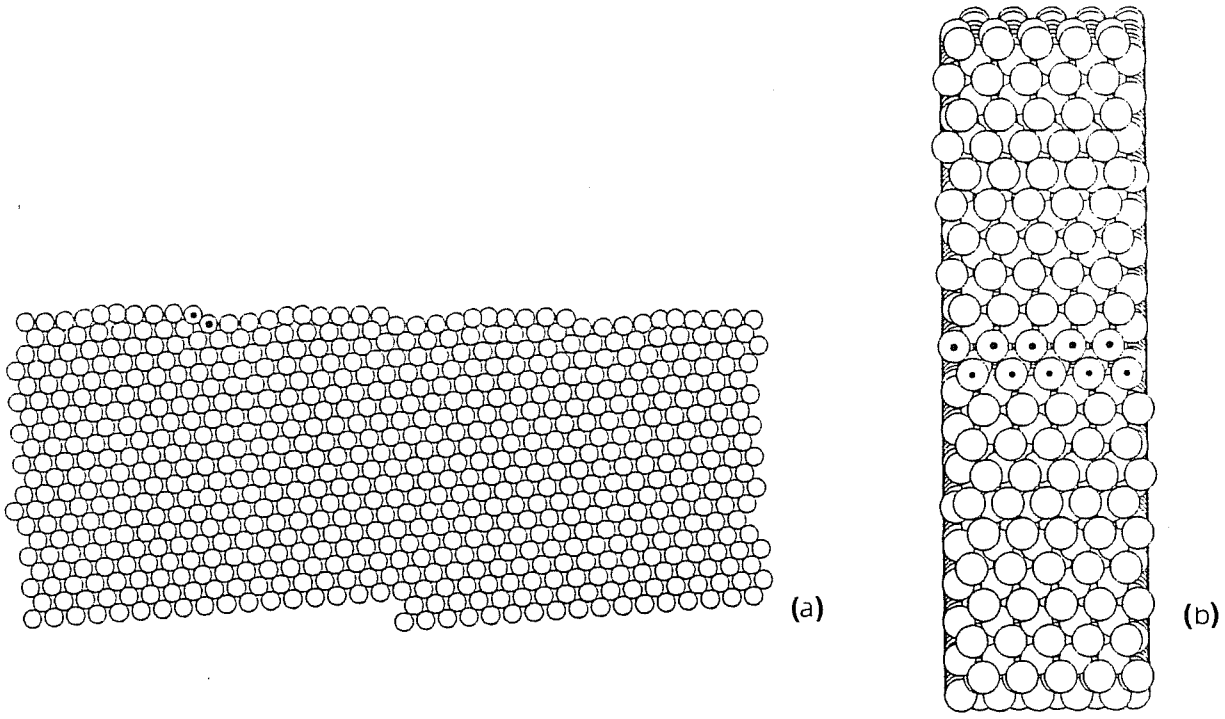

Figure 5.17:
(17,1,1) in the case $N = 1$. Quenched sample. For details see Fig. 5.2.
(a) Slab profile. Two MD boxes are shown in y' direction.
(b) Flat map.

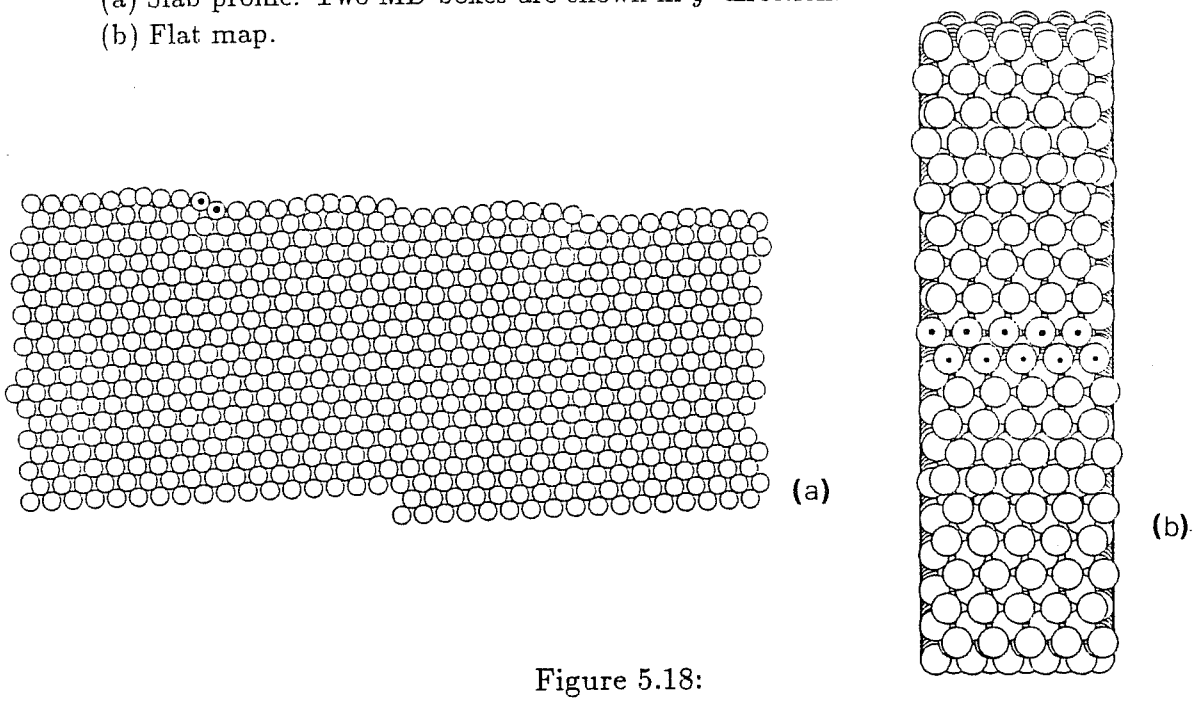

Figure 5.18:
(17,1,1) in the case $N = 1$. Annealed sample. For details see Fig. 5.2.
(a) Slab profile. Two MD boxes are shown in y' direction.
(b) Flat map.

Structure	Sharp step	Smooth step
(7,1,1)	107.92	116.03 *
(9,1,1)	105.04	108.79 *
(11,1,1)	104.31	105.58
(13,1,1)	104.54	104.53

Table 5.3:
Surface energies of $N = 1$ vicinal surfaces in the sharp step and smooth step configurations. All values are obtained by simulated annealing, except those marked with a $*$, obtained from quenching.

Among the vicinals, for which it is possible to distinguish well the two configurations, the sharp and the smooth step structures, the sharp step structure implies a big energetic gain with respect to the other, especially for vicinals with highest inclination (8.1 meV/Å^2 for (7,1,1) and 3.8 meV/Å^2 for (9,1,1)). However this difference decreases for increasing K, until at $K = 13$ (8-onto-7 atom terraces) the smooth step structure is more convenient (-0.01 meV/Å^2).

We can qualitatively affirm that, when the system is too much under compression, as it happens in reconstructed small size vicinals, the sharp point structure has lower energy, because the stress can concentrate especially in the sharp point, keeping the other parts of the terrace less stressed. Instead, when the terrace is longer and so less stressed for the reconstruction, the sharp step structure is not more convenient.

The sharp step configuration has a minimum at (11,1,1) (7-onto-6 atoms terraces), while for the smooth step configuration the minimum is in correspondence with the vicinal (17,1,1) (10-onto-9 atoms terraces). Between these two local minima, the lowest in energy is that corresponding to the vicinal (11,1,1). This fact compares well with the experimental results by Hasegawa et al.[38], who also obtained as the best vicinal the (11,1,1).

But our structure of the 7 onto 6 terraces (Fig. 5.15), with its asymmetry above described is, however, a little different from that shown in Profile Imaging micrographs [38], which seems to have a corrugation just

in the middle of the terrace (see Section 4.5), more similar to our quenched configurations.

If, on this annealed sample, we consider (100) tilted layers within a single MD box, the first one of these layers (Fig. 5.15) shows an area with an inward relaxation, followed by a very little one (two atoms wide), in which there is a strong corrugation (0.8 Å) and finally another region with inward relaxations.

This relaxation pattern propagates until deeper layers. Anyhow, if we consider the average z coordinates (in (100) direction) we can say that the distance between the first and the second layer, in average, slightly increases, similarly to what happens between the second and the third, and finally that between the third and the fourth again decreases.

The average relaxation of the first layer respect to the second one is quite close to that obtained [13,12,14] with the (1×5) cell, on flat surface, and also the behaviour of the relaxation of the deeper (100) layers is qualitative similar to that obtained in the flat case (see Section 2.2).

The results got from simple quenching in the orders of reconstruction $N = 2$ and $N = 3$ give as the best configurations the vicinals (25,1,1) (Fig. 5.19) and (33,1,1) (Fig. 5.20) corresponding to 15 onto 13 and 20 onto 17 atoms terraces.

As it is natural to expect, we observe in the (25,1,1) and (33,1,1) respectively, two and three symmetric configurations $ABCCBA$, i. e., for each atom added a configuration $(1 \times p)$ appears, with $p \simeq 5$.

5.2.3 A model for surface energies of quenched samples

While for the smallest cells (up to K=13), it is not possible to find a simple analytical expression for the surface energies of the annealed samples, which fits our MD results, instead, a very simple model can reproduce the trend of the quench results for $N \geq 1$.

As it will be clear further, we have adopted the solution of considering the physical situation described by this model for the orders of reconstruction $N > 1$, while for $N = 0$ and $N = 1$ the physical conclusions are done on the MD points.

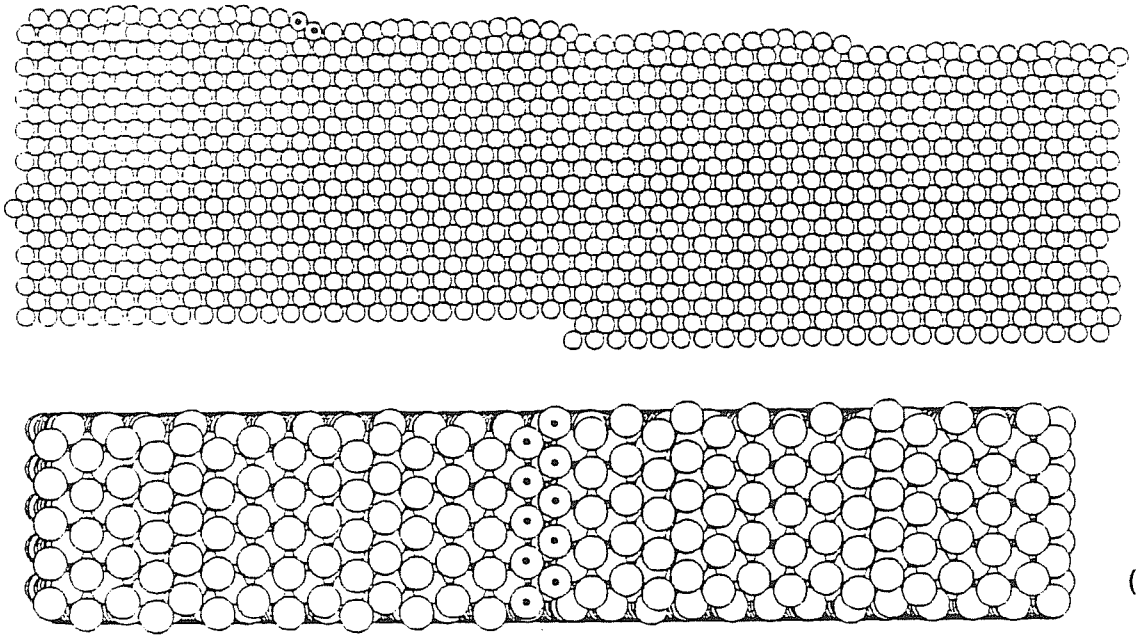

Figure 5.19:
(25,1,1) for the case $N = 2$. Annealed sample. For details see Fig. 5.2.
(a) Slab profile. Two MD boxes are shown in y' direction.
(b) Top view.

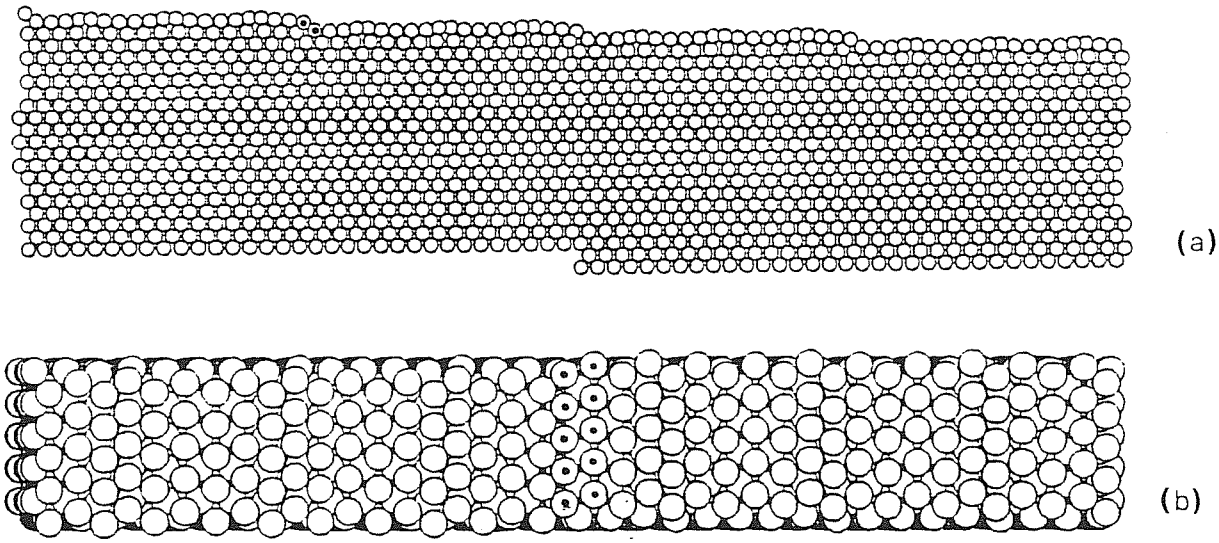

Figure 5.20:
(33,1,1) for the case $N = 3$. Quenched sample.
(a) Slab profile. Two MD boxes are shown in y' direction.
(b) Top view.

The simple model consists of separating the surface energy in a terrace and in a step contribution:

$$\sigma(M,N) = \sigma_{terrace}(M,N) + \sigma_{step}(M,N). \tag{5.2}$$

In this splitting, the terrace is regarded as a piece of flat, reconstructed (100), while effects associated with relaxations near the steps are thought to be incorporated into the step term. For flat $(1 \times M)$-reconstructed (100), it turns out that the behaviour of the surface energy as a function of the cell length M, for $M = 3, ..., 7$, as extracted from a previous study, using the same model [12], can be well reproduced by a quadratic expression in $1/M$

$$\sigma_{flat}\left(\frac{1}{M}\right) = a + b\left(\frac{1}{M}\right) + c\left(\frac{1}{M}\right)^2 \tag{5.3}$$

with $a = 117.88$ meV/Å^2, $b = -155.75$ meV/Å^2, $c = 389.38$ meV/Å^2. With this choice of the coefficients, this expression has a minimum for $M = 5$, exactly corresponding to the value 102.3 meV/Å^2, found by energy minimization [12].

We can regard the independent variable $1/M = (M+1)/M - M/M$ as the average excess atom density (due to reconstruction) per unit area. On a terrace with length M and reconstruction of order N, the excess density is $(M+N)/M - M/M = N/M$.

We are thus led to write, for the "flat terrace contribution" to the surface energy,

$$\sigma_{terrace}(M,N) = \sigma_{flat}\left(\frac{N}{M}\right) = a + b\left(\frac{N}{M}\right) + c\left(\frac{N}{M}\right)^2. \tag{5.4}$$

For $N = 1, 2, 3...$, this expression has a minimum for $M = 5, 10, 15....$ However, MD results indicate that the minima of the terrace part are rather located near M=10,13,17..., that is terraces prefer to be larger than what predicted by Eq.(5.4).

We may tentatively explain this discrepancy by noting that, at the terrace side, near the base of a step, atomic coordination is relatively high. Therefore, for the arguments discussed in Chapter 1, the tendency to reconstruct should be weaker in this region. Schematically, we may then divide the total terrace length $M_N d$ of the optimal terrace with the reconstruction

order N, in two parts:

$$M_N d = \lambda d + (M_N + N - \lambda)\frac{5}{6}d, \tag{5.5}$$

where d is the bulk spacing between rows, λ indicates the number of non-reconstructed rows near the step base, while the remaining $M+N-\lambda$ rows in the terrace are assumed to be reconstructed, and therefore optimally separated on the average by $(5/6)d$. This condition yields $M_N = 5N + \lambda$, predicting a shift of the minima.

In this scheme, the surface energy of a generic terrace can also be divided in two parts, weighted by the area fractions occupied by the two regions:

$$\sigma_{terrace}(M,N) = \frac{\lambda}{M}\sigma^{*} + \left(1 - \frac{\lambda}{M}\right)\ \sigma_{flat}\left(\frac{N}{M-\lambda}\right), \tag{5.6}$$

where σ^{*} is the surface energy to be associated with the region near the step base, and σ_{flat} is the expression (5.3). The argument $N/(M-\lambda)$ is the excess density, due to $M+N-\lambda$ rows stacked above $M-\lambda$.

σ^{*} is unknown, but note that the term $\frac{\lambda}{M}\ \sigma^{*}$ is proportional to the step density and can be very naturally incorporated into the steps contribution to the surface energy discussed below. Therefore, we shall simply drop this term from (5.6). λ has to be regarded as a free parameter to be fitted.

Of course, the real situation is more complex than this scheme, as revealed by inspection of the quenched configurations. The inter-row spacing, in fact, changes gradually rather than abruptly, so that one cannot in practice identify a boundary between two different regions. However, the argument is valid and (5.6) reasonably fits the results.

To ultimate the description of the various contributions to the surface energy, we must analyse the step term in (5.2). We can schematize the energy per unit length (in the direction of the steps, i.e. x direction) of a system of p interacting steps, with terrace length Md onto a distance $L = pMd$ with the expression

$$E_{step} = \frac{E}{L_x} = p\epsilon + \frac{h}{(Md)^2}; \tag{5.7}$$

ϵ is the energetic cost of the step, h is the strength of the step-step interaction, which depends from the square of the distance between two steps, as

it is explained in Chapter 4. The contribution of the steps to the surface energy is given naturally by E_{step}/L:

$$\sigma_{step} = \frac{\epsilon}{Md} + \frac{h}{(Md)^3} \tag{5.8}$$

or

$$\sigma_{step} = \frac{\mu}{M} + \frac{g}{M^3}. \tag{5.9}$$

μ is naturally interpretable as the chemical potential of the steps. In our simple scheme, we take σ_{step} independent from the order of reconstruction. We recall that the interaction is generally repulsive ($g > 0$), due to the lattice strain in the vicinity of a step.

To fit our MD results to the full expression (5.2), we have proceeded as follows:

(1) we assume that $\sigma(M,N)$ tends to the optimal value $\sigma_0 = 102.3$ meV/Å^2 for flat (100) when the vicinal angle $\theta \to 0$, i.e., $M \to \infty$, but also $N \to \infty$ with M/N=5 to retain the correct excess density:

$$\lim_{M\to\infty} \sigma\left(M, \frac{M}{5}\right) = \sigma_{flat}\left(\frac{1}{5}\right) \equiv \sigma_0; \tag{5.10}$$

(2) all the minima in the family of surface energy curves corresponding to different values of N are obtained by replacing $\sigma_{flat}\left(\frac{N}{M-\lambda}\right)$ with the optimal value σ_0 in (5.6). From (5.6) and (5.9), it follows that these minima satisfy the equation

$$\sigma_{min}(M) = \sigma_0 + \frac{f - \lambda\sigma_0}{M} + \frac{g}{M^3}. \tag{5.11}$$

From our MD results, we can identify the values of M corresponding to the minima of the surface energy for $N = 2, 3$, corresponding, respectively, to $M = 13$ and $M = 17$. These two points, when surface energies are plotted as a function of $1/M$, appear to be perfectly lined with the point ($1/M$=0, $\sigma = \sigma_0$). This allows to estimate $\mu = f - \lambda\sigma_0 \simeq 17$ meV/Å^2. This value may be regarded as the "step chemical potential". The effect of the step interaction cannot be noticed on these terrace sizes.

(3) We subtract the minimum energy $\sigma_{min}(M)$ thus determined for all $M's$ from our data for $N = 2$ and $N = 3$. The resulting locations of the minima allow us to estimate $\lambda \simeq 2.6$. At this point (5.6) can be used to estimate $\sigma_{terrace}(M,N)$ for all M and N.

(4) We calculate the analytic curve for $N = 1$. This is quite different from the actual MD results, particularly for small M, due to the smooth-sharp step bistability discussed above, which is not taken into account by the present model. A better agreement is obtained by assigning a finite value to the step interaction. Our estimate, $g \simeq 45$ meV/Å^2, shifts the energy of the $N = 1$ minimum ($M = 7.6$) by 0.1 meV/Å^2; the shift is negligible for $N \geq 2$. Note, however, that this estimate is extremely sensitive to the choice of parameters. The curves obtained by this procedure are shown in Fig. 5.21, compared with the quench results, in Fig. 5.22.

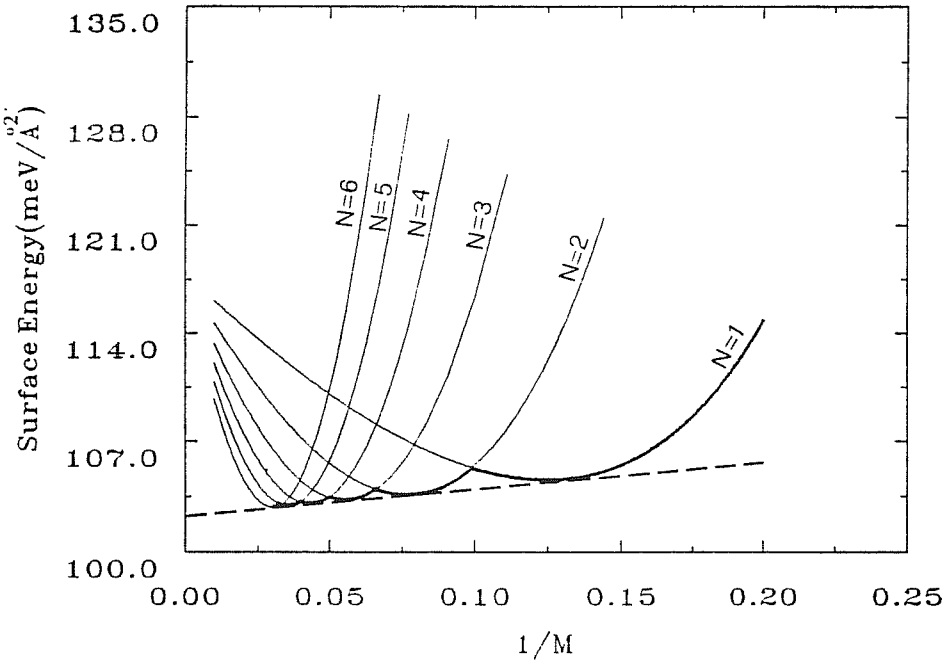

Figure 5.21:
Surface energy curves for the various orders of reconstruction N versus the step density $1/M$, as predicted by the Eq.(5.6) and Eq.(5.9). The slope of the dashed line (which starts from the value of the surface energy of the flat reconstructed Au(100)[13]) equals the chemical potential of the steps. The thick line, which indicates the lower envelope of the curves, defines the effective vicinal surface energy.

The thick line in Fig. 5.21 indicates the lower envelope, which defines the effective vicinal surface energy. The dashed line indicates the linear

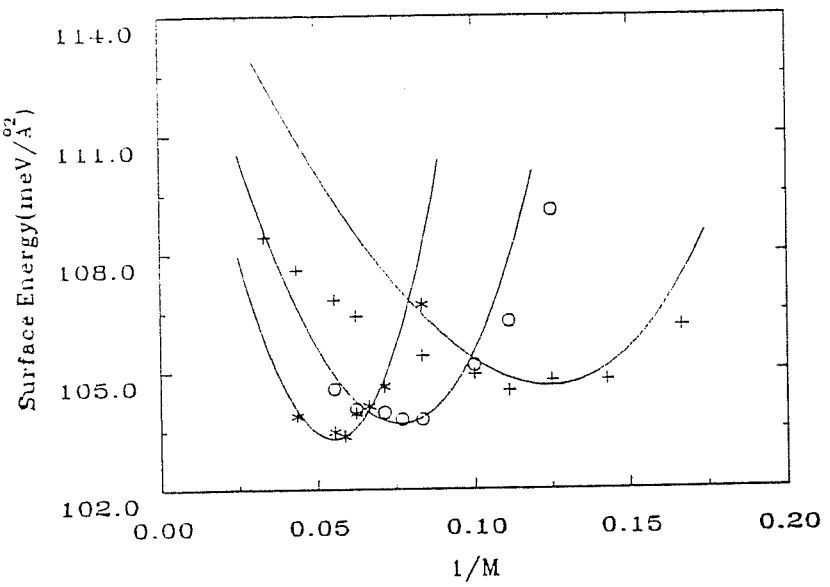

Figure 5.22:
Comparison between the quench-results (+ for $N = 1$, o for $N = 2$, and $*$ for $N = 3$) and the fitted curves.

term in $1/M$, whose slope is $\mu \simeq 17$ meV/Å^2, giving rise to an energy per unit length of the step $\epsilon = \mu d \simeq 50$ meV/Å.

The positions of the minima, which lie on the lower envelope of the curves, are described by the relation $M_{min} \simeq 5N + \lambda$, that is the size of the optimal terrace is not simply a multiple of 5, for the reasons above explained.

To our knowledge there are no experimental results on gold vicinals about the strength of the chemical potential and of the step-step interaction term, that can be compared with our calculations. Only for vicinal copper faces, however, some estimates by thermal roughening studies have been given [106] for the kink formation energy and the step-step interaction-energy, as explained in Section 4.5.

While the analytic expression introduced is a useful model for the high-index surfaces (which are expensive to optimize by computer), lower index surfaces are better taken into account by directly using the energy minimization results. In this sense, we have summarized the energetic informations into the graph of Fig. 5.23 where for $N \geq 2$ the surface energy of Au(100) vicinals has been considered described by the fitted analytical curves (Eqs.(5.6) and (5.9)), while for $N = 0$ and $N = 1$ we have limited ourselves to consider their MD values.

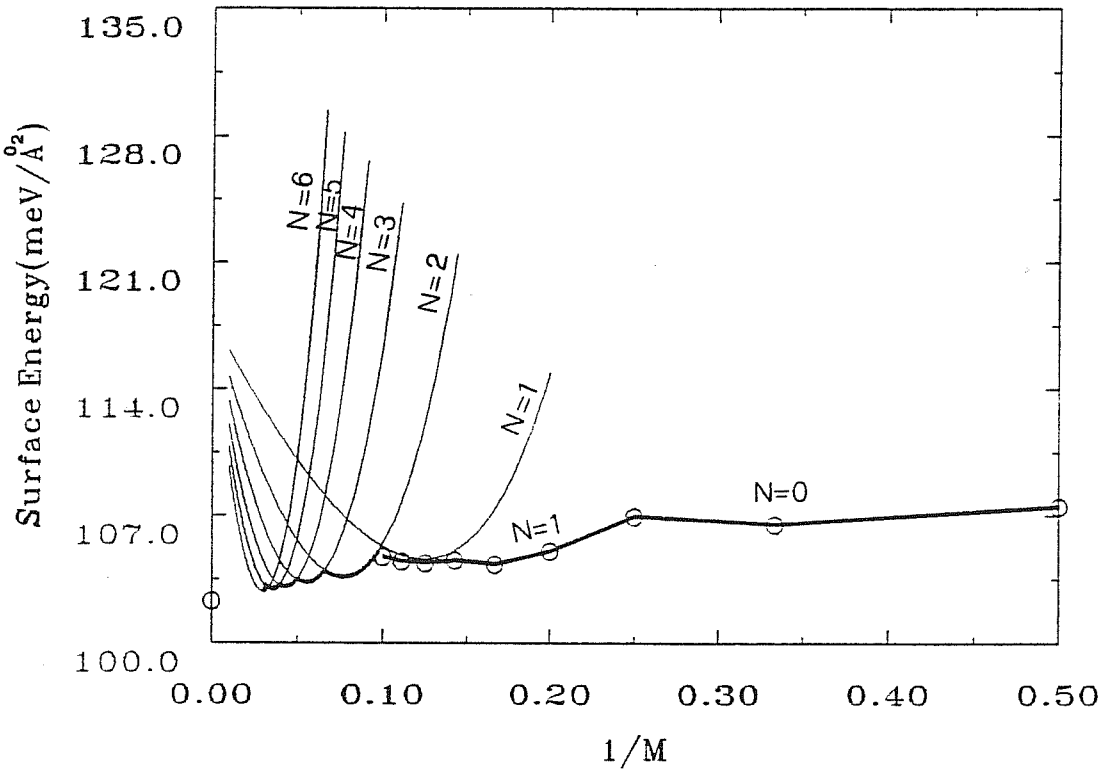

Figure 5.23:
o indicate the best simulated annealing results for the vicinals of high inclination ($N = 0, N = 1$), while the other curves represent the surface energies for the various orders of reconstruction, obtained by the analytical expressions (5.6) and (5.9). The thick line defines the effective vicinal surface energy. The dot on the ordinate axis indicates the flat reconstructed Au(100) surface energy in our model [12,13].

5.3 "Stabilized" (K,1,1) Au(100)-vicinals

5.3.1 The "tilting" pressure.

Introducing an external field (a "tilting pressure" π in this case), we have searched the minima of the "Gibbs surface free energy" in function of the angle θ, $g(\theta) = f(\theta) - \pi\theta$ by a Maxwell construction, that is we

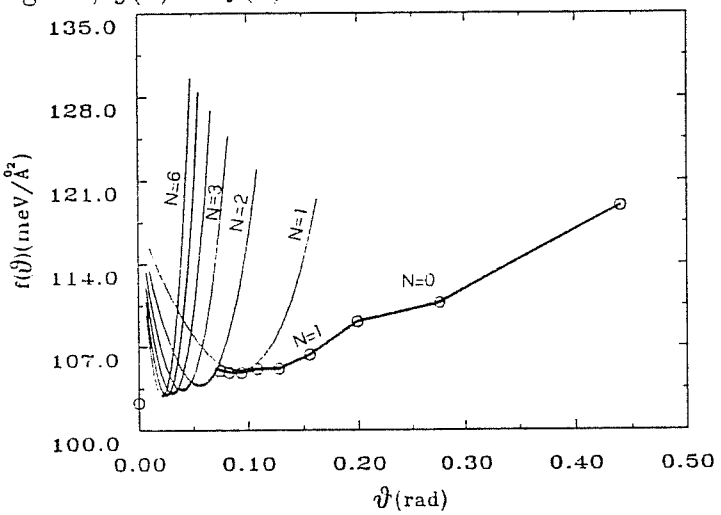

Figure 5.24:
The same as Fig. 5.23, but with $f(\theta) = \frac{\sigma(\theta)}{\cos\theta}$ versus the angle θ.

have looked first of all for the first intersection between the straight line $\sigma_o + \pi\theta$ (σ_o is the value of the surface energy of the flat reconstructed Au(100) surface) and the lower envelope of the curves $f(\theta) = \sigma(\theta)/\cos\theta$, which defines the effective vicinal surface energy (see Fig. 5.24). We divide $\sigma(\theta)$ by $\cos\theta$ because we want to take into account the increment of surface due to the inclination, respect to the low-Miller index direction (100). By considering $f(\theta)$ instead of $\sigma(\theta)$, we regard $\pi\Delta\theta$ as the energy required to increase the tilting angle from θ to $\theta + \Delta\theta$ by inserting extra steps, by leaving unchanged the total (100) area of the terraces, that is the projection of the area of the vicinal in the plane perpendicular to (100) direction.

Only starting from a certain value of the tilting pressure, we get these intersections. The value of π_{min} is naturally linked to the slope of the straight line tangent to the lower envelope of the curves of surface energy for the various reconstructions (that is linked to the value of the chemical

potential of the steps). Physically it means that only when we apply an external tilting pressure at least equal to the chemical potential of the steps, we can have stabilized vicinal surfaces.

As soon we have got the first intersection, corresponding to a certain value of σ, say σ_1, we start again from this point (θ_1,$\sigma_1/\cos\theta_1$) to perform the Maxwell construction. So, with a pressure π', we meet the curve in another point, say (θ_2, $\sigma_2/\cos\theta_2$), that is we apply again the relation

$$\sigma_1/\cos\theta_1 + \pi'(\theta_2 - \theta_1) = \sigma_2/\cos\theta_2 \tag{5.12}$$

and so on, until we cross the vicinals with the lowest Miller indices, corresponding to the order of reconstruction $N = 1$.

Because of the particular shape of surface energy obtained for cells of small size (Fig. 5.23), if we perform the Maxwell construction, we see that all high Miller index vicinals are not stabilized; in fact, the above described straight line $\sigma_o + \pi\theta$ meets, as the first vicinal, the (11,1,1).

Then, starting from $\sigma(\theta)/\cos\theta$, corresponding to the (11,1,1) vicinal, the second intersection corresponds to the (5,1,1) vicinal, and, at the end, the (3,1,1) vicinal is met. The results for $\pi(\theta)$ are shown in Fig. 5.25.

5.3.2 The Wulff plot

To discuss the stability of the Au(100) vicinal surfaces inclined along the [01$\bar{1}$] zone-axis, and in particular the tendency to formation of facets ("hill and valley" structure) we could have some informations from the Wulff plot. Here the vicinals cover the range between the (100) direction ($M \to \infty$) and the (111) ($K = 1$, $\theta \simeq 55^o$).

The magic vicinals, found for Au(100), have no impact on the macroscopic crystal habit. In fact, a crystal will grow a given facet if

(a) it corresponds to a surface energy cusp in the polar Wulff plot;

(b) that cusp is deep enough to prevail on other neighbouring cusps (see Chapter 4).

In our case, the magic vicinals can be thought as cusps, but they are not deep enough, respect to those corresponding to (100) and (111) cusps, to give rise to stable facets in the macroscopic crystal habit (see Fig. 5.26). The equilibrium crystal shape, at $T = 0$ can be thought as composed of (100) and (111) facets divided by sharp edges.

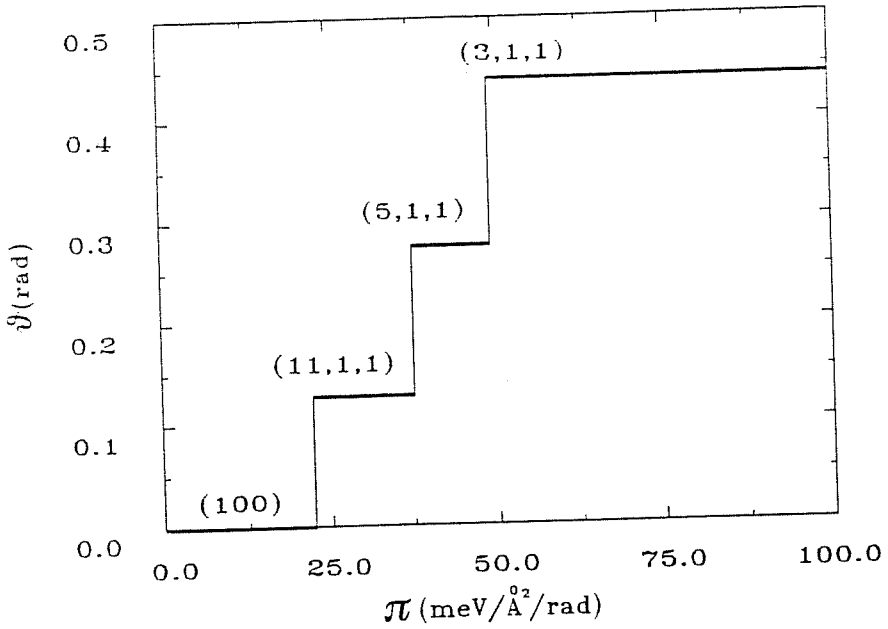

Figure 5.25:
The "tilting" angle versus the "tilting pressure". Note the magic vicinals (5,1,1) and (11,1,1).

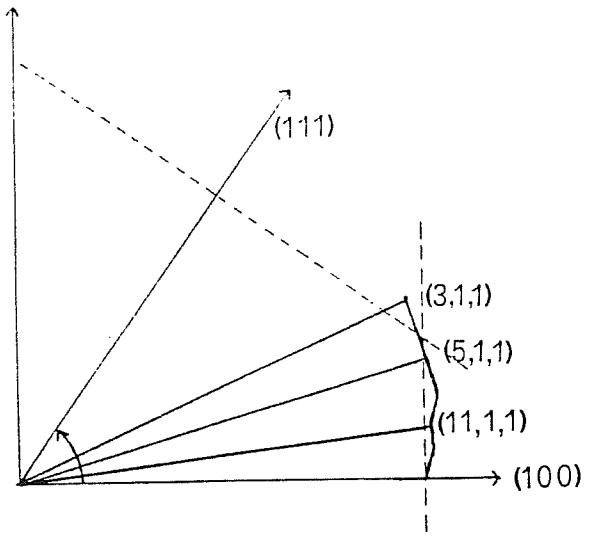

Figure 5.26:
The section of the Wulff plot corresponding to the inclination angles of the (K,1,1) studied vicinals, between the (100) and (111) direction. The dashed lines correspond to the two (100) and (111) facets, which constitute the equilibrium crystal shape. Note that the "magic vicinals" have no impact on the equilibrium crystal shape.

5.3.3 The faceting of (K,1,1) Au(100)-vicinals

Besides by the Wulff plot, we have tried to investigate which vicinals are stable and which facet, following the experimental suggestion by Sotto et al. [88], for which the (5,1,1) and all vicinals with K$\geq$ 11 are stable, while the (7,1,1) and (9,1,1) show a faceting in (5,1,1) and (100) facets.

To this end we have compared the energy of a configuration, in which in a macroscopic length L there are p terraces all of the same size $M(L = pM)$, which individuate a vicinal (K,1,1) with $K = 2M - 1$, with all the other possible configurations, in which the sizes M_i of the p terraces can be different among them, respecting, however, the condition

$$\sum_{i=1}^{p} M_i = pM, \tag{5.13}$$

which imposes the macroscopic tilting angles to remain unchanged. It is natural that we achieve the macroscopic limit when p goes to infinity.

The energy of a faceted configuration is naturally

$$\Sigma_f(M_1, ..., M_p) = \sigma(M_1)\frac{M_1}{\cos\theta_1} + ... + \sigma(M_p)\frac{M_p}{\cos\theta_p} \tag{5.14}$$

where θ_1=$\theta(M_1)$. We want to find the configuration, which minimizes the (5.14). This formula is similar to (4.6) (Herring criterion, Chapter 4), but written in a different representation, since it uses the (100) orientation as a fixed reference and not the vicinal, which corresponds to a terrace of length M.

We have computed, for all possible combinations of terraces for p up to 7, the differences

$$\delta(M_1, ..., M_p) = \frac{\Sigma_f(M_1, ..., M_p)}{pM} - \frac{\sigma(M)}{\cos\theta}. \tag{5.15}$$

Of course, faceting occurs when $\delta < 0$.

For $p = 2$ and $N > 2$ the vicinals, corresponding to the minima of the curves of σ, do not facet and also the (3,1,1), (5,1,1) and (11,1,1) do not facet.

Increasing p, all vicinals start to facet, except the (3,1,1), (5,1,1) and (11,1,1). If p is big enough and M is bigger than 6, it is always favourite a faceting in an area of vicinal (11,1,1) (M=6 terraces) plus a flat (100)

Table 5.4:
Faceting energies, defined as in Eq.(5.14) and (5.15), with the condition (5.13), for various p. The vicinals, which are reported in the Table, belong to the order of reconstruction $N = 1$ until the (19,1,1), while the last three correspond to the vicinals for which the surface energy has a minimum for the orders of reconstruction $N = 2, 3, 4$.

Structure	*p=2* M_1, M_2	δ (meV/Å^2)	*p=3* M_1, M_2, M_3	δ (meV/Å^2)	*p=4* M_1, M_2, M_3, M_4	δ (meV/Å^2)
(7,1,1)	4,5	-1.14	3,3,6	-1.18	3,3,5,5	-1.14
(9,1,1)			3,6,6	-0.06	3,5,6,6	-0.04
(13,1,1)	6,8	-0.17	6,6 9	-0.12	6,6,8,8	-0.17
(15,1,1)			6,6,12	-0.25	6,6,6,14	-0.23
(17,1,1)	6,12	-0.43	6,8,13	-0.40	6,6,6,18	-0.57
(19,1,1)	6,14	-0.73	6,6,18	-0.92	6,6,6,22	-0.95
(25,1,1)	8,18	-0.02	6,6,27	-0.18		
(35,1,1)			6,6,42	-0.09		
(45,1,1)			6,6,57	-0.06		

part. More particularly, if we have p terraces the configuration for each M ($M \geq 6$) is characterized by $p-1$ terraces of size 6 and a terrace of size $pM-(p-1)6$. It is clear that, with increasing p, the latter terrace increases in size, eventually becoming a large flat Au(100) face. The situation is a little more complicate for the (7,1,1) and (9,1,1) ($M < 6$). By increasing p, we observe in both cases the appearance of a good percentage of terraces of size $M = 3$ (5,1,1) and $M = 6$ (11,1,1) and a very little one of size 5 (9,1,1). So in a first approximation we can say that these two vicinals facet in (5,1,1) and (11,1,1). Some of our results are summarized in Table 5.4. This analysis strongly suggests that the (5,1,1) and (11,1,1) are extremely stable surfaces, and that there is a clear tendency for other vicinals to facet into them, with the exception of (3,1,1), which has a larger inclination. A shortcoming of this scheme, however, is that it does not take into account the possibility of faceting including also the flat Au(100), which could compare only in the limit of terraces of infinite size.

So we have also adopted another method in which from the beginning

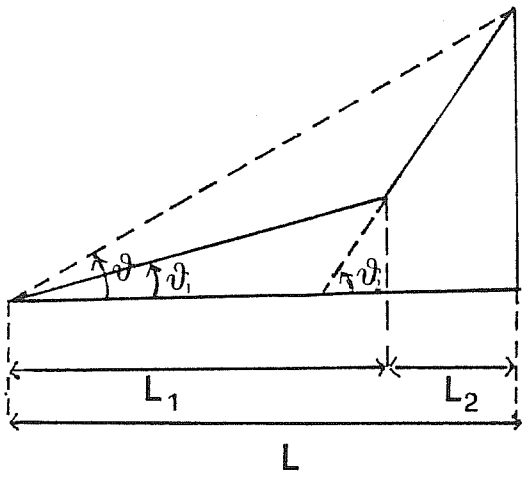

Figure 5.27:
Faceting of a vicinal inclined by an angle θ into two facets inclined by θ_1 and θ_2. Angles are measured from the (100) plane.

this possibility is comprised. In this scheme only two different types of facets are allowed. Following the suggestion of the previous analysis, we limit ourselves to consider the following three cases: (a) (100)+(5,1,1); (b) (100)+(11,1,1); (c) (5,1,1)+(11,1,1). Geometrical considerations give us the percentage of the macroscopic length (projected on the (100) plane) L in which the two facets under consideration appear. In particular (see Fig. 5.27) for a given inclination θ of the vicinal surface and the faceting in two types of facets of inclination θ_1 and θ_2, these two conditions must be imposed:

$$L_1 + L_2 = L \tag{5.16}$$

$$L_1 \tan\theta_1 + L_2 \tan\theta_2 = L \tan\theta. \tag{5.17}$$

These conditions determine the fractions of the areas projected on (100) plane, L_1/L and L_2/L, respectively occupied by the two facets.

To calculate an effective surface energy for the faceted geometry, one has to properly take into account the areas of the two facets, whose sum exceeds, of course, the area of the unfaceted surface. By referring the surface energies to areas projected on the (100) plane, the effective surface energy $\sigma(\theta)/\cos\theta$ becomes, after faceting,

$$\Sigma_f(\theta,\theta_1,\theta_2) = \frac{L_1}{L}\frac{\sigma(\theta_1)}{\cos\theta_1} + \frac{L_2}{L}\frac{\sigma(\theta_2)}{\cos\theta_2} \tag{5.18}$$

so that the faceting energy is given by

$$\delta(\theta,\theta_1,\theta_2) = \Sigma_f(\theta,\theta_1,\theta_2) - \frac{\sigma(\theta)}{cos\theta}. \tag{5.19}$$

For each value of θ corresponding to a (K,1,1) vicinal, we set θ_1 and θ_2 to correspond to the cases (a), (b), (c) listed above (when compatible with the conditions (5.16) and (5.17)) and then calculate $\delta(\theta, \theta_1, \theta_2)$. For $\sigma(\theta)$, we always choose the lowest value among those corresponding to different reconstruction orders (see Table 5.2). The results are shown in Table 5.5 and in Fig. 5.28.

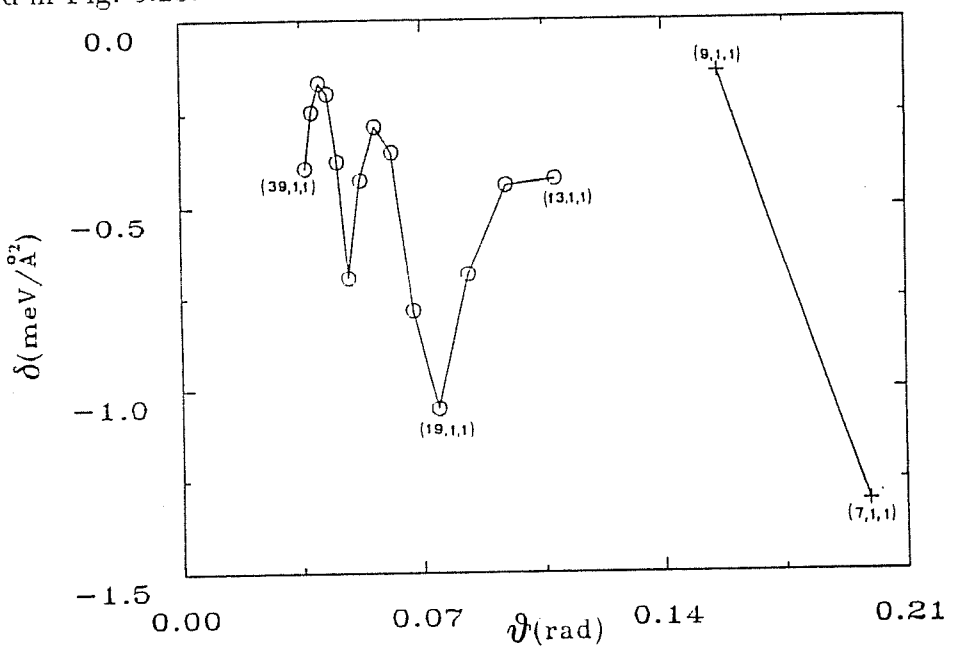

Figure 5.28:
For each vicinal, only the case yielding the lowest δ is reported. The indicated vicinals belong to the order of reconstruction $N = 1, N = 2, N = 3$. o indicate faceting into (11,1,1)+(100), + into (5,1,1)+(11,1,1).

All the vicinals considered, except (3,1,1), (5,1,1) and (11,1,1) gain energy by faceting. As it is natural to expect, the energetic gain is higher for vicinals, whose σ values lie near the points of crossing between two different orders of reconstruction, and lower for vicinals whose σ values lie near the points of minimum for each order of reconstruction. Naturally the energetic gain achieved for all vicinals, represents the energetic gain in the limit $p \to \infty$ of our previous calculations. The largest energy gain is observed on (7,1,1). As it turns out, this surface can facet in two ways. In the best case, it divides in a portion (52%) of (5,1,1) and another one

Table 5.5:
Faceting energies δ of (100) vicinals into (5,1,1)+(11,1,1), (11,1,1)+(100) and (5,1,1)+(100). θ is the vicinal angle, L, L_1 and L_2 are as from Fig. 5.27, δ is defined by Eq.(5.14). We have examined the vicinals up to $N = 3$.

Structure	$\sigma(\theta)/\cos\theta$ (meV/Å^2)	L_1/L *(5,1,1)*	L_2/L *(11,1,1)*	δ (meV/Å^2)	L_1/L *(5,1,1)*	L_2/L *(100)*	δ (meV/Å^2)
(7,1,1)	109.11	0.52	0.48	-1.31	0.71	0.29	-0.81
(9,1,1)	106.33	0.81	0.19	-0.14	0.56	0.44	+0.64
(11,1,1)	105.16				0.45	0.55	+0.95
Structure		L_1/L *(11,1,1)*	L_2/L *(100)*				
(13,1,1)	105.15	0.85	0.15	-0.42	0.38	0.62	+0.38
(15,1,1)	104.84	0.73	0.27	-0.44	0.33	0.67	+0.26
(17,1,1)	104.84	0.65	0.35	-0.68	0.29	0.71	-0.07
(19,1,1)	105.01	0.58	0.42	-1.05	0.26	0.74	-0.50
(21,1,1)	104.99	0.52	0.48	-0.78	0.24	0.76	-0.28
(23,1,1)	103.97	0.48	0.52	-0.35	0.22	0.78	+0.10
(25,1,1)	103.84	0.44	0.56	-0.28	0.20	0.80	+0.14
(27,1,1)	103.89	0.41	0.59	-0.43	0.19	0.81	-0.04
(29,1,1)	104.08	0.38	0.62	-0.69	0.17	0.83	-0.33
(31,1,1)	103.47	0.35	0.65	-0.38	0.16	0.84	-0.04
(33,1,1)	103.45	0.33	0.67	-0.20	0.15	0.85	+0.12
(35,1,1)	103.36	0.31	0.69	-0.17	0.14	0.86	+0.13
(37,1,1)	103.24	0.30	0.70	-0.24	0.14	0.86	+0.04
(39,1,1)	103.50	0.28	0.72	-0.39	0.13	0.87	-0.12

(48%) of (11,1,1); in this case $\delta = -1.3$ meV/Å^2. For a division in a part (71%) of (5,1,1) and another part (29%) of flat Au(100), the energetic gain is, instead, $\delta = -0.8$ meV/Å^2. This type of faceting has been experimentally observed [88]. (9,1,1) also facets in (5,1,1)+(11,1,1), with an energetic gain $\delta = -0.14$ meV/Å^2, while faceting in (5,1,1)+(100) yields a small surface energy increase ($\delta = +0.64$ meV/Å^2).

As a check, we have also calculated the energetic gains for faceting of vicinals into (K,1,1)+(100), with varying K. Results for some vicinals are reported in Fig. 5.29, where the horizontal axis represents the fraction

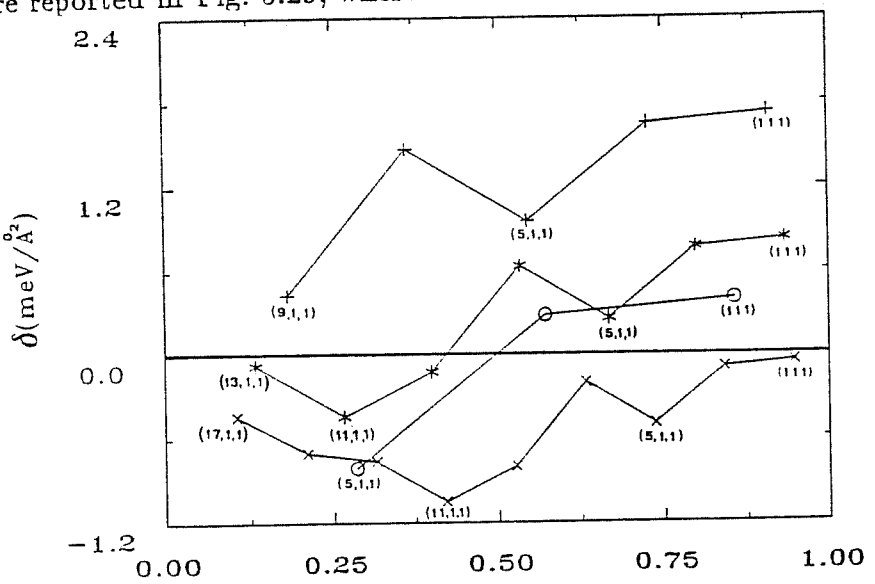

Figure 5.29:

The energetic gain versus the percentage of (100) for some vicinals with order of reconstruction $N = 1$. Each line corresponds to a vicinal, in particular, × refers to (19,1,1), * to (15,1,1), + to (11,1,1) and ∘ to (7,1,1). The Miller indexes denote the orientation of one of the two facets, the other being a (100) facet. We can notice that δ for (11,1,1) is always positive, i.e., no faceting occurs. For each vicinal, increasing the percentage of flat part, the Miller index K of the other vicinal in which the faceting occurs, decreases. So, for instance, for the (15,1,1) the first point on the left corresponds to a faceting in the (13,1,1) and (100), while the last on the right corresponds to a division in (111) and (100). We can note also that a minimum occurs for (19,1,1) and (15,1,1) when the faceting comprises a portion of (11,1,1).

of (100) facet with respect to the total (100)-projected area. The results confirm that, as expected from the calculations presented above, (5,1,1) and (11,1,1) are the preferred facets, although negative δ may occur also with other facets.

We have checked also the possibility of a faceting in three parts (the vicinals (5,1,1) and (11,1,1) together with the flat Au(100)), but in all cases the faceting in two parts gives a better energetic gain.

We have made an attempt to study the dynamics of faceting by MD. To this end, we have chosen the vicinal (7,1,1), which has the strongest tendency to facet, and performed a 10000 steps annealing/quenching thermal cycle. Due to the large mass transport required to form facets, which presumably would imply a rather slow kinetics for the process, we have chosen a relatively high annealing temperature (900 K). In the final configuration, the original 4-rows wide terraces had completely disappeared, and parts with a (5,1,1) orientation can be clearly distinguished (Fig. 5.30). On the whole, however, the structure is rather disordered and the surface energy is slightly higher than that of the unfaceted (7,1,1). This partial failure can be attributed to the limited size of the MD box and, perhaps, more likely, to the limited annealing time (corresponding to about 70 psec).

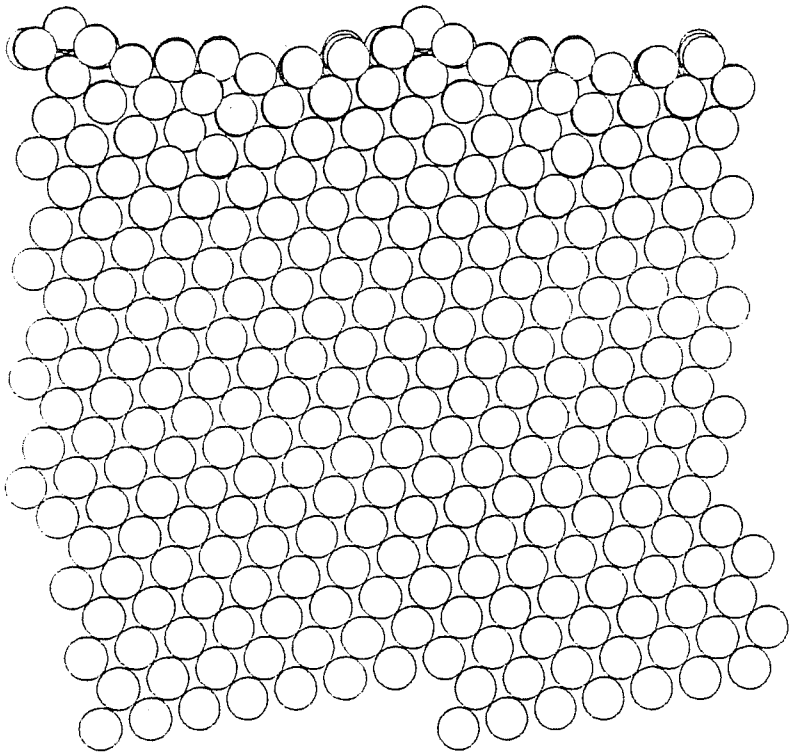

Figure 5.30:
(7,1,1) in the case $N = 0$. Annealed sample (900 K). Two MD boxes are shown in y' direction. We can note that parts with a (5,1,1) orientation can be distinguished.

Chapter 6

Simulation of Au(111)-vicinals

6.1 General description of (M+1, M−1, M) Au(111)-vicinals

In this Chapter we present a study of the energetic and structural properties of Au(111)-vicinals, conducted in a way similar to the study of Au(100)-vicinals presented in Chapter 5.

We recall that the "glue model" predicts $p = 11$ as the best periodicity for the $(p \times \sqrt{3})$ reconstruction unit cell of Au(111), differently from experimental results, which give $(p \times \sqrt{3})$ with $p = 21 - 23$. So all terrace-lengths, about which we will speak about, will be presumably shorter than the real ones by about a factor equal 2. Nevertheless, it is interesting to study what the model would qualitatively predict also for Au(111)-vicinals.

In particular, we have undertaken a quantitative study of the Au(111) vicinals, inclined along the zone $[11\bar{2}]$-axis [107]. These consist of $[11\bar{2}]$ (henceforth y-direction) straight steps, separated by (111) terraces, which are M atoms wide in the $[1\bar{1}0]$ direction (henceforth x) and infinitely extended along y. The length of the terrace along x determines the angle of inclination of the vicinal, $\theta = \arctan \sqrt{\frac{2}{3}} \frac{1}{M}$.

We shall also call z the [111] direction, x' the $[2 - 3M, 2 + 3M, 2]$ and z' the $(M + 1, M - 1, M)$ ones, respectively (see Fig. 6.1). x', y, z' form an orthogonal system, obtained by rotating the x, y, z system by an angle θ along the y axis.

The geometry of (111) makes the construction of a MD box with the

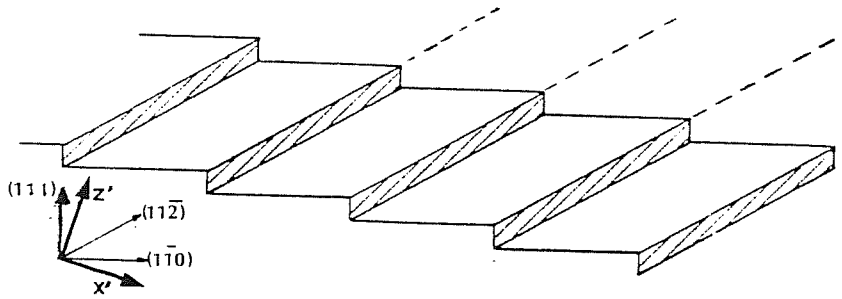

Figure 6.1:
Au(111) vicinals inclined along the [11$\bar{2}$] zone-axis (geometrical scheme). The dashed line indicates an infinite extension along the [11$\bar{2}$] direction.

free surface parallel to a (111)-vicinal surface rather cumbersome. In fact, if we limit ourselves to the more practical parallelepiped boxes, the typical $ABCABC...$ stacking of (111) layers forces us to include three terraces (and three steps) in a single box in order to have a match by periodic boundary conditions at the box boundaries. Together with the necessity to study long terraces (dictated by the large periodicity of the Au(111) reconstruction), this would give rise to very large MD samples.

Therefore, we have chosen to study a simplified system with the free surfaces parallel to (111), and two terraces separated by two opposite steps. To study by MD such Au(111)-vicinals, in this case we have constructed a very simplified, not tilted MD box with two steps that, with unchanged PBC, does not simulate the real vicinal (Fig. 6.2). We expect the difference with the tilted system to be rather small, particularly for the largest terraces, since the interaction among steps is supposed to decay in both cases as their inverse square distance.

The size of the terraces has been taken $(M \times L\sqrt{3})$ in units of d, the bulk first-neighbour distance; M, which is the terrace length in the contraction [1$\bar{1}$0] direction, has been varied, while L in [11$\bar{2}$] has been taken equal to 2, since it is not expected to play any particular role, not being the [11$\bar{2}$] the reconstruction direction. In our geometry, the inclination is roughly simulated by the size of the terrace along x. In a first approximation, we can take $\theta \simeq \sqrt{\frac{2}{3}}\frac{1}{M}$. As in the case of Au(100)-vicinals, we study various

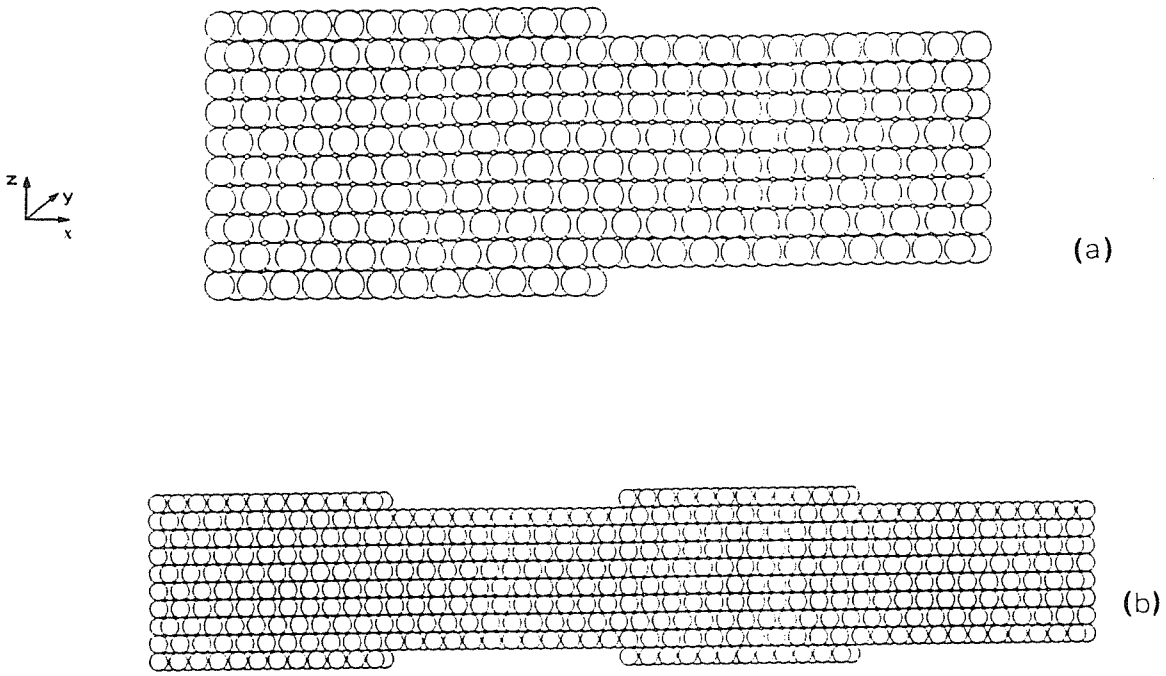

Figure 6.2:
(a) An example of our MD box for a (12,10,11) perfect starting sample.
(b) Two MD boxes in x direction, which, with the usual periodic boundary conditions, give a very simplified model of a vicinal.

orders of reconstruction, by accommodating $M + N$ atoms over M in the $[1\bar{1}0]$ direction on each terrace. $N = 0$ means absence of reconstruction.

We have kept two free surfaces and used the symmetric geometry of Fig. 6.2, which does not allow stresses to flatten out the steps. The two surfaces are treated identically, and are both monitored in the calculation.

We have used 10-layers slabs and the biggest sample considered, corresponding to $M = 90$, contains about 6500 particles.

6.2 Structure and energetics of (M+1,M−1,M) Au(111)-vicinals

Following the strategy already described in Section 1.4, we have minimized the energy of our slabs by relaxing them by MD. In some preliminary cases, both direct quenching and annealing at finite temperature, followed by quenching, have been used. The differences in surface energy between these two methods are usually less than 0.5 meV/Å^2 in favour of the annealed samples; they increase a little only for the smallest cells ($M < 5$). Because of these small differences, both in structure and energetics, we have decided to perform the calculations by using only the direct quenching procedure, which requires much less computer time.

We have studied 75 configurations, differing in the terrace sizes (ranging from 2 to 90 rows) and in the reconstruction order (from $N = 0$ to $N = 4$). The surface energy results are summarized in Table 6.1 and in Fig. 6.3. Our results are shown for MD simple quenching in Fig. 6.3 and in Table 6.1.

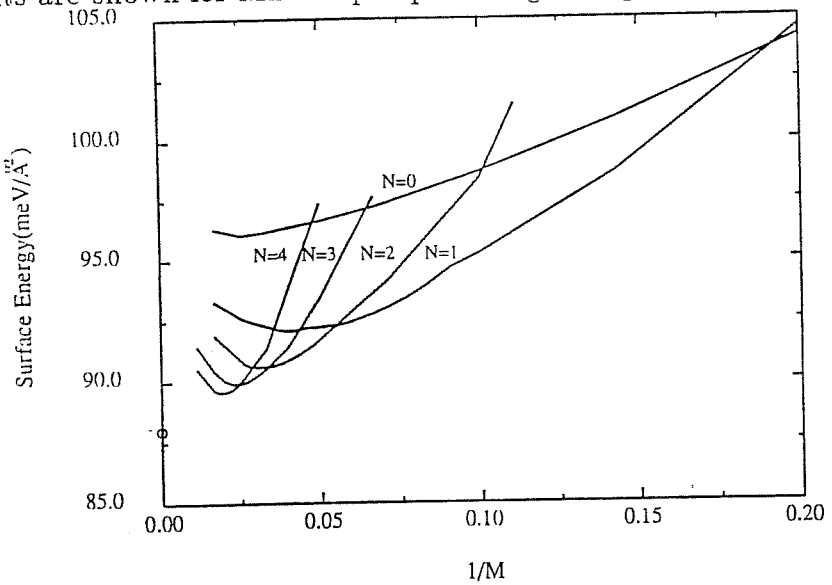

Figure 6.3:
Surface energy as a function of the inverse terrace length. Each curve corresponds to a different order of reconstruction N. The dot on the ordinate axis indicates the flat reconstructed Au(111) surface energy in our model [69,68].

The following observations can be made:

Table 6.1:

Surface energies for several Au(111) vicinals and different reconstruction orders N.

Structure	$\sigma(\theta)$ $(meV/\AA^2)$ *N=0*	$\sigma(\theta)$ $(meV/\AA^2)$ *N=1*	$\sigma(\theta)$ $(meV/\AA^2)$ *N=2*	$\sigma(\theta)$ $(meV/\AA^2)$ *N=3*	$\sigma(\theta)$ $(meV/\AA^2)$ *N=4*
(3,1,2)	126.14				
(4,2,3)	113.86				
(6,4,5)	104.22	104.60			
(7,5,6)		101.85			
(8,6,7)	100.89	98.68			
(9,7,8)		96.88			
(10,8,9)		96.55	101.49		
(11,9,10)	98.70	95.29	98.43		
(12,10,11)		94.72			
(13,11,12)		93.98			
(14,12,13)		93.45			
(15,13,14)		93.08	94.22		
(16,14,15)	97.23	92.80		97.65	
(18,16,17)		92.43			
(19,17,18)		92.33			
(20,18,19)		92.30	92.06		
(21,19,20)	96.66	92.25		93.48	97.38
(22,20,21)			91.50		
(23,21,22)		92.22			
(24,22,23)			91.14		
(25,23,24)		92.11	91.00		
(26,24,25)	96.39			91.43	
(27,25,26)		92.10	90.79		
(29,27,28)			90.67		
(30,28,29)		92.24	90.65	90.73	
(31,29,30)	96.21		90.63	90.58	91.38
(33,31,32)				90.35	
(34,32,33)		92.40	90.61		
(36,34,35)	96.12		90.63	90.12	
(38,36,37)		92.54		90.01	
(39,37,38)			90.74		90.19
(41,39,40)	96.06	92.64		89.93	
(42,40,41)				89.93	
(43,41,42)					89.83
(44,42,43)				89.93	
(46,44,45)				89.94	89.69
(49,47,48)					89.60
(51,49,50)				90.05	89.58
(56,54,55)					89.57
(61,59,60)	96.33	93.31	91.94	90.45	89.65
(91,89,90)				91.48	90.55

(a) Each curve, corresponding to a given reconstruction order N, has a minimum for $M \simeq 11N + K$, with $K \simeq 11$. As it will be further clarified in the following, $11N$ is the terrace length which realizes the optimal packing density (12 rows over 11) for each reconstruction order N. The surface energy minima are shifted by K, since there is also a tendency to reduce the step density due to the energetic cost of the step. Note that this would be the only energetic term for a vicinal surface of a non-reconstructing material, so that no minima as a function of the step density (or the inverse of the terrace size) would be present in this case. The presence of a shallow minimum, also in the unreconstructed case, will be explained further.

(b) As Fig. 6.3 shows, the lower envelope of the family of curves tends, for $\frac{1}{M} \to 0$ to a limiting value $\sigma_0 \simeq 88.2$ meV/Å^2. In complete analogy with the Au(100) case (see Subsection 5.2.2), σ_0 is the surface energy of the flat reconstructed Au(111), as established in Section 3.2. This is natural, thinking that in this limit the presence of the steps has no importance. The lower envelope of the family corresponds to vicinal surfaces, where the top layer atomic density is always kept equal to the optimum value (corresponding to keeping $(M/N) \simeq 11$).

(c) Each curve (N fixed) tends for $\frac{1}{M} \to 0$ to a limiting value $\sigma_1 \simeq 96.6$ meV/Å^2. This is the surface energy of a flat *unreconstructed* Au(111), as it is to be expected, since, in this limit, the excess density of the terraces N/M vanishes as the step contribution.

A typical final configuration is shown in Fig. 6.4, which refers to the case $M = 11$, $N = 1$. Terraces have here their optimal density, and exhibit the atomic structure typical of the Au(111) reconstruction, with the stacking changing continuously from fcc to hcp and vice versa. Other configurations are shown in Fig. 6.5 ($M = 33$, $N = 2$) and Fig. 6.6 ($M = 5$, $N = 0$).

It should be noted that, in our simplified geometry, the two terraces in the first and in the second layer, are not treated symmetrically. Therefore, as a consequence of the energy minimization, one of them might grow in size at the expense of the other, if this contributes to lower the energy. This effect occurred quite systematically when the top layer density was far from the optimal value in the starting configurations. The resulting in-plane stress originates a contraction (or expansion) of the "top" terrace, which brings the terrace density closer to the optimum one. A contraction is clearly visible in Fig. 6.6, where the two terraces have not the same measure. The little shift of the topmost layer respect to the second one, is,

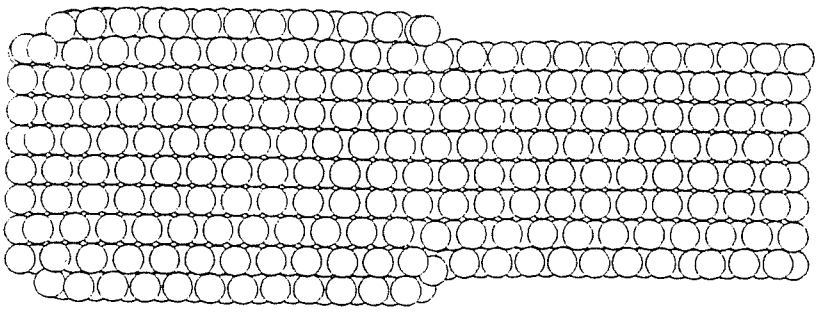

(a)

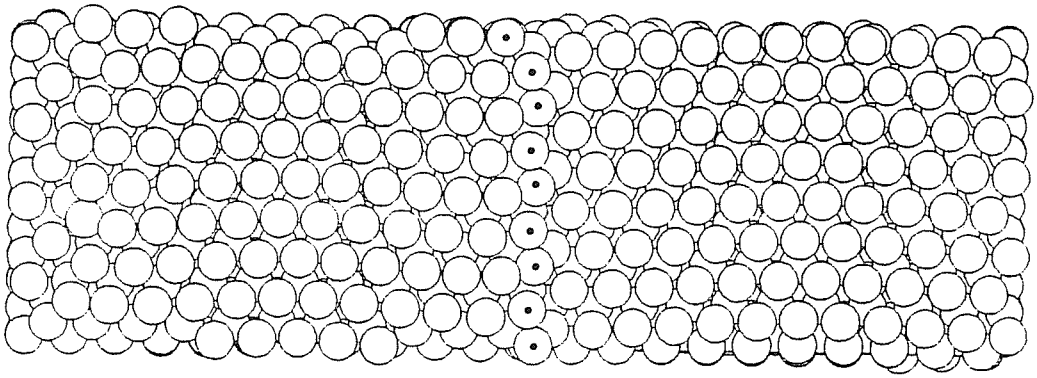

(b)

Figure 6.4:
(12,10,11) in the case $N = 1$.
(a) Slab profile.
(b) Top view, in which it is possible to observe two $(11\times4\sqrt{3})$ terraces, separated by two steps. One step is located near the middle, the other near the right edge. The atoms at the step zone in the upper terrace are drawn with a •

instead, visible in all the samples.

Such mechanism of contraction explains why in the $N = 0$ case vicinals with large terraces have a surface energy slightly lower than that of the flat non-reconstructed (111), $\sigma_1 = 96.6$ meV/Å^2. In our model, in fact, non-reconstructed (111) presents a large tensile stress, which terrace shrinking on the pseudo-vicinal partially relieves. These effects are an artifact of the simplified geometry, and would disappear if a real tilted vicinal was constructed. In practice, however, they are important only for vicinals with non-optimal packing, which are in metastable states, while in the remainder of this Chapter we are concerned only with stable states (i.e, those on the lower envelope in Fig. 6.3).

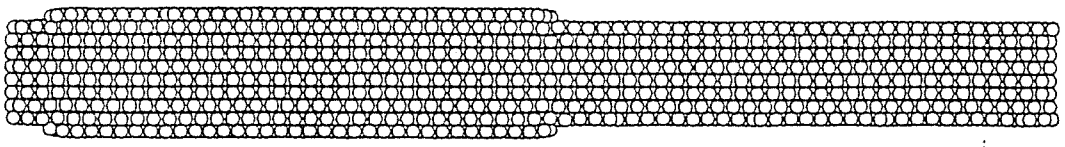

(a)

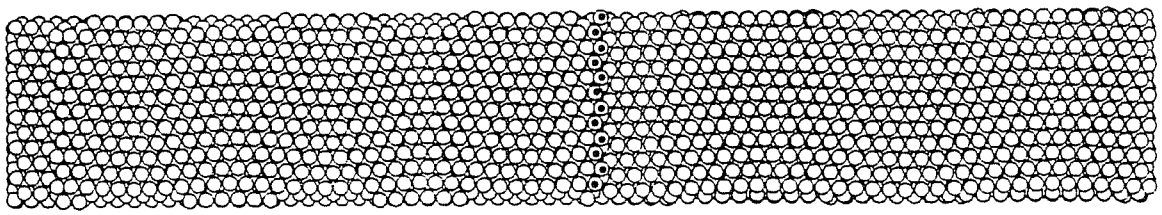

(b)

Figure 6.5:
(34,32,33) in the case $N = 2$. Two $(33 \times 6\sqrt{3})$ terraces are shown. The atoms at the step zone in the upper terrace are drawn with a •.
(a) Slab profile.
(b) Top view.

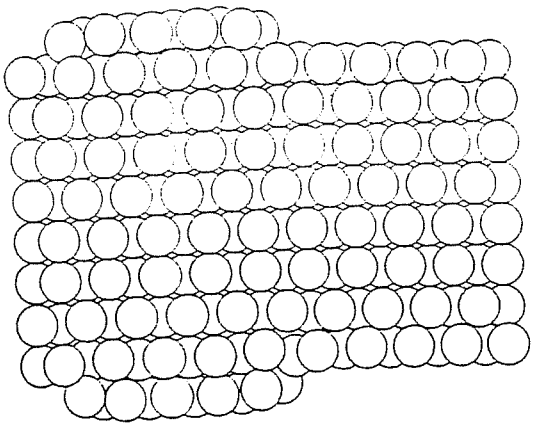

Figure 6.6:
(6,4,5) in the case $N = 0$. Slab profile. Note a slight in-plane contraction of the terraces at the top.

6.3 A model for the surface energies of quenched samples

As done for Au(100) vicinals, we have tried to reproduce our results with a simple model in which the surface energy is written as a sum of two contributions, coming respectively from terraces and from steps:

$$\sigma(M,N) = \sigma_{terrace}(M,N) + \sigma_{step}(M,N). \tag{6.1}$$

Similarly to the Au(100) vicinal case, the term due to the flat terraces is obtained generalizing for every order of reconstruction the quadratic fit in $1/M$ of the MD results, obtained for the flat Au(111) surface:

$$\sigma_{flat}\left(\frac{N}{M}\right) = a + b\left(\frac{N}{M}\right) + c\left(\frac{M}{M}\right)^2. \tag{6.2}$$

We have chosen the coefficients $a = 95.40$ meV/Å^2, $b = -156.42$ meV/Å^2, and $c = 849.34$ meV/Å^2, which differ slightly from those reported in Section 3.2, but reproduce better the MD results in the region we are now mostly interested in, i.e. around the minimum ($M = 11$). In particular, $\sigma_{flat}\left(\frac{1}{11}\right) = \sigma_0 = 88.2$ meV/Å^2 is the precise value of the minimum, as obtained by MD. We are thus led to write

$$\sigma_{terrace}(N,M) = a + b\left(\frac{N}{M}\right) + c\left(\frac{N}{M}\right)^2 \tag{6.3}$$

that is we regard each terrace as a piece of flat surface with a top layer excess density N/M, due to the stacking of $M+N$ rows over M.

Contrary to the case of (100)-vicinals, where a correction, shifting the position of the minima, had to be introduced to reproduce quench results (see Eqs. (5.5) and (5.6)), this expression fits enough well the data obtained by energy minimization. Note that the above formula works also for $N = 0$, yielding a surface energy independent of the terrace length M, as expected for a non-reconstructed surface.

For the step term, we assume

$$\sigma_{step}\left(\frac{1}{M}\right) = \frac{\mu}{M} + \frac{g}{M^3} \tag{6.4}$$

which is independent from the reconstruction order N. As discussed in Subsection 5.2.3, this is derived by fitting p steps onto a distance L (whence $L = pMd$), writing the total step energy per unit length as $E = p\mu d + ph/Md^2$ and taking $\sigma_{step} = E/L$. μ and h can be interpreted respectively as the step chemical potential and the step-step interaction constant. We take $g = \frac{h}{d^3}$.

To fit μ and g, we have used the surface energies of vicinals with $M = 11N$ ($N = 1, 2, 3, 4$), as extracted from Table 6.1. All these vicinals, which have the optimal density $\sigma_{terrace} = \sigma_0$, should follow the curve

$$\sigma_{min} = \sigma_0 + \frac{\mu}{M} + \frac{g}{M^3}. \tag{6.5}$$

With this procedure we have fixed $\mu = 68.2$ meV/Å^2 and $g = 480$ meV/Å^2. The resulting surface energy model is shown in Fig. 6.7. The lower envelope of the family of curves, indicated by a thicker line, denotes stable states. It should be remarked that the absolute minima as a function of M, for fixed N, which occur at $M_N \simeq 11N + K$, with $K \simeq 11$ in the MD data, and $K \simeq 5$ in the parametrization, do *not* correspond to stable states. In fact, by increasing M, the transition from the reconstruction order N to $N + 1$ occurs before M_N is reached. In other words, the derivative of the envelope curve, as a function of $1/M$, is always positive, in contrast with the case of (100) vicinals, where the envelope curve presents true minima. This is due to the high energetic cost of the steps on Au(111), which is so high to move the position of the minima towards larger cells, which can be in a state of density enough far from the optimal density of the flat surface 12/11. In fact, the step energy per unit length is $\epsilon = \mu d = 200$ meV/Å, which is about 4 times bigger than in the Au(100) case. Apart from the obvious effect of the larger interplanar spacing of Au(111), an additional reason for these differences may be found in the closer packing of Au(111), which reduces the inward relaxation effects, and therefore makes the steps somewhat more sharp.

In Fig. 6.7 we see that also the case $N = 0$ can be described within our simple model. It consists of the constant a plus the step term and, as a consequence, it has an increasing trend, if the step density increases. So for Au(111)-vicinals with unreconstructed terraces, we can give an analytical expression in the $N = 0$ case, differently from what happens in the Au(100) case, where the surface energy of the unreconstructed surfaces (which are,

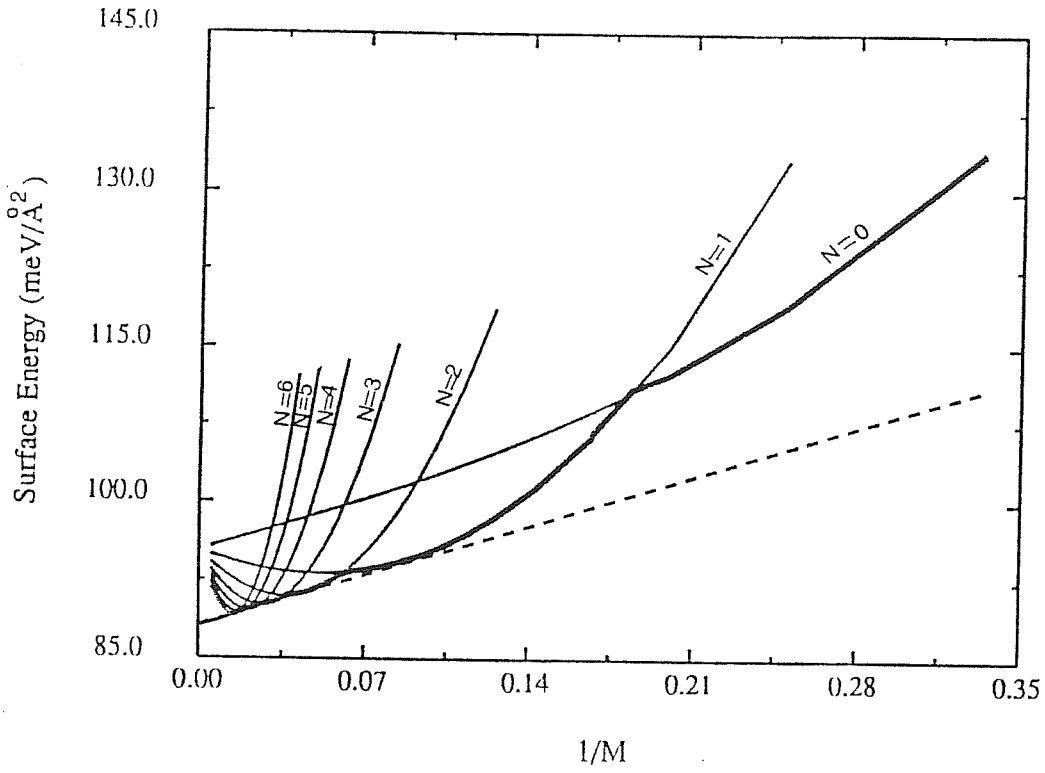

Figure 6.7:
Surface energies curves for the various orders of reconstruction versus the step density $1/M$. The thick line (lower envelope) indicates the effective vicinal surface energy. The pendency of the dashed line gives the chemical potential μ of the steps.

on the other hand, extremely instable), decreasing the step density, has an increase trend.

Finally, we would like to comment on the step-step interaction constant, which is $g \simeq 480$ meV/Å^2 for Au(111)-vicinals, but only $g \simeq 50$ meV/Å^2 for Au(100)-vicinals. This behaviour probably again reflects the stronger individuality of the (111) step. The details are not clear at this stage. These two numbers, anyway, are not to be taken too seriously, because it should be kept in mind that our estimates for the step-step interaction are not very reliable, since they express very tiny deviations from linearity of σ as a function of $1/M$ and are very sensitive to the exact choice of the linear coefficient.

6.4 "Stabilized" (M+1, M−1, M) Au(111)-vicinals

6.4.1 The "tilting pressure"

The coefficient μ of the linear term in Eq.(6.4) is linked also to the minimum value for the "tilting pressure" which, also in this case, can be introduced to perform the "Maxwell construction" to find the minima of the Gibbs surface free energy $g(\theta) = \sigma(\theta)/\cos\theta - \pi\theta$ (see Section 5.3). As in the (100) case, this is done by calculating all the intersections between the straight line $r = \sigma_o + \pi\theta$ and the effective vicinal surface energy. Instead of the step density $1/M$, we have used the "tilting angle" $\theta \simeq \sqrt{\frac{2}{3}}\frac{1}{M}$ as the independent variable. As the tilting pressure π is increased above the threshold value $\pi_c = \sqrt{\frac{2}{3}}\mu \simeq 83.5$ meV/Å^2/rad, the value of the chemical potential of the steps, θ begins to increase. The increase is not continuous, but rather by discrete steps, obtaining a series of stabilized high-Miller index vicinals, each corresponding to a different order of reconstruction (see Fig. 6.8). Of course N decreases with increasing θ, roughly keeping $N\theta$ constant. When N becomes 5 or less, we find for each N rather than a single stabilized vicinal, a plateau, starting with a vicinal with the nearly optimal terrace ($M \simeq 11N$) and continuing with denser terraces. In the case $N = 1$, for instance, the plateau begins with $M = 12$ and includes all $M's$ down to $M = 6$. This behaviour can be seen more clearly in the log-log plot of Fig. 6.9.

The analytic form for $\pi(\theta)$ near to the limit value $\pi_c \simeq 83.5$ meV/Å^2/rad when θ goes to zero, is linear.

$$\pi(\theta) = \pi_{min} + A\theta \tag{6.6}$$

with $A = \sigma_0/2$ meV/Å^2. This can be easily found by approximating the envelope curve by

$$\frac{\sigma(\theta)}{\cos\theta} \simeq \left(\sigma_0 + \sqrt{\frac{3}{2}}\mu\theta + g\left(\sqrt{\frac{3}{2}}\right)^3\theta^3\right)\left(1 + \frac{\theta^2}{2}\right) \tag{6.7}$$

and making it equal to $\sigma_0 + \pi\theta$. We observe that the factor $1/\cos\theta$ by which $\sigma(\theta)$ is multiplied is crucial in determining the behaviour of $\pi(\theta)$. In

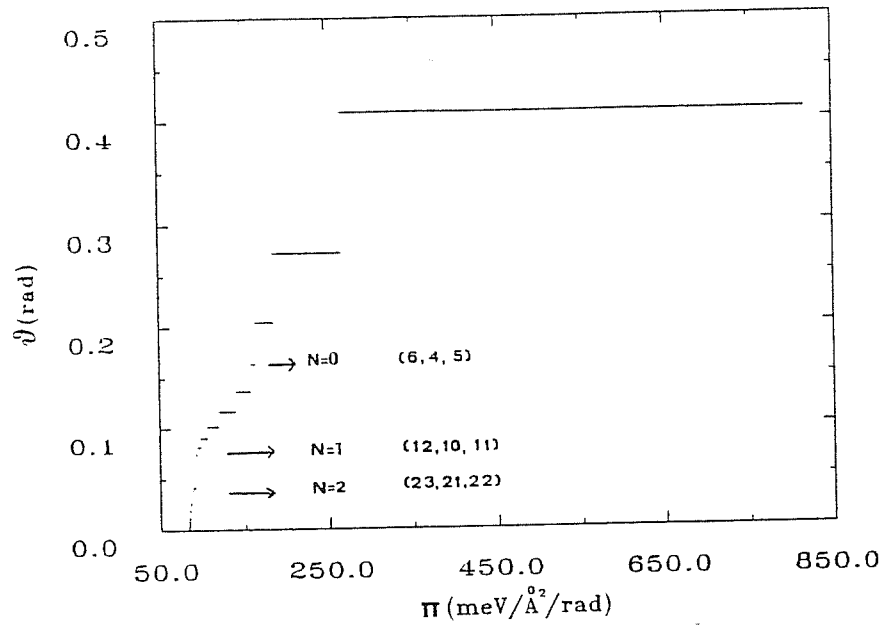

Figure 6.8:
The "tilting angles", corresponding to different vicinals, versus the "tilting pressure"; each horizontal line corresponds to a different "stabilized" vicinal.

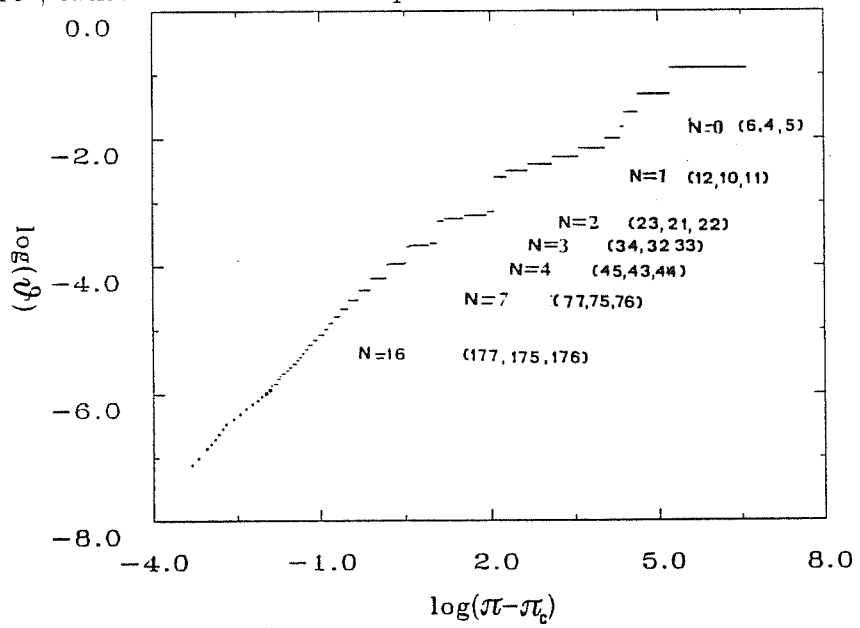

Figure 6.9:
Logarithmic plot of the tilting pressure; π_c represents the minimum value for the tilting pressure to get an intersection in the Maxwell construction. The "islands" of stabilized vicinals for the orders of reconstruction $N = 0, N = 1, N = 2$ are well visible.

fact, it gives a contribution θ^2, which overcomes the step-step interaction contribution of the order of θ^3.

It may be interesting to note that the motion of atoms, requested to pass from an order of reconstruction to another one, could take place on a very long time scale. For example, the 1×1 (metastable)$\rightarrow 1 \times 5$ (stable) transition of Ir(100) requires an activation temperature of at least $800K$ to be observed on a time scale of several minutes [110]. Therefore metastable states could also be observed under certain experimental conditions.

Informations about the stability of the vicinals $(M+1, M-1, M)$ could have been obtained also from the Wulff plot, where such vicinals cover the range of θ between the (111) ($M \rightarrow \infty$) and $(1\bar{1}0)$ (M=0) ($\theta \simeq 90^0$). Resulting all vicinals higher in energy than the flat Au(100), like for the Au(100) it has resulted that, in vicinity of (111) direction, none of the vicinals is naturally preferred to the low index orientation ones.

The stabilized vicinals, above found, similarly to the stabilized (K,1,1) Au(100)-vicinals, have no impact on the macroscopic crystal habit, i. e., they do not contribute to the equilibrium crystal shape, which is, in fact, formed by facets (111) and (110) divided by sharp edges.

6.4.2 The faceting of (M+1,M−1,M) Au(111) vicinals

Similarly to the Au(100) case, we have proceeded to investigate the possibility of faceting for Au(111) vicinals.

We limit ourselves to discuss our results for faceting in two parts. We have taken the surface energies from our parametrization of Fig. 6.7. The details of the calculation follow the scheme outlined in Subsection 5.3.3 for the faceting of Au(100) vicinals.

Table 6.2 reports the faceting energies for all $(M+1, M-1, M)$ vicinals with $M \leq 38$. Only faceting into a flat (111) part and a more tilted part is considered. For each vicinal, only the best case (the lowest δ) is reported. Vicinals which are missing in the list, do not facet (i. e., the best case has still $\delta > 0$). Note that faceting does not occur for $M < 13$, $19 \leq M \leq 22$, $31 \leq M \leq 33$. These vicinals have terraces lengths $M \simeq 11N$, and are therefore stabilized by reconstruction. Vicinals with $13 \leq M \leq 18$

Structure	L_1/L *Structure*	L_2/L *Structure*	δ $(meV/\AA^2)$
(14,12,13)	0.92 (13,11,12)	0.08 (111)	-0.09
(15,13,14)	0.86 (13,11,12)	0.14 (111)	-0.22
(16,14,15)	0.80 (13,11,12)	0.20 (111)	-0.39
(17,15,16)	0.75 (13,11,12)	0.25 (111)	-0.57
(18,16,17)	0.71 (13,11,12)	0.29 (111)	-0.37
(19,17,18)	0.66 (13,11,12)	0.34 (111)	-0.12
(24,22,23)	0.96 (23,21,22)	0.04 (111)	-0.02
(25,23,24)	0.92 (23,21,22)	0.08 (111)	-0.05
(26,24,25)	0.88 (23,21,22)	0.12 (111)	-0.11
(27,25,26)	0.85 (23,21,22)	0.15 (111)	-0.18
(28,26,27)	0.82 (23,21,22)	0.18 (111)	-0.25
(29,27,28)	0.78 (23,21,22)	0.22 (111)	-0.16
(30,28,29)	0.76 (23,21,22)	0.24 (111)	-0.08
(31,29,30)	0.73 (23,21,22)	0.27 (111)	-0.03
(35,33,34)	0.97 (34,32,33)	0.03 (111)	-0.01
(36,34,35)	0.94 (34,32,33)	0.06 (111)	-0.03
(37,35,36)	0.92 (34,32,33)	0.08 (111)	-0.06
(38,36,37)	0.89 (34,32,33)	0.11 (111)	-0.10
(39,37,38)	0.87 (34,32,33)	0.13 (111)	-0.14

Table 6.2:

Energy gains for faceting of $(M+1, M-1, M)$ (111)-vicinal surfaces into a more tilted vicinal plus a portion of flat (111). L_1/L is the fraction of area projected onto (111), occupied by the facet, and L_2/L is the fraction of flat part. For each vicinal, we have selected, among all faceting possibilities, that with the largest energetic gain δ. Vicinals, which do not appear, are stable, i.e. they do not facet. All cases from $M = 13$ to $M = 38$ have been considered.

gain energy by faceting into (111)+(12,10,11); those with $23 \leq M \leq 30$ into (111)+(23,21,22), and those with $34 \leq 38$ into (111)+(34,32,33). The energetic gain is larger for those vicinals, such as (17,15,16), which fall near the cusps (corresponding to points of crossing between two different orders of reconstruction) in the envelope curve of Fig. 6.7.

This type of faceting is not the best one. It results, in fact, more convenient for a vicinal with $M = 11N + R$ (where R is an integer between 1 and 9 or 10) a faceting in which the vicinal of lower Miller indices has $M \simeq 11N$ and that of higher Miller indices has $M \simeq 11(N+1)$, as it is shown in Table 6.3 and in Fig. 6.10. Once again, vicinals near the cusps

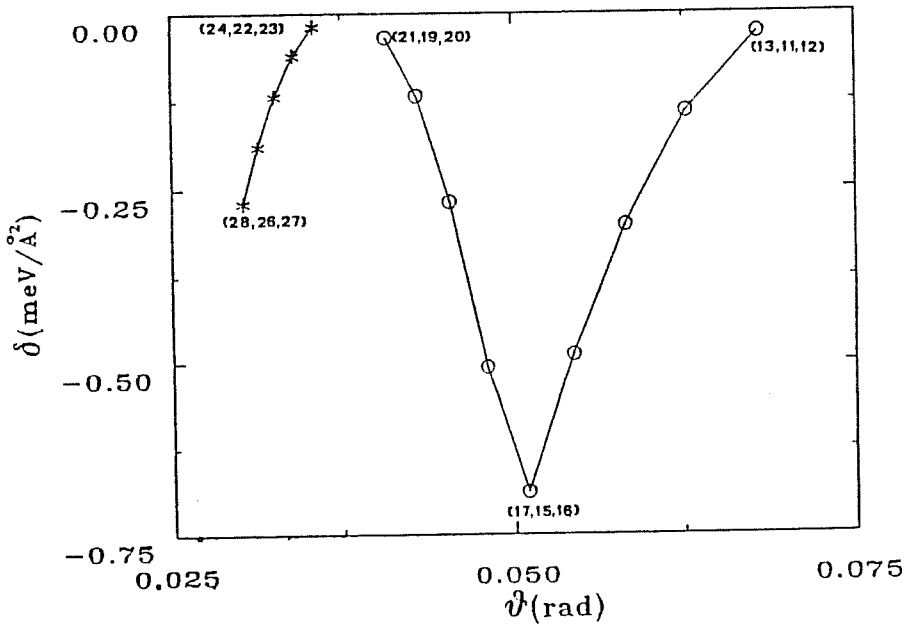

Figure 6.10:
Faceting energy gains as a function of the tilting angle θ for the vicinals of order $N = 1$ and $N = 2$. o indicate the vicinals which facet in a part of (12,10,11) and in a part of (22,20,21); $*$ indicate the vicinals, which facet in a part of (23,21,22) and in a part of (34,32,33).

of the envelope curve are those which gain more energy by faceting. Note also the occurrence of faceting of (6,4,5) and (7,5,6) into (5,3,4)+(8,6,7).

To summarize, our calculations confirm the prevision that vicinals, whose terrace length is such to accommodate on each terrace an integer

Structure	L_1/L *Structure*	L_2/L *Structure*	δ $(meV/\AA^2)$
(6,4,5)	0.53 (5,3,4)	0.47 (8,6,7)	-1.48
(7,5,6)	0.78 (5,3,4)	0.22 (8,6,7)	-0.85
(13,11,12)	0.83 (12,10,11)	0.17 (22,20,21)	-0.03
(14,12,13)	0.67 (12,10,11)	0.33 (22,20,21)	-0.14
(15,13,14)	0.57 (12,10,11)	0.43 (22,20,21)	-0.30
(16,14,15)	0.44 (12,10,11)	0.56 (22,20,21)	-0.49
(17,15,16)	0.34 (12,10,11)	0.66 (22,20,21)	-0.69
(18,16,17)	0.26 (12,10,11)	0.74 (22,20,21)	-0.51
(19,17,18)	0.18 (12,10,11)	0.82 (22,20,21)	-0.27
(20,18,19)	0.12 (12,10,11)	0.88 (22,20,21)	-0.12
(21,19,20)	0.06 (12,10,11)	0.94 (22,20,21)	-0.03
(24,22,23)	0.87 (23,21,22)	0.13 (34,32,33)	-0.02
(25,23,24)	0.75 (23,21,22)	0.25 (34,32,33)	-0.06
(26,24,25)	0.64 (23,21,22)	0.36 (34,32,33)	-0.12
(27,25,26)	0.54 (23,21,22)	0.46 (34,32,33)	-0.19
(28,26,27)	0.44 (23,21,22)	0.56 (34,32,33)	-0.27

Table 6.3:

Same as Table 6.3, but for faceting into a less-tilted vicinal plus a more-tilted vicinal. Note that, with respect to Table 6.2, energy gains have improved, and new surfaces have appeared. All cases from $M = 12$ to $M = 27$ have been considered.

number of "optimal" reconstructed cells (that is, $M \simeq 11N$ in the glue model, or $M \simeq 23N$ in real gold) are particularly stable, giving rise to an ordered array of "locked steps". Vicinals with terrace lengths which do not allow an optimal packing (that is, with $M \simeq 11(N+1/2)$ in the glue model, or $M \simeq 23(N+1/2)$ in real gold) have a strong tendency to facet into two stable orientations, one more tilted and the other less tilted with respect to the vicinal orientation.

Chapter 7

Conclusions and possible outlooks

Within the phenomenological many-body "glue Hamiltonian" scheme of Ercolessi, Parrinello and Tosatti, able to overcome most of the difficulties encountered when using a two-body potential to model a non-simple metal as gold, we have described the structural properties of several gold surfaces: in particular the low-index (111) surface and a class of vicinals of (100) and of (111). As an introduction to this work, we have provided first of all a review, based on Ercolessi et al. 's previous work, of the Hamiltonian and of its application to Au(100) and Au(110).

The main characteristic of the Au(111) surface reconstruction, well established by experiments is a slight in-plane contraction of the topmost layer along one of the densely packed directions. This gives rise to a large $(p \times \sqrt{3})$ unit cell, with $p \simeq 23$, meaning that the amount of contraction is $\simeq \frac{1}{23}$, or 4%. Our study, using the glue model, predicts a more contracted $(11 \times \sqrt{3})$ superstructure, whose structural features appear in qualitative agreement with the experimental data.

Solitons, such as hypothesized by Harten et al. [55] are not found for Au(111). The top layer contraction seems rather more uniform than in that model, but the general feature of fcc-hcp alternating stacking is confirmed.

In both cases, following the idea that reconstruction could be expected to take place on the terraces of a vicinal surface, we have considered vicinals obtained by tilting low-index surfaces around an axis orthogonal to the contraction direction. This gives rise to the $(K, 1, 1)$ family of (100)-vicinals,

and the $(M+1, M-1, M)$ family of (111)-vicinals.

Vicinals of Au(100) and Au(111) and their faceting properties turn out to be easy to describe within the glue model. This is perhaps not very surprising, since that model has shown to be rather good for the main low-index surfaces.

In the case of Au(100), "magic vicinals" induced by terrace reconstruction are found to be the (5,1,1) and (11,1,1), which agrees with preliminary experimental findings. The faceting of an arbitrary vicinal into these magic vicinals is studied and corresponds to surface energy dips. In the case of (11,1,1) this dip is directly related to the basic (1×5) Au(100) reconstruction geometry, as can be seen by checking the "6-onto-5" (actually 7-onto-6) registry between the topmost and the second layer. The (5,1,1) is a little more mysterious, and seems to correspond to the disappearance of a step structure in the vicinal.

The case of Au(111) is different because we find no magic vicinals, but rather groups of vicinals which seem preferred over others. The characteristic of each group is to contain roughly an integer number of reconstructed unit cells. Although we have not found detailed experimental studies of the Au(111) to compare with, our findings seem very much in line with Kaiser and Jaklevic's STM observation that ordered arrays of steps appear on Au(111), which seem in exact registry with the basic reconstruction periodicity.

Therefore, our main result in the thesis, for the two classes of vicinal surfaces of gold studied, is just the appearance of particularly stabilized surfaces, which compare in the faceting habit of the crystal. Their peculiarity is the fact that, with exception of (5,1,1) for Au(100)-vicinals, their terrace size contains an integer number of reconstructed unit cells. Therefore, the appearance of magic vicinals, is essentially linked to the reconstruction, which is due, in turn, to strong many-body forces of electronic origin present on noble metal surfaces. As a consequence, magic vicinals would have not been obtained if a simpler pairwise model, not including such forces, had been used.

While the magic vicinals have no impact on the macroscopic equilibrium crystal shape of the crystal, they influence strongly the "microscopic faceting" behaviour of the crystal and can be well-observed experimentally, even if they are in metastable states with respect to the corresponding low-

index orientation surfaces. In fact, the edge separating the low-index facets, when observed microscopically, should appear as a sequence of magic vicinals, each extending for one or at most a few terraces. Such picture is supported by some electron microscopy observations. A detailed study of the microscopic crystal face near facet edges is a possible future extension of our work.

By adopting the powerful minimization procedure, based on simulated annealing and molecular dynamics, the search for the "best" state is often laborious, requiring a non-trivial amount of human and computer time. However, simple relaxation procedures, if the initial state is carefully chosen, are often already useful to obtain informations on the structural and energetic trends when the tilting angle is varied, although they should be used with great caution because the danger of trapping not in the lowest minimum is high.

As a continuation of this study, other families of Au(100) and Au(111)-vicinals, i. e., tilted along different orientations, as well as Au(110)-vicinals, could be investigated. This would contribute to clarify further the interplay effects between steps and reconstruction. Au(110) vicinals, in particular, could behave in a quite different way, since Au(110) reconstructs by a faceting mechanism rather than by a top-layer in-plane contraction like Au(100) and Au(111).

Moreover, stepped surfaces could be studied at finite temperatures using molecular dynamics. Such studies are, however, rather delicate, since phase transitions, especially those involving density changes, could be undetectable in practice as a consequence of the short simulation times and small cell sizes. We have already encountered problems of this kind when studying Au(111) at finite temperature, as discussed in Chapter 3.

Finally, it should be remarked that the reliability of the results discussed in this thesis is strongly related to that of the interaction model that we have used. The glue Hamiltonian has been constructed on empirical grounds and therefore its reliability can be judged exclusively on its ability to reproduce the behaviour of the real material in several different physical situations (bulk, liquid, surfaces, finite temperature).

In this sense, the glue parametrization for Au can be regarded, overall, as well tested and rather satisfactory, although some discrepancies with experiments do exist.

On the other hand a similar study, using first principle interactions, is clearly not feasible at present, due to the relatively large unit cells, required for high index surfaces.

Therefore, an extension of this study to other materials (metals or semiconductors) is clearly possible, but subordinate to the construction of an appropriate phenomenological interaction model, as done for gold.

Bibliography

[1] P.J. Estrup in R. Vanselow and R. Hove Eds. "*Chemistry and Physics of Solid Surfaces*"V, Springer Series in Chemical Physics, Vol. 35; (Springer, Berlin, Heidelberg, 1984).

[2] Y. Tanishiro, H. Kanamori, K. Takayanagi, K. Yagi and G. Honjo, Surf. Science **111**, 395 (1981).

[3] W.J. Kaiser and R.C. Jacklevic, Surf. Science **181**, 55 (1987); Surf. Science **182**, L227 (1987).

[4] C.S. Jayanthi, E. Tosatti and A. Fasolino, Phys. Rev. B **31**, 470 (1985).

[5] Y.A. Kraftmakher and P.G. Strelkov, in *"Vacancies and Interstitial in Metals"* ed. by A. Seeger, D. Schumaker, W. Schilling and J. Diehl (North-Holland, Amsterdam, 1970), pag. 59.

[6] M. Born and K. Huang, *" Dynamical Theory of Crystal Lattices"*, (Oxford, University Press, Oxford, 1954), chapter III.

[7] J.Q. Broughton and L.V. Woodcock, J. Phys. C **11**, 2743 (1978).

[8] F. Ercolessi, *thesis, University of Trieste* (1983).

[9] R.A. Johnson, Phys. Rev. B **6**, 2094 (1972).

[10] M.I. Baskes and C.F. Melius, Phys. Rev. B **20**, 3197 (1979).

[11] F. Ercolessi, M. Parrinello and E. Tosatti, Philosophical Magazine A, **58**, 213 (1988).

[12] F. Ercolessi, E. Tosatti and M. Parrinello, Phys. Rev. Lett. **57**, 719 (1986).

[13] F. Ercolessi, M. Parrinello and E. Tosatti, Surf. Science **177**, 314 (1986).

[14] F. Ercolessi, *PhD Thesis*, International School for Advanced Studies - Trieste (1987).

[15] M. Garofalo, *Magister Thesis*, International School for Advanced Studies - Trieste (1984).

[16] M.S. Daw and M.I. Baskes, Phys. Rev. Lett. **50**, 1285 (1983).

[17] M.S. Daw and M.I. Baskes, Phys. Rev. B **29**, 6443 (1984).

[18] S.M. Foiles, M.S. Daw and M.I. Baskes, Phys. Rev. B **33**, 7983 (1986).

[19] P. Hohenberg and W. Kohn, Phys. Rev. B **136**, 864 (1964).

[20] M.W. Finnis and J.E. Sinclair, Philos. Mag. A **50**, 45 (1984); Erratum: Philos. Mag. A **53**, 161 (1981).

[21] V. Heine, Solid State Physics **35**, pag.1, (1980).

[22] D. Tománek and K.H. Bennemann, Surf. Science **163**, 503 (1985).

[23] A. Rahman, in *"Correlation functions and quasiparticle interactions in condensed matter"*, NATO Advanced Study Institute Series, Volume B53 (Plenum, New York, 1977), pag. 417.

[24] M. Parrinello and A. Rahman, Phys. Rev. Lett. **45**, 1196 (1980); J. Appl. Phys. **52**, 7182 (1982).

[25] S. Kirpatrick, C.D. Gelatt, Jr., and M.P. De Vecchi, Science **220**, 671 (1983).

[26] C.W. Gear, ANL Report 7126, Argonne National Laboratory, *Numerical Initial Value Problems in Ordinary Differential Equations*, (Pretice Hall, Englewood Cliffs, N. J. 1971).

[27] W. Andreoni, F. Ercolessi and E. Tosatti, to be published.

[28] F. Ercolessi, A. Bartolini, M. Garofalo, M. Parrinello, E. Tosatti, Surf. Science **189/190**, 636 (1987).

[29] F.Ercolessi, A. Bartolini, M. Garofalo, M. Parrinello and E. Tosatti, Physica Scripta **T19**, 399 (1987).

[30] D.G. Fedak and N.A. Gjostein, Phys. Rev. Lett. **16**, 171 (1966).

[31] A.M. Mattera, R.M. Goodmann and G.A. Somorjai, Surf. Science **7**, 26 (1967).

[32] P.W. Palmberg and T.N. Rhodin, J. Chem. Phys. **49**, 134 (1968).

[33] H. Melle and E. Menzel, Z. Naturforsh **33a**, 282 (1987).

[34] M.A. Van Hove, R.J. Koestner, P.C. Stair, J.P. Bibérian, L.L. Kesmodel, I. Bartoš and G.A. Somorjai, Surf. Science **103**, 189, (1981); Surf. Science **103**, 218 (1981).

[35] G.K. Binnig, H. Rohrer, Ch. Gerber and E. Stoll, Surf. Science **144**, 321 (1984).

[36] K.H. Rieder, T. Engel, R.H. Swendsen and M. Manninen, Surf. Science **127**, 223 (1983).

[37] K. Yamazaki, K. Takayanagi, Y. Tanishiro and K. Yagi, Surf. Science **199**, 595 (1988).

[38] T. Hasegawa, N. Ikarashi, K. Kobayashi, K. Takayanagi and K. Yagi, in *Proc. 2nd Int. Conf. on the Structure of Surfaces*, Amsterdam 1987, ed. by J.F. Van der Veen and M.A. Van Hove (Springer, Berlin, 1988), pag. 43.

[39] Brian W. Dodson, Phys. Rev. **35**, 880 (1987).

[40] A.R. Miedema, Z. Metallk. **69**, 287 (1978).

[41] Y. Okwamoto and K.H. Bennemann, Surf. Science **179**, 231 (1987).

[42] J. Villain and M.B. Gordon, Surf. Science **125**, 1 (1983).

[43] M. Garofalo, E. Tosatti and F. Ercolessi, Surf. Science **188**, 321 (1987).

[44] W. Moritz and D. Wolf, Surf. Science **88**, L29 (1979).

[45] G. Binnig and H. Rohrer, Surf. Science **126**, 236 (1983); G. Binnig, H. Rohrer, Ch. Gerber and E. Weibel, Surf. Science **131**, L379 (1983).

[46] X.Q. Wang, G.L. Chiarotti, F. Ercolessi and E. Tosatti, Phys. Rev. B, *in press.*

[47] M. Kostelitz, J.L. Damange and J. Oudar, Surf. Science **34**, 431 (1973).

[48] M.A. Chesters and G.A. Somorjai, Surf. Science **52**, 21 (1975).

[49] J. Perderau, J.P. Bibérian and G.E. Rhead, J. Phys. F **4**, 798 (1974).

[50] D.M. Zehner and J.F. Wendelken in *Proc. 7th Intern. Vacuum Congrss and 3rd Inter. Conf. on Solid Surfaces*, Vienna (1977).

[51] K. Yagi, K. Takayanagi, K. Kobayashi, N. Osakabe, Y. Tanishiro and G. Honjo in *Proc. 9th Intern. Cong. on Electron Microscopy*, Toronto (1978).

[52] K. Yagi, K. Kobayashi, N. Osakabe, Y. Tanishiro and G. Honjo, Surf. Science **86**, 174 (1979).

[53] J.C. Heyraud and J.J. Metois, Surf. Science **100**, 519 (1980).

[54] K. Takayanagi and K. Yagi, Trans. Jpn. Inst. Met. **24**, 337 (1983).

[55] U. Harten, A.M. Lahee, J.P. Toennies, C.H. Woll, Phys. Rev. Lett. **54**, 2619 (1985).

[56] L.D. Marks, V. Heine and D.J. Smith, Phys. Rev. Lett. **52**, 656 (1984).

[57] L.D. Marks and D.J. Smith, Surf. Science **143**, 495 (1984).

[58] V. Heine and L.D. Marks, Surf. Science **165**, 65 (1986).

[59] P. Bak, Reports on Progress in Physics, 589 (1982).

[60] Y.I. Frenkel and T. Kontorova, Zh. Eksp. Teor. Fiz. **8**, 1340 (1938).

[61] F.G. Frank and J.W. Van der Merwe, Proc. Royal Society (London) **198**, 205 (1949).

[62] T. Engel and K.H. Rieder in *Structural Studies of Surfaces* ed. by I. Strell and G. Schudt Weitz - Springer Tracts in Modern Physics, vol. 91, Springer - Verlag.

[63] M. El-Batanouny, S. Burdick, K.M. Martini and P. Stancioff, Phys. Rev. Lett. **58**, 2762 (1987).

[64] M. Martini, S. Burdick, M. El-Batanouny and G. Kirczenow, Phys. Rev. B **30**, 492 (1984).

[65] Y. Okwamoto and K.H. Bennemann, Surf. Science **186**, 511 (1982).

[66] J. Kanamori and K. Kawakami, Solid State Commun. **39**, 733 (1981).

[67] Y. Okwamoto and K.H. Bennemann, in preparation

[68] F. Ercolessi, A. Bartolini and E. Tosatti, Il Vuoto, **XVI**, num. 4, 230 (1987).

[69] A. Bartolini, F. Ercolessi and E. Tosatti, *Proc. 2nd Int. Conf. on the Structure of Surfaces*, Amsterdam (1987), ed. by J. F. Van der Veen and M.A. Van Hove - Springer Verlag Heidelberg.

[70] P. Carnevali, F. Ercolessi and E. Tosatti, Surf. Science **189/190**, 645 (1987); Phys. Rev. B **36**, 6701 (1987).

[71] C.Z. Wang, M. Parrinello, E. Tosatti and A. Fasolino, Europhys. Lett. **6** (1), 43 (1988).

[72] H.J. Schulz, Phys. Rev. B **22**, 5274 (1980).

[73] W. Kossel, Nachr. Ges. Wiss. Gottingen, Mathemat./Physical. Klasse 135 (1927).

[74] J.N. Stransky, Z. Phys. Chemie **136**, 259 (1928); **11**, 421 1931.

[75] B. Lang, R.W. Joyner and G.A. Somorjai, Surf. Science **30**, 440 (1972).

[76] H. Wagner in *Springer Tracts in Modern Physics*, Vol. **85**, Springer - Verlag, Berlin (1979), pag. 151, and references therein.

[77] J. Lapujolade and Y. Lejay, Surf. Science **69**, 354 (1977).

[78] G. Comsa, G. Mechtesheimer, B. Poelsema and S. Tomoda, Surf. Science **89**, 123 (1979).

[79] J. Villain, D.R. Grempel and J. Lapujoulade, J. Phys. F **15**, 809 (1985).

[80] F. Fabre, B.Salanon, and Lapujoulade in *Proc. 2nd Int. Conference on the Structure of Surfaces* (Ed. by J.F. Van der Veen and M.A. Van Hove), Amsterdam 1987, pag 520.

[81] M. den Nijs, E.K. Riedel, E.H. Conrad and T. Engel, Phys. Rev. Lett. **55**, 1698 (1985).

[82] K.S. Liang, E.B. Sirota, K.L. D'Amico, G.J. Hughes and S.K. Sinha, Phys. Rev. Lett. **59**, 2447 (1987).

[83] J.C. Boulliard, J.L. Domange and M.P. Sotto, Surf. Science **165**, 434 (1986).

[84] J.C. Boulliard and M.P. Sotto, Surf. Science **177**, 139 (1986).

[85] J.C. Boulliard and M.P. Sotto, Surf. Science **152/153**, 392 (1985).

[86] M.P. Sotto and J.C. Boulliard, Surf. Science **162**, 285 (1985).

[87] A. Brodde, St. Tosh and H. Neddermeyer, to be published.

[88] M.P. Sotto and J.C. Boulliard, *Proc. 2nd Int. Conf. on the Structure of Surfaces*, Amsterdam, Book of Abstracts, pag. 110, (1987).

[89] R.J. Phaneuf and E. Williams, Phys. Rev. Lett. **58**, 2563 (1987); Phys. Rev. B **38**, 1984 (1988).

[90] B.Z. Olshanetsky, S.M. Repinsky and A.A. Shklyaev, Surf. Science **69**, 205 (1977).

[91] D.W. Blakely and G.A. Somorjai, Surf. Science **65**, 419 (1977).

[92] R.G. Linford in *Solid State Surface Science*, Vol. 2 - Eds. M. Green (1973).

[93] J.M. Blakely and M. Eizenberg in *"The Chemical Physics of Solid Surfaces and Heterogeneous Catalysis* edited by D.A. King and D.P. Woodruff - Volume 1 : Clean Surfaces. pag.1, (1981).

[94] E.M. Lifshitz and L.P. Pitaevskii, *Statistical Physics* - Part I -, (Pergamon, Oxford) 1980, pag. 520.

[95] G. Wulff, Z. Krist. **34**, 449 (1981).

[96] A.F. Andreev, Sov. Phys. JEPT **53**, 1063 (1982).

[97] W.K. Burton, N. Cabrera and F.C. Frank, Phil. Trans. Royal Society, **243** A, 299 (1951).

[98] H. van Beijeren and I. Nolden, in *Structure and Dynamics of Surfaces II* Topics in Current Physics, ed. by W. Schommers and P. von Blanckenhagen, Springer - Verlag (1987), pag. 259.

[99] C. Rottmann and M. Wortis, Phys. Rep. **103**, 59 (1984).

[100] C. Herring, Phys. Rev. **82**, 87 (1951).

[101] P. Bennema, in *Crystal Growth*, ed. by P. Hartman, North Holland, Amsterdam (1973).

[102] P. Wymblatt, in *Interatomic Potentials and Simulation of Lattice Defects*, ed by Gehlen, Beeler and Joffee, Plenum Press (1972), pag.633.

[103] J.M. Blakely and R.L. Schwoebel, Surf. Science **26**, 321 (1971).

[104] E.E. Gruber and W.W. Mullins, J. Phys. Chem. Solids **28**, 875 (1967).

[105] M.B. Gordon and J. Villain, J. Phys. C **12**, L151, (1979).

[106] C. Jayaprakash, Craig Rottman and W.F. Saam, Phys. Rev. B **30**, 6549 (1984).

[107] A. Bartolini, F. Ercolessi and E.Tosatti, in preparation.

[108] V.M. Hallmark, S. Chiang, J.F Rabolt, J.D. Swalen and R.J. Wilson, Phys. Rev. Lett. **59**, 2879 (1987).

[109] R.C. Jacklevic and L. Elie, Phys. Rev. Lett. **60**, 120 (1988).

[110] K. Heinz, G. Schmidt, L. Hammer and K. Müller, Phys. Rev B **32**, 6214 (1985).

Acknowledgements

I would like to express my gratitude to Prof. Erio Tosatti, who has given me the ideas for this work, during very interesting and useful discussions.

I owe Doct. F. Ercolessi particular thanks. He helped me, in fact, constantly, during the years in which this work has been done, both in computing, explaining to me his programs and the way to use them, and in the understanding the theory of surfaces.

Part of computations were carried out under the SISSA-CINECA joint project, sponsored by the Italian Ministry of Education.